Karlsruhe Institute of Technology

Evaluation of Hail Occurrence over Europe and Its Relevance for Viticulture Using Multiple Data Sources

Master's Thesis by

Aleksandra Kotliarevskaia

At the KIT Department of Physics
Institute for Meteorology and Climate Research
Troposphere Research (IMKTRO)

First examiner:	apl. Prof. Dr. Michael Kunz
Second examiner:	Prof. Dr. Joaquim José Ginete Werner Pinto
First advisor:	Prof. (Adjunct) Dr.-Ing. James Daniell

June 2025 – June 2026

Karlsruhe Institute of Technology
Department of Physics
76131 Karlsruhe
Germany

Evaluation of Hail Occurrence over Europe and Its Relevance for Viticulture Using Multiple Data Sources (Master's Thesis)

I declare that I have developed and written the enclosed thesis completely by myself. I have not used any other than the aids that I have mentioned. I have marked all parts of the thesis that I have included from referenced literature, either in their original wording or paraphrasing their contents. I have followed the by-laws to implement scientific integrity at KIT.

Karlsruhe, June 2026

. . . . . .

(Aleksandra Kotliarevskaia)

Abstract

Severe convective storms (SCSs) are among the most damaging meteorological hazards in Europe, producing lightning, heavy precipitation and flash floods, tornadoes, and hail. Among these hazards, hail is one of the most damaging, significantly impacting infrastructure, populated areas, economic and insurance losses, and especially agriculture and viticulture. Vineyards are highly vulnerable because even a single severe hail event can damage shoots, leaves, and grapes, reduce the yield of the current season, and, in some cases, affect vine productivity in subsequent years. However, hail occurrence is difficult to assess consistently, as hailstorms are short-lived, spatially localized, and not fully captured by any single observational or model-based dataset. This is especially relevant for local-scale impacts, such as hail damage affecting individual wineries or wine-growing regions.

This thesis investigates the representation of hail occurrence over Europe and evaluates how effectively the datasets capture hail signals at local scales, using selected hail events that affected wineries as examples. Three datasets are analyzed: satellite-based overshooting tops (OTs), simulated maximum hail diameter at the ground level from HAILCAST coupled to a convection-permitting regional climate model, and quality-controlled hail reports from the European Severe Weather Database (ESWD). The analysis covers the period from 2011 to 2021, focusing on the warm-season months from April to September, when severe convective activity and hail occurrences are most frequent in Europe. Spatial patterns, seasonal and diurnal variability, and interannual differences are analyzed to determine if the datasets consistently depict hail occurrence across Europe. Additionally, categorical verification and selected case studies of documented hail damage to wineries are used to evaluate dataset agreement at more localized scales.

The analysis shows that the datasets provide broadly consistent information on major hail-prone regions and on the seasonal and diurnal timing of hail activity. However, their agreement becomes weaker at the daily grid-cell scale and for individual damaging events. Overall, this thesis demonstrates that combining satellite-based indicators, model-based simulations, and ground-based reports provides a more reliable assessment of hail occurrence, particularly its potential impacts on European viticulture.

Zusammenfassung

Schwere konvektive Stürme (severe convective storms, SCSs) gehören zu den schadenträchtigsten meteorologischen Gefahren in Europa. Sie können Blitzschlag, Starkniederschlag, Sturzfluten, Tornados und Hagel hervorrufen. Unter diesen Gefahren zählt Hagel zu den schadenträchtigsten Ereignissen, da er erhebliche Auswirkungen auf die Infrastruktur, besiedelte Gebiete, sowie auf wirtschaftliche und versicherungsbezogene Verluste hat und insbesondere die Landwirtschaft und den Weinbau stark beeinträchtigt. Weinberge sind besonders anfällig, da bereits ein einzelnes schweres Hagelereignis Triebe, Blätter und Trauben beschädigen kann. Dies verringert den Ertrag der laufenden Saison und beeinträchtigt in einigen Fällen auch die Produktivität der Reben in den Folgejahren. Das Auftreten von Hagel lässt sich jedoch nur schwer konsistent erfassen, da Hagelstürme kurzlebig und räumlich stark begrenzt sind. Kein einzelner beobachtungs- oder modellbasierten Datensatz kann sie vollständig erfassen. Dies ist besonders für die kleinräumigen Auswirkungen relevant, beispielsweise für Hagelschäden an einzelnen Weingütern oder in Weinbauregionen.

In dieser Arbeit wird die Darstellung des Hagelauftretens über Europa untersucht und bewertet, wie effektiv die Datensätze Hagelsignale auf lokaler Skala erfassen. Ausgewählte Hagelereignisse, von denen Weingüter betroffen waren, dienen dabei als Beispiele. Dazu werden drei Datensätze analysiert: satellitenbasierte Overshooting Tops (OTs), der am Boden simulierte maximale Hageldurchmesser aus dem Hagelwachstumsmodell HAILCAST und qualitätskontrollierte Hagelmeldungen aus der European Severe Weather Database (ESWD). Die Analyse umfasst den Zeitraum von 2011 bis 2021 und konzentriert sich auf die Monate der warmen Jahreszeit (April bis September), in denen schwere konvektive Aktivität und Hagelereignisse in Europa am häufigsten auftreten. Es werden räumliche Muster, saisonale und tageszeitliche Variabilität sowie interannuelle Unterschiede werden analysiert, um zu bestimmen, ob die Datensätze das Hagelauftreten über Europa konsistent darstellen. Zusätzlich werden eine kategorische Verifikation und ausgewählte Fallstudien dokumentierter Hagelschäden an Weingütern herangezogen, um die Übereinstimmung der Datensätze auf stärker lokalisierten Skalen zu bewerten.

Die Analyse zeigt, dass die Datensätze weitgehend konsistente Informationen über die wichtigsten hagelgefährdeten Regionen und die saisonale sowie tageszeitliche Verteilung der Hagelaktivität liefern. Ihre Übereinstimmung nimmt jedoch auf der täglichen Gitterzellenskala und bei einzelnen schadenverursachenden Ereignissen ab. Insgesamt belegt diese Arbeit, dass die Kombination satellitenbasierter Indikatoren, modellbasierter Simulationen und bodengestützter Meldungen eine zuverlässigere Bewertung des Hagelauftretens und seiner potenziellen Auswirkungen auf den europäischen Weinbau ermöglicht.

Contents

List of Figures

List of Tables

Abbreviations

BRN	bulk Richardson number
BT	brightness temperature
BWER	bounded weak-echo region
CAPE	Convective Available Potential Energy
CCN	cloud condensation nuclei
CIN	Convective Inhibition
COSMO	Consortium for Small Scale Modeling
CSI	Critical Success Index
DLS	0-6 km bulk wind shear
DMC	deep moist convection
EFZ	embryo-formation zone
ERA5	fifth-generation European Center for Medium-Range Weather Forecasts Reanalysis
ESSL	European Severe Storms Laboratory
ESWD	European Severe Weather Database
FAR	False Alarm Ratio
FFD	forward- flank downdraft
FOZ	fallout zone
HGZ	hail-growth zone
HSS	Heidke Skill Score
INP	ice-nucleating particle
IR	infrared
ISMEA	Istituto di Servizi per il Mercato Agricolo Alimentare
LCL	lifting condensation level
LFC	level of free convection
LLJ	low-level jet
LNB	level of neutral buoyancy
MCC	mesoscale convective complex
MCS	mesoscale convective systems
MCV	mesoscale convective vortex
MSG	Meteosat Second Generation
NASA	National Aeronautics and Space Administration
NUTS-3	European Nomenclature of Territorial Units for Statistics
OT	Overshooting Top
POD	Probability of Detection
RFD	rear-flank downdraft
RIJ	rear-inflow jet
SCS	Severe Convective Storm
SEVIRI	Spinning Enhanced Visible and Infrared Imager

1. Introduction

Severe Convective Storms (SCSs) are convection-driven extreme weather events that can produce hazardous meteorological phenomena such as hail, heavy precipitation, wind gusts, tornadoes, and lightning (Punge et al., 2017; van Ederen et al., 2026). In Europe, they occur predominantly during the warm season, when convective activity is favored by stronger surface heating, with the highest convective activity over continental Europe generally observed in summer (Taszarek et al., 2020a; van Ederen et al., 2026). Although these storms are often short-lived and spatially localized, they pose an important natural hazard in Europe, as they can cause substantial damage to infrastructure, agriculture, and populations every year (Taszarek et al., 2020a; van Ederen et al., 2026). In recent years, due to increasing exposure and climate change, SCSs have become one of the most significant drivers of insurance losses, as they are becoming more frequent and severe (Feldmann et al., 2025; van Ederen et al., 2026). More recently, Munich Re (2026) reported that severe thunderstorms in Europe caused a record USD 17 billion in losses in 2023, including USD 13 billion in insured losses, with hailstorms in the Alpine and Mediterranean regions being major contributors.

Hail is a primary contributor to the overall economic losses from SCSs. Estimates indicate that hailstorms account for approximately 50%-80% of all losses associated with SCSs, highlighting their importance for risk assessment and insurance applications (Allianz Commercial, 2026). In Europe, individual hailstorms have produced losses exceeding USD 1 billion. For instance, northern Italy alone experienced a record loss of USD 6 billion in 2023 (Battaglioli et al., 2026). Agriculture is particularly vulnerable to hail because even relatively small hailstones (<2 cm) can damage crops, while larger hailstones can produce severe losses to both crops and infrastructure (Ursu et al., 2025). Several individual hailstorms in Europe have caused very high economic losses. One prominent example is the 2013 storm Andreas in Germany, which produced damage exceeding EUR 3 billion (Punge and Kunz, 2016).

Vineyards are particularly vulnerable to hail, as the canopy of the grapevine, including leaves, shoots, buds, inflorescences, and bunches, can be injured even by relatively small hailstones or even by graupel. A single severe hail event can cause significant damage to the entire current-season yield and, if buds or the canopy are severely damaged, it can also affect the next year's crop. This vulnerability is economically significant because viticulture and wine production are major agricultural and commercial sectors in Europe. The European Union holds a substantial portion of the global vineyard area and wine production (International Organisation of Vine and Wine, 2025). The impact of hail on grapevines depends strongly on the phenological stage at which the event occurs. Damage that occurs early in the season, especially around budburst (March-April in the Northern Hemisphere), primarily impacts the newly developed shoots. These shoots are still fragile and can easily be broken

or removed. While regrowth may happen from secondary buds, this new growth usually has lower fruitfulness compared to the original primary shoots, leading to a reduced yield potential. If hail occurs around flowering (May - June Northern hemisphere) or fruit set, the consequences are more severe. The physical impact can break off and damage the shoot tip, part of the shoot or even entire bunches, while also stripping leaves from the canopy. As the season progresses, hail tends to affect berry development and fruit quality. Damaged berries and leaves become vulnerable to fungal diseases. Additionally, hail can have carry-over effects to the following years (The Australian Wine Research Institute, 2021).

However, quantifying the impact of hail is challenging due to its localized and short-lived nature (Ursu et al., 2025). As of now, there are several methods for detecting hail; each provides only a partial view of the situation. Currently, observations combine ground-based networks such as hailpads, which provide detailed information but only for small areas, manned stations, which provide information mostly during daytime, and insurance data, which is also very localized towards populated regions and insured property (Giordani et al., 2024). Additional insight into hail occurrence is provided by severe-weather reports from storm spotters, voluntary observers, and media sources, which are compiled into a database such as the European Severe Weather Database (ESWD) (European Severe Storms Laboratory, 2026). Another way to estimate SCS/hail frequency is by using indirect data, known as proxies, which are specifically derived from remote sensing instruments such as radar or satellites. However, radar observations across Europe are far from uniform: coverage usually stops at national borders, each country operates its own system, often with different frequencies and technologies. Moreover, topography features can create gaps in radar data. These factors make it difficult to build a consistent radar-based climatology for hail across larger regions such as Europe, particularly for extreme events (Punge et al., 2017).

Because of these difficulties, satellite-based products, such as Overshooting Tops (OTs), have been used, as they indicate strong convective updrafts that are capable of producing severe hail. However, OTs should be interpreted as a hail proxy rather than direct hail observations, since not every OT-producing storm necessarily produces hail at the ground (Punge et al., 2017). A second approach is provided by numerical model-based hail simulations, in which HAILCAST, a one-dimensional (1D) hail growth model, is coupled online to a convection-permitting regional climate simulation. While numerical weather prediction models can also simulate hail directly using advanced microphysics schemes, such approaches are computationally expensive. HAILCAST instead uses the simulated storm environment to estimate the maximum hail diameter at the ground and therefore provides a model-based estimate of hail occurrence across the model domain and simulation period (Cui et al., 2025; Thurnherr et al., 2025). In this study, both hail-indicating methods are evaluated and compared with quality-controlled hail reports from the ESWD. These reports provide reliable information on observed hail occurrence and hailstone size over broad geographic areas (Punge et al., 2017).

Based on these different data characteristics, this thesis evaluates whether satellite-based and model-based hail indicators provide a consistent representation of hail occurrence over Europe, and how their signals compare with quality-controlled ground-based hail

reports. Particular attention is paid to whether agreement between the datasets is only visible at broad spatial and temporal scales, or whether it also persists at more local scales and for selected severe hail events affecting wineries. This leads to the following research questions:

- Which European regions are most exposed to hail hazard according to OTs, HAILCAST, and ESWD?
- How consistently do OTs, HAILCAST, and ESWD represent the main spatial patterns of hail occurrence across Europe?
- How do seasonal variability, interannual distribution, and diurnal cycle of hail occurrence differ between OTs, HAILCAST, and ESWD?
- Does the spatial agreement between OTs and HAILCAST persist at the local grid-cell scale, or is the agreement mainly related to broader regional hail patterns?
- To what extent do OTs and HAILCAST capture selected severe hail events affecting wineries when evaluated at high spatial resolution?
- Can satellite-based or model-based hail indicators be used individually for hail assessment, or is a combined interpretation with ground-based reports necessary?

2. Theoretical background

This chapter provides an overview of the theoretical background relevant to this study, focusing primarily on the main processes that contribute to hail occurrence in Europe. It begins with an overview of the European climate and the large-scale atmospheric conditions that shape the spatial and temporal distribution of the convective activity.

Subsequently, the chapter outlines the thermodynamic principles underlying convection, including parcel theory and atmospheric instability, and discusses the influence of wind shear on the thunderstorm cells as well as the resulting types of convective systems. Finally, the processes of hail formation are described, together with the main factors influencing hail occurrence and its potential changes in a changing climate.

2.1. Convective activity

Europe is located in mid-latitudes, resulting in strong regional climate contrasts due to interactions between oceanic and continental air masses and its complex topography. The general atmospheric circulation over Europe is associated with mid-latitude westerlies, which contribute to the advection of maritime air from the North Atlantic and influence temperature and precipitation patterns across the continent (Barry and Chorley, 2003). As a result, a gradual transition from oceanic conditions in western Europe to more continental conditions towards the interior can be observed, while Mediterranean conditions are typical for southern Europe. This combination of influences leads to pronounced spatial variability in the European climate.

The variability of this climate is further governed by large-scale synoptic features, most notably the seasonal interplay between the Icelandic Low and the Azores High. The pressure gradient between these systems strongly influences the strength and the path of the North Atlantic storm track, while the prevailing southwesterly winds transport maritime air masses and moisture from the Atlantic towards the continent (Barry and Chorley, 2003). During the warmer season, the westerlies and associated synoptic gradients generally weaken, and Atlantic depressions over Europe are typically less intense, with weaker frontal contrasts. These large-scale conditions affect the availability of moisture, instability, and lifting mechanisms that support regional convective development.

Moisture availability represents one of the key factors controlling convective activity in Europe. The distribution of convective precipitation varies with distance from the ocean. This creates a dual pattern: cold maritime air masses tend to suppress summer convection

along northern and western coastlines, leading to a slight increase in convective activity farther inland (Taszarek et al., 2020a). In contrast, the warm waters of the Mediterranean basin significantly enhance convective development along the southern coast (Taszarek et al., 2020a; Lombardo and Bitting, 2024). Surrounding seas act as an important source of heat and moisture, especially during the warm season, when evaporation rates are high (Lombardo and Bitting, 2024). Moist air masses originating from the Mediterranean and North Atlantic can be transported into continental regions, contributing to the development of potentially unstable atmospheric conditions. In combination with surface heating and boundary-layer processes, moisture supply can precondition the atmosphere for deep convection by increasing moist-static energy, reducing Convective Inhibition (CIN), and increasing Convective Available Potential Energy (CAPE) (Kirshbaum et al., 2018). Building on this parcel-buoyancy framework, the initiation of deep moist convection (DMC) depends on whether air parcels can first be lifted to saturation and then to a level at which they become freely buoyant, allowing them to rise to great heights. In contrast to shallow convection, DMC involves sustained vertical development and the release of latent heat over a deep layer, enabling the formation of deep convective clouds – specifically cumulonimbus – and the potential occurrence of thunderstorms and hail (Markowski and Richardson, 2010; Vallis, 2017). Such conditions require sufficient lower-tropospheric moisture together with a relatively large lapse rate from the lower to middle troposphere, which allows lifted parcels to become freely buoyant and accumulate CAPE (Lin, 2007; Markowski and Richardson, 2010; Vallis, 2017).

As a result of this thermodynamic preconditioning, convective activity is a pervasive feature of the European climate, particularly over continental Europe during the summer months when radiative heating is most intense (Groenemeijer et al., 2017), whereas activity over the Mediterranean reaches its maximum during autumn. Although lightning and thunderstorms occur across the entire continent, their frequency varies significantly. Observations indicate that most of Europe experiences between 15 and 100 thunderstorm hours, with peaks exceeding 100 hours in major mountain ranges (Taszarek et al., 2020a), amounting to roughly 20 to 60 thunderstorm days annually within the more active regions of Central and Southern Europe (Groenemeijer et al., 2017). This distribution illustrates how large-scale background environments interact with regional-scale triggering mechanisms. While the broader environment establishes the necessary thermodynamic structure, mesoscale processes typically determine where the actual convective release occurs (Doswell, 1987; Lombardo and Bitting, 2024).

While thermodynamic preconditioning provides the potential for deep convection, buoyant instability and moisture alone are insufficient for initiation; air parcels generally require forced ascent to reach their level of free convection (LFC), making convective release dependent on both the background environment and specific trigger mechanisms (Doswell, 1987; Markowski and Richardson, 2010). Both synoptic-scale fronts and mesoscale features, such as drylines, sea breezes, and storm-generated outflow boundaries, often act as effective linear initiation zones. Along the airmass boundaries, intense low-level horizontal convergence mechanically forces unstable parcels upward, overcoming CIN and releasing their buoyant potential (Markowski and Richardson, 2010). However, in the absence of broad atmospheric triggering zones, localized topography provides an important source of lifting

and, therefore, plays a fundamental role in shaping regional climate and the distribution of convection. Major mountain ranges like the Alps, the Pyrenees, and the Carpathians modify atmospheric flow by acting as barriers to air masses and inducing vertical motion. Orographic lifting enhances cloud formation and precipitation, contributing to regional differences in weather patterns (Barry and Chorley, 2003).

Beyond direct mechanical lifting, mountainous terrain also supports thermally driven circulations, including slope and valley winds. By transporting warm, moist air along elevated surfaces and promoting low-level convergence, these circulations can generate localized ascent, contributing to the mesoscale triggering of convective initiation (Markowski and Richardson, 2010; Van Baelen et al., 2011; Heim et al., 2020; Fischer et al., 2025). In complex terrain, this triggering may occur not only through direct windward lifting, but also through lee-side low-level convergence, mountain-wave-induced ascent, thermally driven upslope circulations over elevated terrain, and forced lifting by ducted gravity waves (Puskeiler, 2013). The highest frequencies of organized convection are concentrated in regions such as the Po Valley, the Alpine foothills, and the western Balkan Peninsula, where topography and regional circulations can favor low-level moisture accumulation and convergence, thereby locally enhancing convective potential (Groenemeijer et al., 2017; Taszarek et al., 2020a).

When these triggering mechanisms coincide with high atmospheric instability, the presence of strong vertical wind shear can organize convection into deep, structured SCSs. In some European severe-storm environments, low-level jets (LLJs) enhance moisture transport and provide kinematic support for storm organization by strengthening vertical wind shear. This interaction between buoyancy and shear is critical for storm longevity, as it promotes the separation of updrafts and downdrafts required for organized convective modes (Púčik et al., 2015). A common indicator of such "potentially severe" environments combines CAPE and 0-6 km bulk wind shear (DLS), with values exceeding 10,000 $m^3\ s^{-3}$, considered when both variables exceed minimum thresholds (Taszarek et al., 2020a). Research using proximity soundings in Central Europe has shown that while ordinary thunderstorms occur across a wide range of environments, the probability of severe convective hazards generally increases with higher CAPE and DLS, although the relationship varies by hazard type (Púčik et al., 2015). In Central Europe, such favorable environments often develop ahead of upper-level troughs and in association with nearby cyclonic systems, where warm and moist advection contributes to destabilization and synoptic-scale ascent helps reduce inhibition. Surface lows and frontal zones may further enhance low-level convergence and forced lifting, while stronger flow in the vicinity of the jet stream can provide the vertical wind shear required for the later organization of convection (Juckes and Smith, 2000; Wissmeier and Goler, 2009; Lamb and Verlinde, 2011).

This combination of atmospheric parameters and orographic triggers facilitates the development of convective structures ranging from short-lived single cells to multicells, supercells, and larger mesoscale convective systemss (MCSs). The more organized forms are frequently associated with hazardous phenomena such as large hail, severe wind gusts, and, more rarely, tornadoes (Groenemeijer et al., 2017; Taszarek et al., 2020a). The resulting socio-economic impacts are substantial; for instance, large hail is recognized as one of the most

economically damaging natural hazards for European agriculture and property (Punge and Kunz, 2016). Furthermore, the high precipitation rates associated with SCSs often lead to localized flash flooding (Barry and Chorley, 2003). To understand the development of such high-impact events, it is necessary to examine the fundamental physical principles and thermodynamic processes that govern atmospheric convection.

2.2. Thermodynamic fundamentals

This section establishes the thermodynamic and dynamic principles that govern the initiation and development of DMC. The vertical stratification of the troposphere is the key factor in determining whether convective motion can be initiated and how it subsequently evolves. Depending on the vertical temperature gradient, the atmosphere can be stable, neutral, or unstable. To analyze the stability, parcel theory is applied, in which an idealized air parcel is displaced vertically without exchanging heat or mass with its surroundings (Markowski and Richardson, 2010; Lamb and Verlinde, 2011). Static stability then describes whether such a displacement is amplified or suppressed.

To derive the criteria for stability, an initial background fluid is considered at rest in a constant gravitational field and in hydrostatic balance (Vallis, 2017). When an idealized air parcel is displaced vertically within this environment, it departs from hydrostatic equilibrium, and its subsequent vertical acceleration is driven by the resulting buoyancy force (Markowski and Richardson, 2010). Changes in the thermodynamic state of this volume of air are described by the first law of thermodynamics. For a homogeneous, closed system, the law relates the change in internal energy du to the specific heat added to or removed from the volume of air δq, and the work done at the volume δw:

$$du = \delta q + \delta w. \tag{2.1}$$

Assuming the air follows the equation for an ideal gas,

$$p = \rho R_d T \tag{2.2}$$

where R_d is the gas constant for dry air, p is air pressure, and T is absolute temperature. With $\alpha = \rho^{-1}$ as the specific volume (with ρ as air density), Eq. (2.2) becomes

$$\rho = \frac{p}{R_d T} \Rightarrow \alpha = \frac{R_d T}{p}. \tag{2.3}$$

The change in internal energy is proportional to the change in temperature and, given the specific heat capacity with constant volume c_v, is expressed as $du = c_v dT$. With the work done by increasing the volume being $\delta w = -p d\alpha$, Eq. (2.1) can be written, using the relations given above, as:

$$\delta q = du - \delta w = c_v dT + p d\alpha \tag{2.4}$$

With enthalpy $h = u + p\alpha$ and the change in enthalpy $dh = c_p dT$, with c_p as specific heat capacity at constant pressure ($R = c_p - c_v$), substitution into Eq. (2.4) gives

$$\delta q = c_p dT - \alpha dp \tag{2.5}$$

where the terms on the right-hand side represent the change in specific enthalpy and the effects of changing pressure, respectively.

From Eq. (2.5), the dry adiabatic lapse rate can be derived, which expresses the rate of temperature change of an air parcel resulting from adiabatic expansion during ascent or compression during dry adiabatic descent. If the motion is adiabatic, $\delta q = 0$. Assuming additionally that T and p are dependent on height only, and that the atmosphere is in hydrostatic balance, meaning that the vertical pressure gradient force is balanced by the downward gravitational force,

$$\frac{dp}{dz} = -\rho g \tag{2.6}$$

where g is gravitational acceleration, Eq. (2.5) can be transformed to give the dry-adiabatic temperature gradient

$$\Gamma_d \equiv -\frac{dT}{dz} = \frac{g}{c_p} \tag{2.7}$$

where $\Gamma_d \approx 0.0098\ Km^{-1}$ (Markowski and Richardson, 2010).

2.2.1. Potential temperature

While the dry adiabatic lapse rate describes the temperature change of the displaced parcel, it is often more practical to characterize the parcel by a property that remains invariant during the vertical motion. For dry adiabatic motion, this conserved property is the potential temperature (θ). The potential temperature is defined as the temperature an air parcel would attain if it were brought dry-adiabatically from its current pressure p to a reference pressure p_0 (typically 1000 hPa).

To derive an expression for θ, we return to the first law of thermodynamics for an adiabatic process ($\delta q = 0$). From Eq. (2.5), we have:

$$c_p dT = \alpha dp. \tag{2.8}$$

Substituting the equation for an ideal gas (Eq. (2.3)) into Eq. (2.8) allows separation of T and p:

$$c_p dT = \frac{R_d T}{p} dp \implies \frac{dT}{T} = \frac{R_d}{c_p}\frac{dp}{p} \tag{2.9}$$

In logarithmic form, this expression becomes:

$$d\ln T = \frac{R_d}{c_p} d\ln p \tag{2.10}$$

By integrating Eq. (2.10) from the current state (p, T) to the reference state (p_0, θ), we obtain a Poisson's equation,

$$\theta = T\left(\frac{p_0}{p}\right)^{R_d/c_p} \tag{2.11}$$

where θ is the potential temperature conserved during dry adiabatic parcel motion. Using θ allows for a direct comparison of the thermodynamic state of air masses at different pressure levels or altitudes. This comparison is fundamental to describing the stratification of the atmosphere. By observing how the potential temperature changes with height ($\partial\theta/\partial z$), we can determine the state of the atmosphere.

In the absence of diabatic heating or cooling (such as radiation or phase changes of water), the potential temperature is conserved following a dry adiabatic parcel motion ($d\theta/dt = 0$). The vertical gradient of the potential temperature, $\partial\theta/\partial z$, therefore provides a convenient measure of dry static stability. A vertical profile with constant θ indicates a neutral stratification. If θ increases with height ($\partial\theta/\partial z > 0$), the atmosphere is considered statically stable, as a displaced parcel will find itself cooler (and thus denser) than its surroundings, leading to negative buoyancy and, thus, a sinking of the air parcel toward its original level, suppressing vertical motion. If a rising air parcel remains warmer than its environment ($\partial\theta/\partial z < 0$), it will continue to accelerate upward owing to positive buoyancy. The atmospheric conditions are considered to be unstable.

According to Markowski and Richardson (2010), deep convection cannot be understood without considering water vapor and the phase changes resulting in latent heat release. As an air parcel ascends, adiabatic cooling increases its relative humidity until saturation is reached. Beyond this point, condensation modifies the parcel's temperature change through latent heat release, so that moist thermodynamic variables such as equivalent potential temperature (θ_e) are required for describing stability in a moist atmosphere.

2.2.2. Equivalent potential temperature

The equivalent potential temperature θ_e is defined as the temperature an air parcel would attain if it were lifted dry-adiabatically to its lifting condensation level (LCL), then further lifted until all moisture has condensed, and finally brought dry-adiabatically to a reference pressure of 1000 hPa (Bolton, 1980).

For a saturated parcel undergoing condensation, diabatic heating ($r_s L_v$) is associated with a decrease in the water-vapor mixing ratio (dr) through the release of latent heat (L_v, the latent heat of vaporization). This balance is expressed through the relation between the release of latent heat and the resulting change in potential temperature. Using Eq. (2.5), we obtain:

$$-L_v dr \approx c_p T \, d\ln(\theta) \tag{2.12}$$

By integrating Eq. (2.12), we get the standard approximation for equivalent potential temperature:

$$\theta_e = \theta \exp\left(\frac{L_v r_s}{c_p T}\right) \tag{2.13}$$

(Lin, 2007). Since the condensate is treated differently in reversible and pseudoadiabatic ascent, it is useful to distinguish between equivalent potential temperature (θ_e) and pseudoequivalent potential temperature (θ_{ep}). Moist-adiabatic ascent can be treated in two limiting

ways: a reversible moist adiabatic process, in which the condensate remains within the parcel, and an irreversible pseudoadiabatic process, in which the condensate is removed immediately after formation. Accordingly, θ_e is strictly conserved under reversible conditions; many operational analyses and forecasts use the pseudoequivalent potential temperature (θ_{ep}). This value represents the temperature an air parcel attains when lifted pseudoadiabatically to 0 hPa and subsequently compressed dry-adiabatically to a reference pressure of $p_0 = 1000$ hPa.

θ_{ep} – which remains invariant during dry adiabatic ascent and nearly conserved during pseudoadiabatic ascent – is defined as:

$$\theta_{ep} = T\left(\frac{p_0}{p}\right)^{0.2854(1-0.28r_v)} \times \exp\left[r_v(1+0.81r_v)\left(\frac{3376}{T^*}-2.54\right)\right] \tag{2.14}$$

where T^* is the saturation temperature at the lifting condensation level and r_v is the water vapor mixing ratio. Although the numerical differences between θ_e and θ_{ep} are typically small, both are useful indicators of air masses and moist stability (Markowski and Richardson, 2010).

The vertical gradient of these variables is a useful indicator of moist stability and potential instability. Specifically, a layer in which θ_e decreases with height ($\frac{\partial\theta_e}{\partial z} < 0$), or equivalently θ_{ep} in many practical analysis, is potentially unstable. When such a layer is lifted, the lower part typically reaches saturation before the upper part and therefore cools less rapidly, which can further destabilize the layer (Lin, 2007; Markowski and Richardson, 2010).

2.2.3. Pseudo-adiabatic temperature gradient and stability

For an unsaturated air parcel, the thermodynamic influence of moisture is omitted during dry-adiabatic ascent, although its effect on air density is preserved by utilizing the virtual temperature T_v, defined as the temperature dry air would need to attain to have the same pressure and density as the moist air (Vallis, 2017; Markowski and Richardson, 2010). However, as an air parcel ascends and cools, it eventually reaches its LCL, where saturation is attained. Beyond this point, the onset of condensation and the subsequent release of latent heat cause the parcel to cool at the moist-adiabatic lapse rate (Γ_m), which is smaller in magnitude than the dry-adiabatic lapse rate (Γ_d). Assuming all condensate is immediately removed from the volume, the resulting pseudo-adiabatic lapse rate Γ_{ps} (or Γ_s) is expressed as:

$$\Gamma_s \equiv -\left.\frac{dT}{dz}\right|_{ad} = \frac{g}{c_p}\frac{1+Lq_s/(R^dT)}{1+L^2q_s/(c_pR^vT^2)}, \tag{2.15}$$

where q_s denotes the specific humidity at saturation, which is approximately equal to the saturation mixing ratio (under typical atmospheric conditions) (Vallis, 2017).

This behavior is linked to the strong temperature dependence of the saturation vapor pressure (E). According to the Clausius-Clapeyron equation, the rate of change of E with absolute temperature T is expressed as

$$\frac{dE}{dT} = \frac{L_v E}{R_v T^2}, \tag{2.16}$$

where R_v is the specific gas constant of vapor. The differential relationship implies that E increases approximately exponentially with temperature. As a result, the saturation specific humidity $q_s \approx \epsilon E/p$, where $\epsilon = R_d/R_v \approx 0.622$ represents the ratio of the gas constants of dry air and water vapor. Consequently, leading to a strong non-linear dependence of q_s on temperature. As q_s increases with temperature, the magnitude of the saturated adiabatic lapse rate Γ_s decreases; accordingly, Γ_s is smaller in warm, humid lower-tropospheric air and approaches the dry-adiabatic value Γ_d at high altitudes. This explains why, in the warm and moisture-rich environment of the lower atmosphere, the condensation-driven release of latent heat is so significant that Γ_s can be as low as 0.003 K m^{-1}, while typical values are around 0.006-0.007 K m^{-1} in the midtroposphere (Vallis, 2017; Holton and Hakim, 2013).

The pseudo-adiabatic lapse rate is a fundamental variable for determining atmospheric stability using parcel theory. By comparing environmental lapse rate ($-\partial\tilde{T}/\partial z$, where $\tilde{T}$ is the environmental temperature) to the saturated adiabatic lapse rate, different stability regimes can be identified:

- If $-\partial\tilde{T}/\partial z < \Gamma_s$, then a saturated parcel will be cooler and denser than its surroundings, causing it to sink. This is a stable regime.
- If $-\partial\tilde{T}/\partial z > \Gamma_s$, then parcel is warmer and less dense than its surroundings and therefore tends to continue rising.

These criteria determine whether a saturated parcel becomes positively or negatively buoyant relative to its environment. The resulting vertical acceleration is then governed by the buoyancy force (Holton and Hakim, 2013; Vallis, 2017).

2.2.4. Buoyancy

The vertical ascent of an air parcel in the troposphere can be triggered by various mechanisms, such as orographic lifting and large-scale synoptic forcing. However, the continued displacement of a parcel depends on wether it becomes positively buoyant relative to its environment. An air parcel displaced vertically accelerates when its local hydrostatic equilibrium is disrupted (Markowski and Richardson, 2010). This acceleration is determined by the combined effects of the vertical perturbation pressure-gradient force and buoyancy relative to a hydrostatic base state, with buoyancy arising from density differences between the parcel and its environment.

To define the buoyancy force B, it is necessary to examine the vertical component of the equation of motion ($\frac{dw}{dt} = -\frac{1}{\rho}\frac{\partial p}{\partial z} - g + F_w$). In a Cartesian coordinate system, neglecting

frictional forces F_w and the effects of Earth's rotation on small-scale vertical motion, the momentum equation is expressed as (Holton and Hakim, 2013)

$$\rho \frac{dw}{dt} = -\frac{\partial p}{\partial z} - \rho g \tag{2.17}$$

where w is the vertical velocity and $g = 9.81$ m s^{-2}. To isolate the perturbation leading to convective motion, we define a horizontally homogeneous base state (denoted by an overbar) that is in hydrostatic balance, such that

$$0 = -\frac{\partial \bar{p}}{\partial z} - \bar{\rho} g. \tag{2.18}$$

Subtracting this equation from Eq. (2.17) yields

$$\rho \frac{dw}{dt} = -\frac{\partial p'}{\partial z} - \rho' g, \tag{2.19}$$

where p' and ρ' denote perturbations from the hydrostatic base state. Rearranging these terms results in the following expression for vertical acceleration:

$$\frac{dw}{dt} = -\frac{1}{\rho}\frac{\partial p'}{\partial z} - \frac{\rho'}{\rho} g = -\frac{1}{\rho}\frac{\partial p'}{\partial z} + B \tag{2.20}$$

The term $-\frac{1}{\rho}\frac{\partial p'}{\partial z}$ represents the vertical perturbation pressure gradient force, while the last term of the equation represents the buoyancy. Specifically, buoyancy is the vertical acceleration associated with the parcel's density difference relative to its environment. Using the Boussinesq approximation, which assumes that $\rho' \ll \bar{\rho}$, it is often sufficiently accurate to replace ρ with a mean reference density $\bar{\rho}$ in the denominator of the buoyancy term. If the effects of pressure perturbations and moisture are neglected, B can also be rewritten as:

$$B \approx g\left(\frac{T_{vp} - T_{venv}}{T_{venv}}\right). \tag{2.21}$$

T_{vp} and T_{venv} are virtual temperatures of an air parcel and environment, respectively. If $T_{vp} > T_{venv}$, the parcel experiences positive buoyancy and therefore upward acceleration. However, this framework assumes that the parcel is dry. In reality, the vertical acceleration of a parcel is also influenced by localized vertical pressure disturbances and the weight of falling precipitation (hydrometeor loading).

Accounting for these factors, the definition of buoyancy is expanded to include a correction for the local perturbation pressure ($\frac{p'}{\bar{p}}$) alongside the downward drag of hydrometeor loading ($-gr_h$), where r_h is the mixing ratio of total hydrometeors:

$$B \approx \left(\frac{T_v'}{\overline{T_v}} - \frac{p'}{\bar{p}} - r_h\right) g = \left[\frac{\theta_\rho'}{\overline{\theta_\rho}} + \left(\frac{R_d}{c_p} - 1\right)\frac{p'}{\bar{p}}\right] g. \tag{2.22}$$

Here, the total mass of condensed water (liquid or ice) directly reduces the net buoyancy of the parcel. Buoyancy, therefore, provides the immediate dynamical mechanism through which thermodynamic instability is translated into vertical parcel acceleration (Markowski and Richardson, 2010).

2.2.5. CAPE and CIN

CAPE serves as a measure of the maximum velocity a buoyant air parcel can theoretically acquire during its ascent. As such, it is widely used to characterize the potential intensity of DMC. However, this maximum is a theoretical limit based on the assumption that the parcel remains isolated from its environment – neglecting the energy-depleting effects of entrainment and the downward physical weight of condensed water (Holton and Hakim, 2013; Lamb and Verlinde, 2011).

The magnitude of CAPE depends fundamentally on the vertical temperature profile and boundary layer humidity (Figure 2.1). While a full vertical profile is required for temperature, the moisture component is limited to the lower atmosphere, using either a 2-meter value for surface-based CAPE or layer-averaged data for mixed-layer and most unstable cases. Because the density of an air parcel is sensitive to its water vapor content, CAPE is calculated using the virtual temperature (T_v) (Emanuel, 1995). This sensitivity is critical because the molecular weight of water (18.01 g mol^{-1}) is lower than the mean molecular weight of dry air (28.97 g mol^{-1}); consequently, the presence of moisture enhances buoyancy even before latent heat is released during condensation (Lamb and Verlinde, 2011).

Higher surface temperatures and increased low-level moisture content generally increase the parcel's equivalent potential temperature (θ_e), which tends to enlarge the area between the parcel's moist adiabat and the environmental sounding. Calculation-wise, CAPE is determined by the vertical integral of buoyancy force per unit mass from the LFC to the level of neutral buoyancy (LNB) (Holton and Hakim, 2013):

$$\text{CAPE} = \int_{z_{LFC}}^{z_{LNB}} g \left(\frac{T_{vp} - T_{venv}}{T_{venv}} \right) dz. \tag{2.23}$$

In a practical meteorological context using pressure as the vertical coordinate (p-system), this expression is rewritten by (Wallace and Hobbs, 2006):

$$\text{CAPE} = \int_{p_{LNB}}^{p_{LFC}} R_d (T_{vp} - T_{venv}) \, d \ln p. \tag{2.24}$$

Within this parcel-buoyancy framework, the integration boundaries represent critical thermodynamic thresholds. Once an air parcel is mechanically forced past its LFC, it becomes warmer than its surroundings and accelerates upward freely due to positive buoyancy. This free ascent continues until the parcel reaches the LNB — also referred to as the equilibrium level — where its temperature converges again with that of the ambient environment. The positive buoyancy accumulated between these two levels defines the total magnitude of CAPE (Lin, 2007; Markowski and Richardson, 2010; Vallis, 2017). CAPE is widely used as an indicator of the potential for DMC in forecasting.

Below the LFC, a lifted parcel is often cooler than its environment, creating a region of negative buoyancy known as CIN. CIN is the energy barrier that must be overcome to lift the parcel from the ground to the LFC; it represents the work that must be done by external

lifting. CIN is calculated by integrating the negative buoyancy from the parcel's initial level — which may be the surface or a representative mixed layer — to the LFC:

$$\text{CIN} = -\int_{z_{surf}}^{z_{LFC}} g\left(\frac{T_{vp} - T_{venv}}{T_{venv}}\right) dz \tag{2.25}$$

Therefore, a parcel cannot access the energy represented by CAPE unless it has a sufficient external mechanical or thermal energy to overcome the CIN barrier (Figure 2.1). Once the LFC is reached, the parcel undergoes free upward acceleration, and the potential energy defined by CAPE is converted into vertical kinetic energy (Holton and Hakim, 2013). This energy is visually represented as the area on a thermodynamic diagram bounded by the parcel's process curve and the environmental temperature profile. The relationship between CAPE and theoretical maximum thermodynamic updraft velocity (w_{max}) is established via the conservation of energy equation:

$$w_{max} = \sqrt{2 \cdot \text{CAPE}} \tag{2.26}$$

So this relationship illustrates that larger CAPE values favor stronger updrafts. Additionally, in idealized upright convection, such as a growing cumulus cloud, the vertical acceleration is partially reduced by a perturbation-pressure gradient force that opposes the upward buoyancy, while the required compensating subsidence in the surrounding environment warms the air and further diminishes the parcel's buoyancy. Furthermore, the magnitude of CAPE dictates the "residence time" of hydrometeors within the cloud; high CAPE environments produce rapid ascents that can carry supercooled liquid water high into the mixed-phase region before it has time to freeze, which is a prerequisite for significant lightning and hail development (Lamb and Verlinde, 2011; Emanuel, 1995).

While CAPE describes the buoyant energy available to a parcel, whether that energy is realized depends strongly on CIN, which is often associated with a capping inversion atop of the boundary layer. (Holton and Hakim, 2013). Such a cap can suppress weak, disorganized convection, thereby allowing heat and moisture to accumulate within the boundary layer and increasing CAPE; if the inhibition is too strong, however, convection may be entirely suppressed regardless of instability. The presence of moderate CIN often serves to regulate the release of potential energy, thereby allowing the accumulation of high CAPE. Consequently, when inhibition is finally overcome by sufficiently strong lifting, the resulting convective initiation is typically more explosive than in uninhibited environments (Emanuel, 1995).

2.3. Thunderstorm types

The morphological organization of DMC is fundamentally directed by the interplay between thermodynamic instability and the kinematic structure of the environment. Among the governing environmental parameters, vertical wind shear is the most significant in determining the storm type. While vertical wind shear generally helps a storm to stay organized

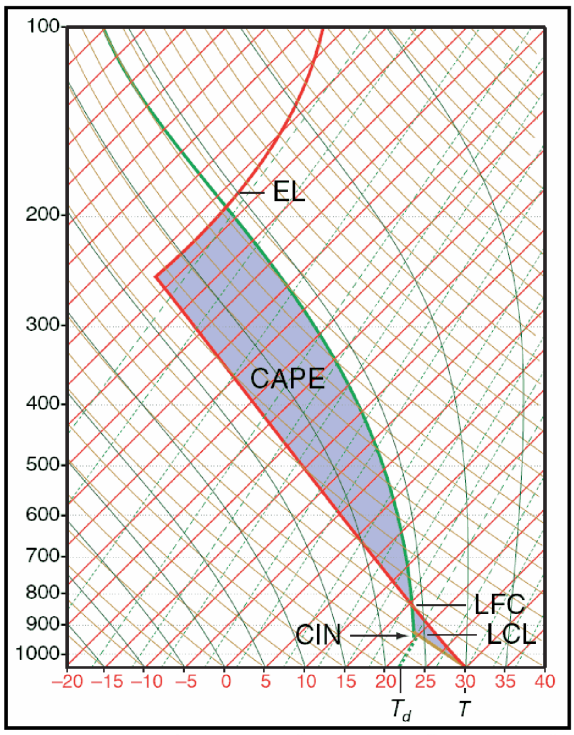

Figure 2.1.: Schematic Skew-T log-p diagram illustrating CIN, CAPE, LCL, LFC, and equilibrium level (EL). Adapted from the National Oceanic and Atmospheric Administration (NOAA)/National Weather Service Skew-T training page (NOAA National Weather Service, nd).

and last longer, in environments with weak instability, very strong shear can hinder the development of an initial updraft, partly by enhancing entrainment of environmental air and thereby reducing parcel buoyancy (Markowski and Richardson, 2010).

While the magnitude of CAPE provides information about the thermodynamic potential for deep convection, the eventual storm mode depends to a large extent on the magnitude and structure of the environmental shear (Holton and Hakim, 2013). To quantify the relation, the bulk Richardson number (BRN), a non-dimensional parameter, is commonly used to relate the available buoyancy to the vertical wind shear. The BRN is expressed as (Wallace and Hobbs, 2006):

$$\mathrm{BRN} = \frac{\mathrm{CAPE}}{\frac{1}{2}U^2} \tag{2.27}$$

In this equation, U represents the difference between the mean wind in the 0-6 km layer and the mean wind in the lowest 500 m of the atmosphere. CAPE primarily describes the buoyant energy available to ascending parcels, but higher values may also favor stronger cold-pool development and stronger convective outflow through enhanced hydrometeor loading, and melting and evaporative cooling (Markowski and Richardson, 2010). Convective phenomena are generally categorized into three classes: single-cellular, multicellular, and supercellular thunderstorms, each defined by unique dynamic balances, spatial extents, and hazard potentials (Lamb and Verlinde, 2011).

2.3.1. Single-cell Convection

The single-cell thunderstorm represents the most elementary form of deep moist convective organization, typically manifesting in environments characterized by weak vertical wind shear, where the bulk wind difference over the deep convective layer (typically 0–6 km) is usually on the order of less than ≈ 10 m s^{-1}. This minimal wind differential prevents new cells from being initiated, at least in an organized way. According to the classical model, the cell undergoes a three-stage evolution (Byers and Braham, 1949; Doswell, 1987). The first stage is the towering cumulus stage, which is characterized by a strong updraft that leads to the formation of a towering cumulus cloud. In the mature stage, hydrometeors grow large enough to fall through the updraft. Their descent increases hydrometeor loading within the cloud, while evaporation below cloud base enhances negative buoyancy and supports downdraft formation. Once the downdraft reaches the surface, a gust front develops from the cold pool, but in weak-shear environments this outflow tends to undercut the updraft rather than support sustained regeneration (Figure 2.2). As a consequence, the storm enters the dissipating stage, when the supply of warm, moist boundary-layer air into the updraft is cut off (Doswell, 1987; Markowski and Richardson, 2010; Lamb and Verlinde, 2011).

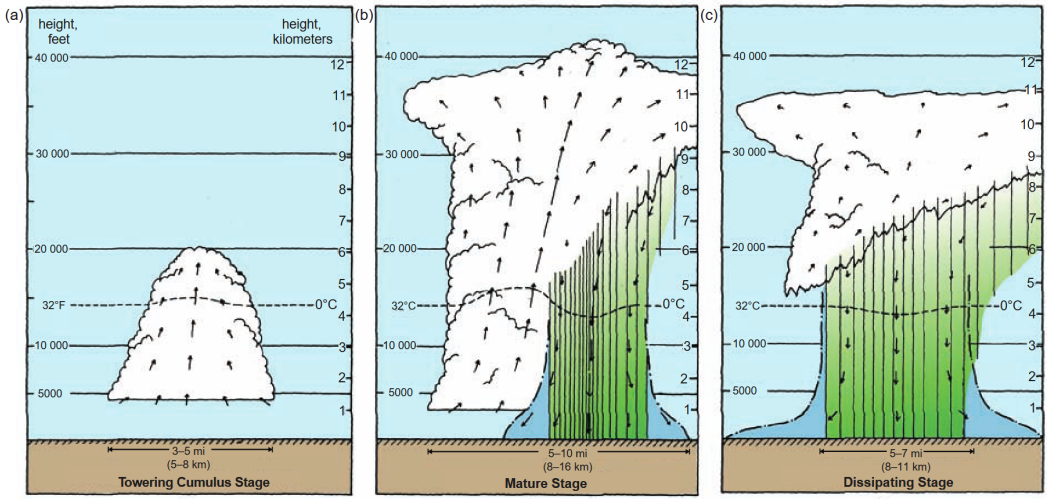

Figure 2.2.: Lifecycle of a single cell convection. Arrows denote updrafts and downdrafts, green shading represents precipitation, and blue shading indicates rain-cooled air (Markowski and Richardson, 2010).

This evolution is fundamentally driven by adiabatic expansion of the rising air parcel during ascent, which reduces its temperature to the point of saturation, thereby promoting condensation and supporting the later formation of solid precipitation particles. As with all moist convective cells, this vertical growth is powered by the release of latent heat during condensation. However, in single cells, buoyancy is significantly mitigated by entrainment, where mixing of drier environmental air dilutes the updraft and causes partial droplet evaporation (Lamb and Verlinde, 2011).

Because there is weak vertical shear to tilt the storm's axis, the precipitation core, which may include rimed ice particles such as graupel or small hail, remains close to the updraft region.

Consequently, the storm cannot maintain a persistent spatial separation between ascending and descending air. This process, driven by precipitation loading together with evaporative cooling, effectively "chokes" the updraft, leading to a relatively short lifecycle that rarely exceeds 30 to 60 minutes. Single-cellular convection often occurs under comparatively weak synoptic forcing, frequently near the time of maximum daytime heating. While their severe-weather potential is limited, single cells may still produce strong wind gusts, heavy precipitation, and, in some cases, small hail (Markowski and Richardson, 2010; Holton and Hakim, 2013).

2.3.2. Multi-cell Convection

Multicellular convection is probably the most common form of DMC in mid-latitudes. Convection organizes into multi-cell systems when the environment exhibits moderate wind shear (usually 10–20 m s^{-1} in the 0–6 km layer). Multicellular convection consists of a succession of single cells, with new updrafts repeatedly forming along the boundary of the storm-generated cold pool (Markowski and Richardson, 2010). As the cold, dense outflow from mature cells spreads along the surface, the associated gust front forces the ascent of warm, high-θ_e environmental air to its LFC (Lamb and Verlinde, 2011). The forced ascent triggers the development of new cells on the downshear flank, which eventually mature and replace the older dissipating cells (Figure 2.3).

This repeated cell regeneration along the outflow boundary gives rise to storm propagation, meaning that the system's motion is a combination of cell advection and continued initiation of new cells. Because of this efficient structural regeneration, more severe multicellular systems may persist for several hours and produce broad swaths of damaging straight-line winds and large hail (Markowski and Richardson, 2010). At the same time, the movement of the system may differ substantially from the mean environmental wind in the cloud-bearing layer, as its track is heavily steered by where these new updrafts are continuously triggered (Markowski and Richardson, 2010; Lamb and Verlinde, 2011).

2.3.3. Supercell convection

Supercells are highly organized, long-lived storms characterized by a persistent, rotating updraft, and an associated mesocyclone (Markowski and Richardson, 2010; Holton and Hakim, 2013). Unlike multicells, which consist of successive cells, a supercell is dominated by a single primary deep updraft that remains active for a prolonged period (1-4 hours is common; sometimes it can last 8 hours). Supercells are less common than single-cell or multicell storms, but they account for a disproportionately large share of severe convective weather, including large hail, destructive wind gusts, and tornadoes (Lamb and Verlinde, 2011; Lin, 2007).

Supercells typically form in environments with strong deep-layer vertical wind shear, often exceeding $\approx 15 - 20\ ms^{-1}$. Directional shear favors the development and persistence of cyclonically rotating right-moving storms, which commonly become dominant in midlatitude

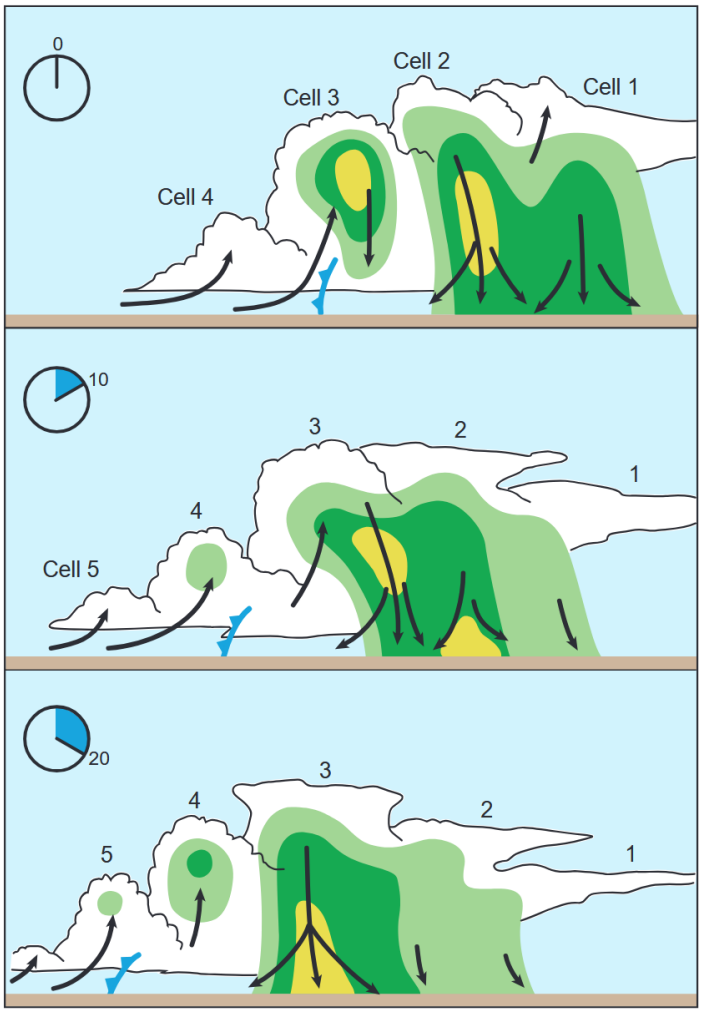

Figure 2.3.: Schematic of the typical life cycle and organization of a multicellular convective storm, with individual cells shown at different developmental stages (Markowski and Richardson, 2010).

environments. At the same time, the interaction between the updraft and the sheared ambient flow generates dynamic pressure perturbations whose vertical gradients can enhance upward acceleration and influence storm propagation (Markowski and Richardson, 2010; Lamb and Verlinde, 2011; Holton and Hakim, 2013).

Strong shear contributes to a pronounced separation between the updraft and the downdraft. This separation ensures that hydrometeors produced in the updraft are advected away from their source region, preventing the updraft from being rapidly choked by its own precipitation. Supercells commonly contain two principal downdraft regions: a forward-flank downdraft (FFD), which is associated with the main precipitation region, and the rear-flank downdraft (RFD), which occurs to the rear of the updraft. The RFD region may also contain precipitation, particularly within the hail core or along the pendant-shaped hook echo observed in low-elevation radar imagery. Rather than a simple byproduct of horizontal wind wrapping, this hook structurally represents the downward extension of the

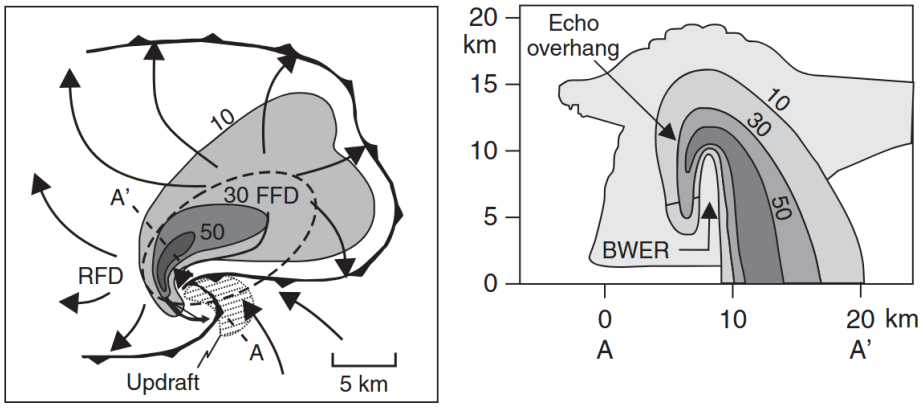

Figure 2.4.: Schematic structure of a supercell storm shown in plan view (left) and in a vertical cross-section along A–A′(right). Radar reflectivity is indicated by shading, the updraft by hatching, and the arrow denotes the direction of storm movement. RFD and FFD indicate the rear-flank and forward-flank downdrafts, respectively, and BWER marks the bounded weak-echo region. Adapted from Lemon and Doswell (1979) and Markowski and Richardson (2010).

precipitation overhang that caps the storm's bounded weak-echo region (BWER) (Figure 2.4) (Lamb and Verlinde, 2011).

Finally, their propagation may deviate from the mean environmental wind, and right- and left-moving storm splits are possible in strongly sheared environments. However, when the environmental shear turns clockwise with height, the right-moving storm is dynamically favored and is therefore often the dominant cell in midlatitude environments (Holton and Hakim, 2013).

2.3.4. Mesoscale convective systems

A MCS is defined as a complex of thunderstorms that becomes organized on a scale larger than the individual cells and persists for several hours or more. Unlike isolated cells, many MCSs develop a mesoscale circulation that is coupled with the convective scale updrafts and downdrafts. The longevity of many MSCs is sustained by the continuous initiation of new convective cells at the edge of the cold pool, replacing the decaying older ones. The system's evolution is driven by the interaction between diabatic processes, such as latent heat release and evaporative cooling, and the environmental wind shear. These systems often produce a significant amount of precipitation in midlatitude regions and are characterized by a contiguous precipitation area with a horizontal scale of at least 100 km in at least one direction (Markowski and Richardson, 2010).

One of the subclasses of an MCS is a squall line - a quasi-linear arrangement of convective cells in a narrow line that moves rapidly and produces heavy precipitation. The squall lines are favored in environments with stronger vertical shear. Their length can extend to hundreds of kilometers, while their width is comparatively narrow. Structural evolution may lead to the development of a bow-echo-shaped structure, driven by a rear-inflow jet

(RIJ) that can produce damaging surface winds. This jet forms as evaporation and melting of hydrometeors falling from the trailing anvil induce mid-level diabatic cooling, generating a localized low-pressure perturbation that forces mid-tropospheric environmental air to accelerate forward from the rear of the system (Lamb and Verlinde, 2011).

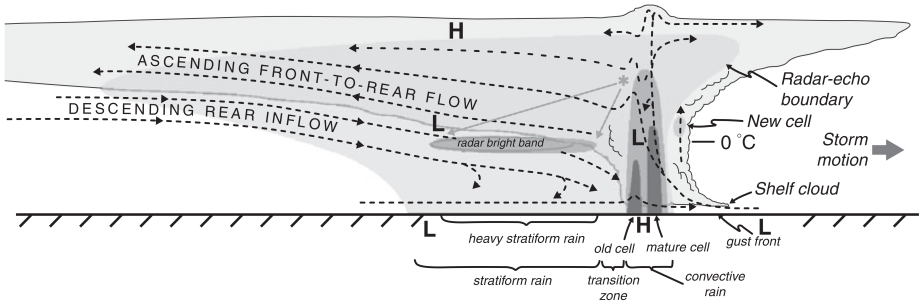

Figure 2.5.: Vertical cross-section displaying the structural organization of a squall line featuring a trailing stratiform precipitation zone. The perspective is aligned normal to the leading convective boundary. Adapted from Houze et al. (1989), after Lamb and Verlinde (2011)

.

Another subclass of MCS is the mesoscale convective complex (MCC), characterized by large, cold, near-circular anvils that are easily captured by satellite imagery. MCCs are usually initiated near sunset and persist through the night. Their maintenance is favored by continued warm, moist inflow, often enhanced by the nocturnal low-level jet. Because of their size and duration, they also develop a warm-core circulation (Markowski and Richardson, 2010; Lamb and Verlinde, 2011).

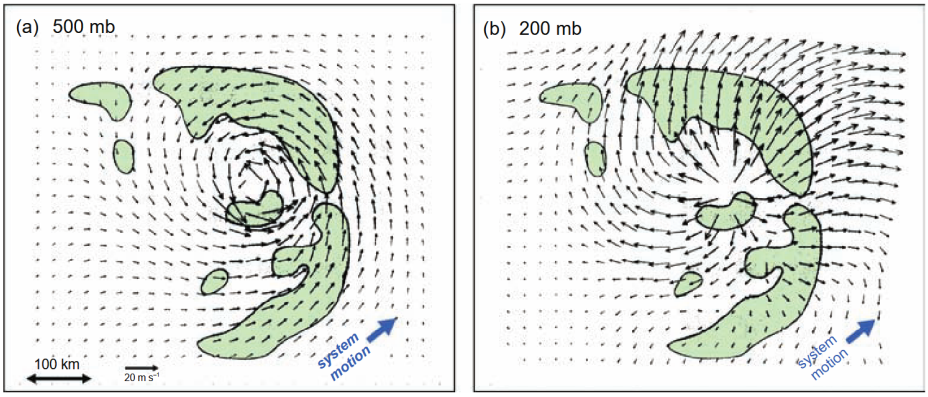

Figure 2.6.: Simulated vorticity pattern associated with a midlatitude mesoscale convective complex, displayed at 500 hPa (a) and 200 hPa (b). Arrows represent system-relative winds, while green shading marks regions of convective precipitation. Adapted from Chen and Frank (1993) and Markowski and Richardson (2010).

As some MCSs grow upscale, they can develop warm-core meso-α-scale (200–2000 km) circulations. Near the tropopause, this circulation is associated with a mesohigh and divergent anticyclonic outflow once Coriolis effects start to influence the flow, whereas below the level of maximum convective heating, a convergent cyclonic eddy may develop,

referred to as a mesoscale convective vortex (MCV) (Figure 2.6). Such vortices can persist beyond the decay of the parent convection and may contribute to renewed convection on subsequent days (Markowski and Richardson, 2010).

2.4. Hail formation and damage

This section describes the microphysical processes that lead to the formation and growth of hail in deep convective clouds. Because hail is a solid precipitation particle that develops in strongly convective clouds rich in supercooled liquid water, its formation cannot be understood without first considering the initiation of cloud and ice particles and the subsequent growth of ice by collection. The final size of hailstones depends on both microphysical growth by accretion and on the storm conditions that allow embryos and growing stones to remain or repeatedly re-enter the favorable environment (Markowski and Richardson, 2010; Lamb and Verlinde, 2011).

2.4.1. Nucleation

The first step in the formation of cloud droplets and ice crystals is nucleation, the process by which a phase change occurs and a new condensed phase (either liquid or ice) forms from water vapor. According to classical nucleation theory, a new phase initially forms as a microscopic embryo within a metastable parent phase. However, the formation of such an embryo creates a new interface between the developing condensed phase and the surrounding parent phase. Very small embryos are unstable because they require a lot of energy to create a new interface, so they tend to evaporate or dissipate before sustained growth can occur. Therefore, establishing a stable phase requires that an energetic barrier be overcome. For liquid droplets, this transition depends on cloud condensation nuclei (CCN) optimizing growth through solubility or size of the dry aerosol particle. In contrast, stable ice crystal formation requires an ice-nucleating particle (INP) to act as an insoluble, crystallographically compatible substrate (Lamb and Verlinde, 2011).

There are two types of nucleation in cloud formation: homogeneous and heterogeneous. Homogeneous nucleation occurs without the involvement of a foreign particle or surface, and requires very high supersaturation or, in the case of ice formation, temperatures below $\approx -38°C$ (Pruppacher et al., 1998).

Heterogeneous nucleation occurs when aerosol particles serve as CCN or INP. By providing a foreign surface, these particles reduce the energy barrier, allowing phase transitions under much lower supersaturation conditions than in homogeneous processes (Lamb and Verlinde, 2011). Depending on whether a liquid droplet or an ice crystal is forming, the nucleating particles must meet different physical requirements:

- CCN: to initiate liquid cloud droplets, a CCN must facilitate condensation by effectively lowering the critical supersaturation threshold. The most effective CCN are composed of soluble substances (e.g., sulfates, sea salt, and secondary organic aerosols), which

lower the vapor pressure over the droplet surface. CCN are relatively abundant in the atmosphere, with characteristic number densities often reaching 100 to 1000 cm^{-3} (Lamb and Verlinde, 2011).

- INP: to initiate solid ice crystals in the mixed-phase zone (0°C to −38°C), an INP must provide a foreign, insoluble substrate that lowers the activation energy barrier for ice formation. Efficient INP often possess crystalline structures related to the hexagonal lattice of ice, such as certain mineral dusts (clays) and specific biological agents (e.g., bacterial proteins). These particles are significantly scarcer than CCN, often present at concentrations of fewer than 1 $liter^{-1}$ in mixed-phase clouds (Lamb and Verlinde, 2011).

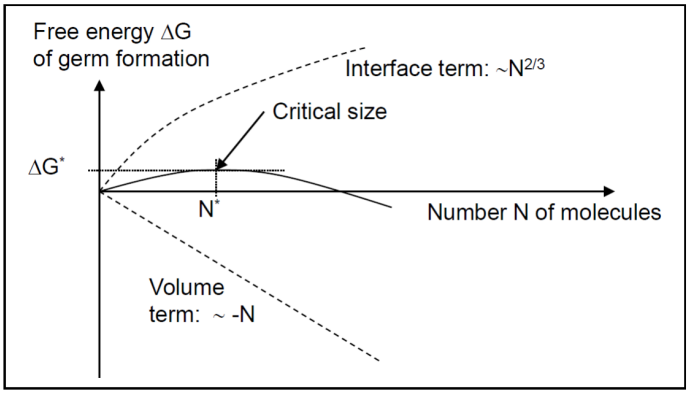

Figure 2.7.: Classical nucleation theory. Illustration of the Gibbs free energy (ΔG) as a function of embryo size (N), adapted from the theoretical framework of Köhler (1921) and the visualization by Möhler (2024). The curve shows the critical embryo size threshold (N^*). The surface energy component (interface term) acts as a barrier to formation, while the bulk chemical potential change (volume term) provides the driving force for phase transition once the critical radius is surpassed.

The thermodynamic framework for the phase change of droplets can be described by classical nucleation theory (Köhler, 1921), which quantifies the total change in Gibbs free energy (ΔG) required to form a stable nucleus from a metastable parent phase. This energy balance is expressed by Equation 2.28, which consists of two terms that determine whether an embryo will stabilize or dissipate (Lamb and Verlinde, 2011).

$$\Delta G = -NkT \ln S + \sigma A \tag{2.28}$$

The first term, $-NkT \ln S$, is the bulk volume term and represents the energetic advantage gained when molecules move into a more stable condensed phase under supersaturated conditions (Markowski and Richardson, 2010). Because the term is negative when the saturation ratio is higher than 1 ($S > 1$), it serves as a fundamental driving force for nucleus growth. In contrast, the interface term (σA) accounts for the work necessary to establish a boundary between the new embryo and the surrounding vapor (Lamb and Verlinde, 2011). This surface tension creates a positive barrier that small clusters must overcome (Markowski and Richardson, 2010).

As shown in Figure 2.7, the interface term dominates at the smallest scales, creating an energy barrier to the phase transition; however, because volume scales more rapidly than surface area, the negative volume term eventually becomes the controlling factor as the embryo grows. Once the embryo exceeds the critical size N^*, the net free energy decreases with continued growth, meaning the aggregate has become a stable nucleus that will spontaneously expand into a cloud droplet (Lamb and Verlinde, 2011).

For ice formation, several heterogeneous nucleation modes exist: deposition nucleation, contact nucleation, condensation-freezing, and immersion-freezing. These mechanisms are vital in mixed-phase clouds where ice coexists with supercooled water – a metastable state where water droplets remain unfrozen at temperatures as low as −40°C due to a lack of sufficient ice-nucleating particles. In deep convective clouds, these supercooled droplets act as the primary growth medium for hail. For the later development of hail, only a small initial number of ice particles may be adequate. Therefore, while nucleation provides a starting point, the growth of large hail mainly depends on the subsequent growth mechanisms and storm dynamics (Markowski and Richardson, 2010).

2.4.2. Growth and formation of ice particles

Once particles have formed, they grow via vapor diffusion and the collection of liquid droplets (Figure 2.8). Growth by vapor diffusion is only effective for very small particles, but as they grow, this process slows, and hail size increasingly relies on collection processes. In the context of hail, the most critical mechanism is riming (or accretion). This occurs when an ice particle collects supercooled cloud droplets that freeze upon impact (Lamb and Verlinde, 2011).

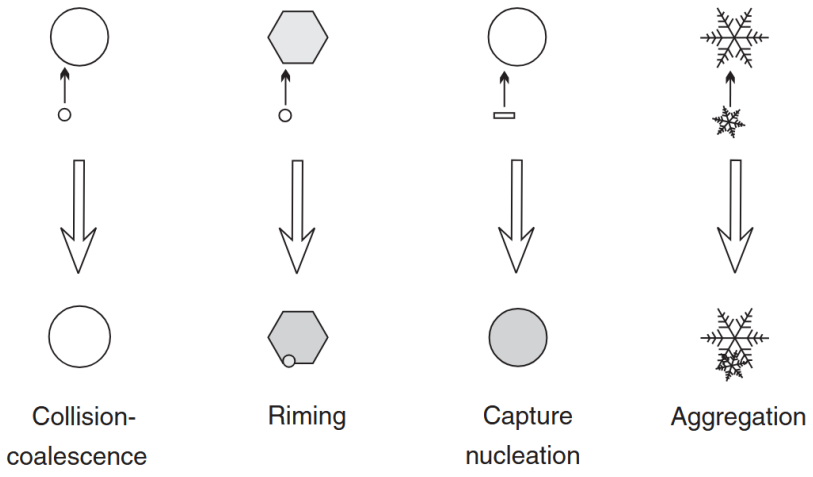

Figure 2.8.: Particle growth involving collection (Lamb and Verlinde, 2011).

Hail growth by riming begins with a hail embryo, which can either be a graupel particle or a large frozen drop. A graupel forms when an ice crystal grows by collecting small cloud droplets that freeze instantly on contact, whereas a frozen drop forms when a relatively large

liquid drop is carried by a strong updraft above the freezing level, where it eventually freezes. The embryo type depends strongly on the cloud-base temperature. Cool-base clouds favor graupel, while warmer-base clouds, which allow for more efficient collision-coalescence (large drop formation) below the freezing level, favor frozen-drop embryos (Lamb and Verlinde, 2011).

After approximately 5–10 minutes of growth, ice particles gain enough mass for their fall speed to increase compared to the surrounding droplets. As particle size and fall speed increase, they can collide with more supercooled droplets due to their larger cross-sectional area. This accelerates the growth rate as long as the particle remains in a region with sufficient supercooled liquid water (Markowski and Richardson, 2010).

There are two defined hailstone growth regimes. The first is the dry growth regime. It occurs when the accretion rate is moderate, allowing the hailstone surface temperature to remain below 0°C. Because the latent heat released during freezing is effectively dissipated into the environment, supercooled droplets freeze almost instantaneously upon contact. This rapid solidification traps air bubbles within the ice, creating "rime ice," which is characterized by an opaque appearance, higher porosity, and relatively low density. The second is a wet growth regime. It occurs when the accretion rate of supercooled droplets is so rapid that the latent heat released exceeds the cooling capacity of the environment, causing the surface temperature to reach 0°C. In this state, the collected droplets do not freeze immediately but instead form a liquid film that can flow into the air spaces of the underlying porous layers. This process creates "glaze ice," which is dense and transparent, with few air bubbles. If the liquid water is not fully retained, it may be shed from the particle or produce a "spongy" hailstone structure, where liquid water is trapped within an ice matrix (Lamb and Verlinde, 2011; Markowski and Richardson, 2010).

2.4.3. The role of storm structure

Large hail cannot form without close interaction between microphysics and storm dynamics. The most favorable environment for hail growth is a region where the updraft velocity roughly matches the hailstone's fall speed. This allows the ice particles to remain suspended in the hail-growth zone (HGZ), where supercooled liquid water is abundant, for an extended period (Markowski and Richardson, 2010).

Lamb and Verlinde (2011) distinguished three zones where hail can form effectively. In the embryo-formation zone (EFZ), relatively weak updrafts allow the initial embryos to develop and grow to a diameter of 5 mm or more. In the HGZ stronger updrafts compensate for the increase in gravity force and thus fall speeds of hailstones, while high liquid water content promotes rapid accretion. In the fallout zone (FOZ), the hailstones become too heavy for the updraft, their fall speeds exceed the updraft speed, and they descend to the surface.

In supercell storms, the organized and tilted updrafts allow embryos to remain suspended within the growth for an extended period, creating optimal conditions for the formation of exceptionally large stones. The final size of the hailstone is primarily determined by the concentration of supercooled liquid water and the time it remains within the high-growth

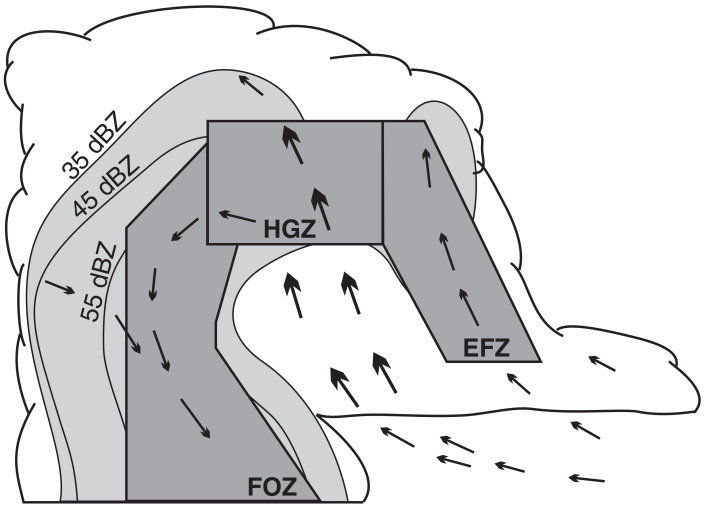

Figure 2.9.: Schematic illustration of hailstone development pathways within a supercell, with arrows indicating wind velocities. Figure by Lamb and Verlinde (2011) adapted from Young (1993).

regions. This residence time is a sensitive balance between the storm's updraft intensity and the hailstone's terminal fall speed, v_t. As the stone remains suspended within the updraft, its fall speed evolves according to its physical properties and the surrounding environment, assuming a spherical and smooth form:

$$v_t = \sqrt{\frac{4g\rho_i D}{3c_d\rho}}, \tag{2.29}$$

where ρ_i is the density of the ice (typically 0.9 g cm^{-3}), D is the particle diameter, and ρ is the ambient air density. The term c_d is a dimensionless drag coefficient (ranging from 0.4 to 1.0) that accounts for the stone's aerodynamic shape and surface roughness. The final size of hail at the ground is also influenced by its descent. As the stone falls through the melting layer (where wet-bulb temperatures are above 0°C), it begins to melt and loses mass. The height of the wet-bulb-zero level and the presence of downdrafts determine the final size of the hailstone. If the wet-bulb-zero level is low or the descent is rapid, larger hailstones reach the surface (Markowski and Richardson, 2010; Lamb and Verlinde, 2011).

Although hail can develop in a variety of deep convective environments, from relatively short-lived single-cell thunderstorms to complex convective systems, the production of large hail is strongly associated with multicell and supercell storms. For hailstone formation, the necessary balance between a stone's increasing terminal fall speed and the updraft velocity is most efficiently achieved within the complex structures of multicells and especially supercells. These storms maintain intense, long-lived updrafts that are often protected from the weakening effects of dry-air entrainment. This allows hailstones to remain suspended for extended periods, ultimately leading to the descent of large, high-density ice particles once their fall speed overcomes the updraft's support (Lamb and Verlinde, 2011; Markowski and Richardson, 2010).

2.4.4. Hail damage

In Europe, hail-producing SCSs are a major cause of economic damage. According to Hulton and Schultz (2024) and Púčik et al. (2019), hailstones exceeding 2–3 cm are the main drivers of devastating impacts, frequently damaging crops and trees, whereas damage to roofs, vehicles, and windows becomes much more frequent for hailstones with a diameter of about 4–6 cm and rises sharply once hail size exceeds 5 cm. The local-scale nature of hailstreaks, combined with high asset exposure, can make individual events especially costly. Moreover, sometimes these hailstreaks can persist over several hundred kilometers (Punge and Kunz, 2016).

In terms of insured losses, these systems have recently evolved into a significant natural hazard in several countries, even surpassing winter storms and floods. Regions across Central and Southern Europe — specifically southern Germany, northern Italy, France, and parts of Spain — experience the highest frequency of intense hailstorms. For Germany in particular, SCS hazards, including hail, severe wind gusts, and lightning, represent the top driver of insured property damage (Punge and Kunz, 2016). Recent reinsurance analyses indicate that 50–80% of total SCS-related damage in the last decade is attributed to hail, making hail the primary component of convective storm losses (Swiss Re, 2023).

Historically, storms, hail, and lightning have accounted for approximately 27% of all European natural hazard losses since 1980. Several prominent hail events, such as the Munich hailstorm of 12 July 1984 and the 2013 “Andreas” storm in Germany, produced multi-billion-dollar losses and rank among the costliest European hail events on record (Punge and Kunz, 2016; Púčik et al., 2019). This trend has only intensified: in 2023 alone, the SCSs’ insured losses across Europe were estimated above USD 5 billion in each year from 2021 to 2023. This was driven heavily by an unprecedented series of hailstorms in Northern Italy that generated a record-breaking USD 5.5 billion in insured losses (Swiss Re, 2023).

Beyond these broad economic impacts, the agricultural sector faces distinct risks, with viticulture being particularly exposed. Even small hail and graupel can cause significant damage to vines. Wine production plays a major role in the local economies of many European wine regions. Italy, France, and Spain alone account for about 34% of the world’s vineyard surface area. The concentration of vineyard areas in these countries indicates that hail risk is not only a local agricultural issue but also affects a significant portion of the global grape-growing area (International Organisation of Vine and Wine, 2025).

Vineyards are highly exposed due to their lack of protective infrastructure and their high sensitivity to physical damage throughout the growing season. In vineyards, hail damage depends strongly on phenological stage: shoots, leaves, bunches, and stems may be bruised, torn, broken, or stripped, while damage to compound and lateral buds can reduce fruitfulness in the following season (Figure 2.10). It may reduce the next year’s crop by approximately 25%. When hail occurs around flowering or later, yield losses depend not only on direct bunch loss, but also on leaf-area reduction, impaired fruit set, berry abortion, delayed recovery, and increased susceptibility of wounded tissue to disease (The Australian Wine Research Institute, 2021).

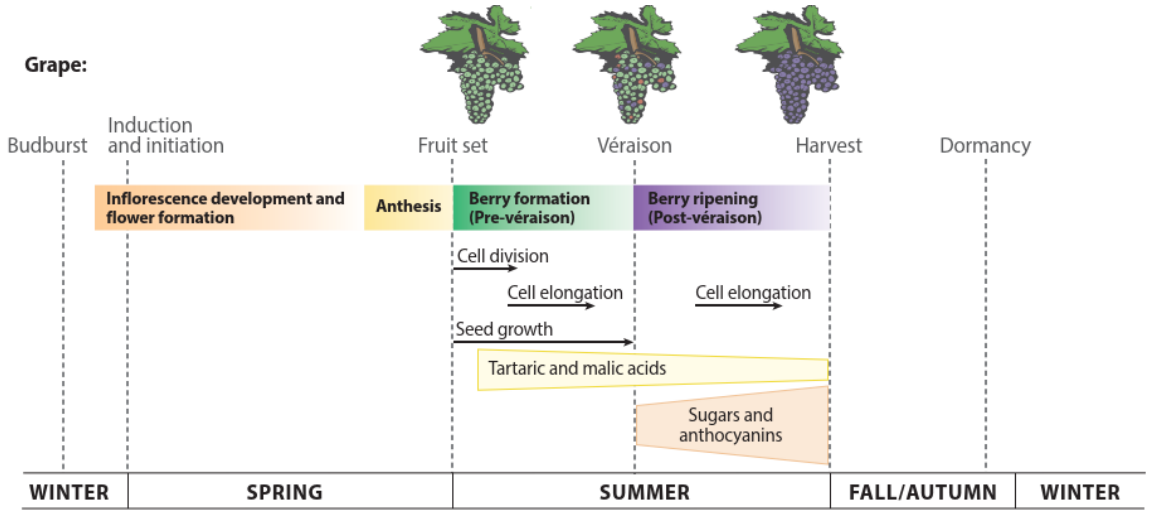

Figure 2.10.: Schematic annual cycle of grapevine phenology, showing the main stages from budburst and flowering to berry formation, veraison, harvest, and dormancy. Adapted from Naidu et al. (2015), modified from Carmona et al. (2008) and based partly on Coombe and McCarthy (2000).

According to the WineRisk project website, hail has already cost the wine industry around 10 billion USD per year, with hail identified as one of the most destructive perils, capable of causing up to 50-90% crop losses in severely affected vineyards (Risklayer GmbH, 2024). A lack of a vineyard-specific, reliable warning or risk assessment system across major European wine-producing regions leaves growers highly susceptible to catastrophic losses.

3. Data and Methods

There are several approaches for assessing hail occurrence and its impacts across different socio-economic sectors. For example, Deepen (2006) developed one of the earliest stochastic hail-damage models for Germany, focusing on automobile insurance losses. In contrast, Berthet et al. (2011) analyzed hailpad observations from the ANELFA network in France to assess seasonal hail intensity in an agricultural context. Radar-based products, such as POH and MESHS, also provide high-resolution information on hail probability and expected severe hail size for hail climatology and agricultural damage-related applications (MeteoSwiss, nd).

While these examples demonstrate the diversity of hail assessment approaches, they are often limited to specific countries, sectors, or observational systems. For this study, datasets were selected to enable a consistent investigation of hail occurrence across a broader European domain (10°W–38°E, 30°N–66°N) and to link this occurrence to agricultural exposure, particularly viticulture. Therefore, this work combines satellite-based OT detections, output from the HAILCAST hail growth model, and ground-based hail reports from the ESWD. This combination allows for the comparison of various representations of hail occurrence. With the exception of specialized physical sensors such as hailpads, all of these datasets serve as indirect proxies for hail rather than direct physical measurements, introducing a relatively high degree of uncertainty. Nonetheless, evaluating a combination of remote-sensing-based proxies, model outputs, and reported ground observations allows for a more comprehensive assessment. HAILCAST is particularly interesting because it has not yet been widely used in European hail-impact studies. Finally, datasets on damaged wineries, wine-growing regions, and insurance information are used to connect hail occurrence with potential impacts on viticulture.

The following sections detail the datasets used in this study and describe the methodological approaches applied to process and analyze these data.

3.1. Overshooting Tops Data

OTs are dome-like protrusions above the surrounding cirrus anvil cloud of deep convective storms. They form when the updraft is strong enough to penetrate above the level of neutral buoyancy and rise into the lower stratosphere. As moist air rises, condensation and freezing release latent heat, which helps maintain and enhance positive buoyancy (Robert A. Houze, 2014; Adler and Mack, 1986). When CAPE is large, the resulting vertical velocities can reach 30-50 m/s or more, allowing the updraft to overshoot its equilibrium level, penetrate the

tropopause, and produce an overshooting top. Such overshooting tops typically persist for about 5-20 minutes and have horizontal scales up to 15 km (Bedka, 2011; Bedka and Khlopenkov, 2016).

Satellites are commonly used to detect OTs. As deep convective cloud tops reach greater altitudes and protrude above the surrounding anvil cloud, their lower cloud-top temperatures can therefore be identified in thermal infrared imagery as locally colder regions embedded within comparatively warmer cirrus clouds. They can also be recognized by their distinctive textured appearance in visible imagery (Adler and Mack, 1986; Bedka and Khlopenkov, 2016; Khlopenkov et al., 2021). The OT data used in this study were derived from measurements of the Meteosat Second Generation (MSG) satellite, operated by the EUMETSAT. The geostationary platforms are used specifically, as they repeatedly observe the same region at short intervals, making them particularly suitable for the consistent detection of rapidly evolving convective features such as OTs. In the European studies of Bedka and Khlopenkov (2016) and Punge et al. (2017), OT detection was based on MSG Spinning Enhanced Visible and Infrared Imager (SEVIRI) infrared window imagery, centered near 10.8 μm.

The infrared (IR) channel provides information on cloud-top temperature by measuring emitted thermal radiation. For a black body, the total emitted radiative flux density F is described by the Stefan–Boltzmann law, according to which the emitted energy per unit surface area and time is proportional to the fourth power of temperature, T:

$$F = \varepsilon \sigma T^4, \tag{3.1}$$

where F is the radiative flux density (W m^{-2}), σ is the Stefan-Boltzmann constant, and ε is a correction factor for grey bodies from the Kirchhoff's law. Accordingly, colder cloud tops emit less total radiation and have their peak emission at longer wavelengths, as described by Wien's displacement law. In longwave infrared satellite imagery, this is expressed through lower brightness temperatures (BTs), which can be used as an indirect indicator of high cloud tops and, therefore, of the likelihood of an OT.

In recent years, the National Aeronautics and Space Administration (NASA) Langley Research Center (LaRC) has improved the detection algorithm, which is capable of identifying candidates in the observed data and assigning to them a probability indicating how likely it is that the detected feature is, in fact, an OT (Bedka and Khlopenkov, 2016; Khlopenkov et al., 2021). Since tropopause temperature varies considerably from region to region, infrared brightness temperatures are converted to tropopause-relative values prior to OT detection. This conversion is performed by normalizing the IR temperature with the "BT-score" parameter:

$$\text{BT Score} = (60 - \text{BTTD}) \cdot 340, \tag{3.2}$$

where $BTTD = BT_p - T_{tpfiltered}$ is a difference in tropopause brightness temperature, BT_p is the brightness temperature of the pixel, and $T_{tpfiltered}$ is the spatially filtered tropopause temperature. The constants 60 and 340 are an offset and scaling factor used to convert the tropopause-relative temperature difference into a BT-score that fits within the range of a 2-byte integer. The filtered tropopause temperature provides a smoother and more stable reference field by reducing localized high-frequency variability and sharp gradients in the

original tropopause temperature field, thereby supporting more robust OT characterization (Khlopenkov et al., 2021).

A candidate for an OT is identified as a cold spot within an anvil cloud (Bedka, 2011). While the anvil clouds appear as a uniform collection of cold pixels in a specific area, an OT visibly disturbs this field. However, anvil identification is not unambiguous, because non-convective cold cloud shields, such as those occurring along fronts in mid-latitude cyclones, can resemble convective anvils in infrared imagery and thus hinder the reliable definition of the OT search region (Scarino et al., 2020). Located cold spots then undergo distance-based verification to ensure each candidate is sufficiently spaced, preventing a single OT from being misidentified as multiple distinct occurrences. Using a custom algorithm, OT candidates are isolated by first identifying true local maxima within a 3×3 window of the BT-score image, then recursively thinning these results via an 11×11 proximity check that retains only the most prominent peaks. This study uses the most recent iteration of the algorithm to generate the dataset; within this framework, the probability score (OT_{prob}) indicates detection certainty, with higher values denoting more robust OT candidates. OT_{prob} is given by:

$$OT_{prob} = 100 TropF^{0.6(1/\lambda - 1)} \tag{3.3}$$

in percent. Therefore, the probability depends on the candidate temperature relative to the tropopause temperature ($TropF$), as well as on λ, which describes the prominence of the OT relative to a large, spatially uniform anvil and is defined as:

$$\lambda = \sqrt{PromF \cdot AreaF \cdot AnvilF}. \tag{3.4}$$

Here, $PromF$ describes the prominence of the cold spot relative to the mean temperature of the surrounding anvil, $AreaF$ represents the size of the anvil area, and $AnvilF$ denotes the measure of spatial uniformity of the anvil temperature. These formulas indicate that an OT should not only be colder than the tropopause, but also relatively colder compared to the surrounding anvil. This means that the normalized IR temperature must be small. In this context, "small" refers to cloud-top brightness temperatures that are near or below the filtered tropopause temperature. Typically, these values associated with OT range from approximately +10 K to -15 K relative to the tropopause. Additionally, pixels that represent the surrounding anvil should be homogeneous around the OT, while the anvil itself should be large, as convection with larger anvils is more likely to produce OTs (Khlopenkov et al., 2021). In order to minimize the amount of falsely detected OTs, only OTs with $OT_{prob} > 0.5$ were used in this analysis. This threshold was established in previous studies as a reliable probability for ensuring that a candidate may represent a physical overshooting top (Khlopenkov et al., 2021; Punge et al., 2023; Giordani et al., 2024).

The OT dataset used in this study is based on post-processed NASA satellite detections of OTs. The original OT product is gridded, whereas the dataset used for this analysis has been converted into a point-based catalog. Each row corresponds to a single OT detection and includes the detection time, latitude, longitude, OT probability, OT temperature difference, and environmental parameters assigned from the nearest fifth-generation European Center for Medium-Range Weather Forecasts Reanalysis (ERA5) atmospheric profile. The detections have a nominal temporal resolution of about 15 min. The available OT data covers the

period from 2004 to 2024. To capture the period of maximum convective activity in Europe, the study focuses on the months of April to September. It is important to keep in mind that OTs represent only a proxy for convection and cannot directly describe hail. To account for this, a filter is applied to the raw detections using ERA5 reanalysis data based on atmospheric conditions. These parameters were compiled by Mateusz Taszarek using the open-source thundeR package, an R-based tool designed for rapid computation of severe-storm parameters from sounding, reanalysis, and numerical weather prediction profiles (Taszarek et al., 2025). The filter is focused on excluding as many OTs as possible that occur in environmental conditions that are unsuitable for hail formation (Punge and Kunz, 2016; Punge et al., 2023). In particular, the filter is based on the following parameters: CAPE, DLS, and freezing level height. The filtering concept follows the approach introduced by Punge and Kunz (2016), while the specific threshold values were updated using environmental distributions associated with hail-related reference datasets.

CAPE and DLS are closely linked to the likelihood of severe convection, while a high freezing level increases the chance that hailstones melt before reaching the surface. However, there is no clear definition of the melting-level height above which a hailstone melts, since the melting process depends on factors such as hailstone size and the thermodynamic profile below cloud base. The thresholds for these ambient parameters were defined and adjusted to the new data based on Punge and Kunz (2016), Punge et al. (2023), and were subsequently adapted to the updated dataset following personal communication with Fischer (Fischer von zur Gathen, 2026). In the current work, OT detections were filtered using ERA5 environmental thresholds of Most Unstable CAPE $MUCAPE > 50$ J kg^{-1}, bulk shear > 1 m s^{-1}, and freezing level height between 1600 and 4400 m (Punge et al., 2023). Using this method $\approx 25\%$ of the data was removed.

ERA5 provides an improved temporal and vertical resolution, with hourly output on a 0.25° horizontal grid and is available at 137 native model levels. The environmental parameters used here are based on ERA5 output variables and pressure-level data. This is particularly relevant to convective parameters such as CAPE and CIN that are sensitive to the temperature profile in the troposphere. These environmental thresholds, applied using ERA5-based variables, allow for a more temporally consistent characterization of rapidly varying convective environments. Nevertheless, reanalysis-based convective diagnostics remain subject to uncertainty, particularly in the boundary layer and in instability-related fields, because deep convection is a subgrid-scale process (Punge and Kunz, 2016; Taszarek et al., 2020b).

3.2. HAILCAST Data

HAILCAST is a one-dimensional (1D) hail growth model that can be combined with several driving models. In the present study, HAILCAST is implemented as an online diagnostic within the climate version v6 of the non-hydrostatic Consortium for Small Scale Modeling (COSMO) model (Baldauf et al., 2011). It provides an estimate of maximum hail diameter at the ground, from which hail occurrence and spatial patterns can be derived. In the

European kilometer-scale simulations presented by Cui et al. (2025) and Thurnherr et al. (2025), the model is embedded in a convection-permitting framework with a nested setup of 12 km in the outer domain and 2.2 km in the inner domain, where convection is treated explicitly, and hail diagnostics are calculated online. In this study, HAILCAST output from the convection-permitting inner COSMO domain with a horizontal grid spacing of 2.2 km is used. In the COSMO implementation, HAILCAST is activated at each grid point every 5 minutes if the modeled updraft speed exceeds 10 m s^{-1} for at least 15 minutes. Once active, HAILCAST simulates the development of hail embryos with starting diameters of 5, 7.5, and 10 mm during adiabatic ascent. HAILCAST simulates the maximum hail diameter at the ground from vertical atmospheric profiles from COSMO, and stores the resulting maximum hail diameter at 5 min intervals.

HAILCAST does not explicitly represent hail; it is a proxy for hail size and distribution that incorporates several physical approximations. Since it operates in a 1D vertical column, the complex dynamics within the convective cloud are not accounted for. In this framework, hailstones are assumed to fall in straight lines, which is inconsistent with the reality of complex trajectories in the three-dimensional flow of convective systems.

Despite the detailed output, the studies by Cui et al. (2025) and Thurnherr et al. (2025) indicate that the model tends to underestimate very large hail, particularly those sizes exceeding approximately 50 mm, which are generally underrepresented. This issue has been linked to the possible underestimation of updraft strength in the model setup. It can also miss short-lived strong updrafts within the 5 min time window (Cui et al., 2025; Thurnherr et al., 2025).

In this study, post-processed HAILCAST data from the 2011-2021 simulation period are used. This data has a temporal resolution of 5 min and provides the estimated maximum hail diameter at the ground for each grid point. It covers large parts of Europe, with the approximate spatial extent shown in Figure 3.1. The data were provided by Daniell (2025).

3.3. Observational Data

ESWD data

To assess the performance of the proxy data, this study utilized quality-controlled severe weather reports from the (available at www.eswd.eu; (Dotzek et al., 2009)). Maintained by the European Severe Storms Laboratory (ESSL), the ESWD is a pan-European database that provides detailed information on severe weather events, including hail, in a common data format. The dataset combines observations from different sources, including national meteorological services, voluntary observer networks, the ESSL staff, media reports, and public reports, which are then processed through a structured, multi-stage quality-control procedure (Dotzek et al., 2009; Groenemeijer et al., 2017).

In this work, hail reports covering the period from 2011 to 2021 were used. Consistent with the database's definition of large hail adopted in previous studies, only reports with a

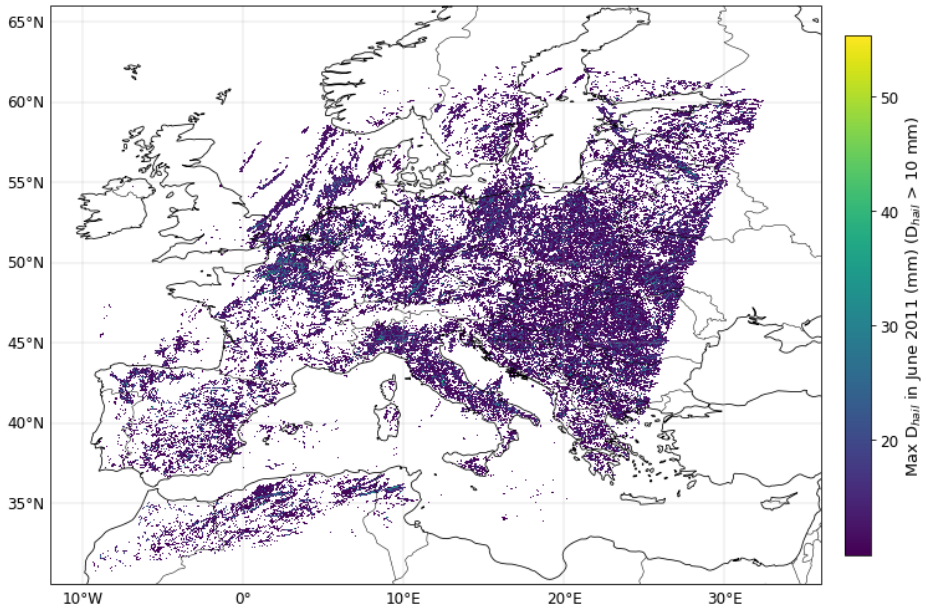

Figure 3.1.: Example of the HAILCAST dataset showing the maximum simulated hail diameter in June 2011, considering only hail diameters larger than 10 mm.

reported hail diameter of at least 2 cm were retained. Furthermore, only reports with quality flags QC1 and QC2 are considered to ensure the analysis is based on reports that have been confirmed or fully verified. The quality control levels are defined as follows: QC1 refers to reports that have been confirmed by a reliable source, such as a meteorological service or a trusted observer, while QC2 is assigned to events that have been fully verified and for which the available information is considered reliable and consistent. (Dotzek et al., 2009; Punge and Kunz, 2016). By cross-referencing these ground-based reports with proxy data, such as OT detections and HAILCAST outputs, this study assessed spatial discrepancies and the degree of agreement between the proxies and reported hail occurrence and diameter.

It is important to acknowledge that reports have limitations for the direct validation of model-derived hail climatologies, primarily due to their non-uniform spatial distribution across Europe. The number of reported hail events is significantly higher in densely populated areas, creating a reporting bias that likely understates hail occurrence in sparsely populated or remote regions, including mountainous areas. (Dotzek et al., 2009; Groenemeijer et al., 2017). Although the number of ESWD reports has increased in recent years, making the data more reliable, the dataset remains affected by pronounced geographical differences in report density. Additionally, the dataset is biased toward daytime events when severe weather is more likely to be observed and reported (Punge et al., 2017; Taszarek et al., 2020a).

CATDAT database

A major challenge in this field is the lack of a centralized record for vineyard damage. Often, available reports provide only a broad overview of a storm's impact, failing to capture

the vineyard-level details necessary for an accurate case study. Therefore, the case study analysis focuses on the most significant hail events within the defined study period.

To support a comprehensive assessment of hail impacts, this study uses damage data from wineries affected by convective hail events, together with corresponding insurance claims. As previously established, viticulture is among the agricultural sectors most vulnerable to natural hazards globally; even small hailstones can cause significant crop damage and fruit degradation. Consequently, the wine industry incurs annual losses of several billion dollars due to weather- and climate-related hazards (Petoumenou et al., 2019; International Organisation of Vine and Wine, 2025).

To evaluate the spatiotemporal accuracy of hail detection and forecasting systems at the local scale, confirmed hail events affecting selected wine regions were identified, thereby providing a reliable framework for high-resolution case studies. For the case study a dataset compiled jointly by Daniell (2025) and the author was used. The CATDAT database was constructed through the aggregation of information from multimedia archives, journalistic records, digital reports, and insurance data.

ISMEA insurance data

To evaluate the HAILCAST and OT datasets, agricultural insurance records were obtained from the open service portal of Istituto di Servizi per il Mercato Agricolo Alimentare (ISMEA). ISMEA is an Italian public institution that provides information, financial services, and risk management tools for the agricultural sector. Italy is regularly affected by hail, making Italian insurance data a valuable resource for the study of hail frequency and intensity. According to a review by Punge and Kunz (2016), Southern Europe—and northern Italy in particular—exhibits some of the highest hail frequencies recorded in Europe.

The collected dataset specifically focuses on subsidized agricultural insurance (Assicurazioni Agricole Agevolate), covering the period from 2011 to 2021. It contains detailed information on the following variables: sum insured (Valore Assicurato in €), total premium (Premio Totale in €), insured product (Prodotto), province (Denominazione Provincia), year (anno), and coverage package (Pacchetto di Garanzie), which identifies the specific insurance policy and the types of protection included.

While the data does not specify the individual hazard events that triggered damage claims, it provides high-resolution information on the spatial distribution of insured losses, particularly for wine grapes. This allows for a robust analysis of spatial and temporal loss patterns in Italian viticulture.

3.4. Evaluation

3.4.1. Definition of Hail Days

To analyze the frequency and spatial distribution of hail across different datasets, individual events are aggregated into a standardized temporal unit known as the 'hail day'. Because

the available hail proxies describe the hail occurrence through different physical variables, converting these outputs to a uniform 'hail day' metric facilitates a scientifically accurate comparison across the European domain.

In this study, a hail day is defined as the 24-hour period spanning from 06:00 UTC to 06:00 UTC the following day, which aligns with previous works (Cui et al., 2025; Thurnherr et al., 2025). This time frame is selected to capture the entire lifecycle of daily convective systems within a single reporting window, thereby avoiding the artificial separation of storm events occurring over night (Cui et al., 2025).

In the HAILCAST output, a grid cell is classified as having a hail day if the simulated maximum hail diameter is greater than or equal to 10 mm ($D \geq 10$ mm) at any time during a defined 24-hour period. Depending on the analysis, this classification is applied either to the 10 km × 10 km grid or to the 100 km × 100 km grid. The 10 mm threshold was selected as it corresponds to the lower bound of the small-hail category considered by Thurnherr et al. (2025). Additional test plots using a lower threshold of 5 mm showed a noisier spatial structure, but did not substantially alter the main spatial patterns (see Appendix A). Therefore, the 10 mm threshold was retained for the analysis. To ensure scientific accuracy, these HAILCAST outputs are post-processed using an artifact-filtering algorithm to remove false hail signals, including cases in which strong upslope flow over steep terrain triggers the diagnostic rather than actual convective activity. This filtering algorithm specifically removes HAILCAST activations that do not coincide with precipitation, as hail is physically expected to occur in the vicinity of rain (Cui et al., 2025).

Additionally, HAILCAST hail days are further divided by hail diameter to distinguish between different hail-size categories and their potential agricultural damage. "Small hail days" are defined as hail days where the simulated maximum diameter is between 10 and 12.5 mm. "Intense hail days" are defined for diameters between 12.5 and 20 mm. The lower bound of 12.5 mm was selected because, over the Alpine region, it yielded the closest agreement between simulated mean hail-day frequency and radar-based observations (Thurnherr et al., 2025). "Severe hail days" are defined as those with a maximum hail diameter exceeding 20 mm. This limit represents a threshold for large hail in Europe, above which significant damage to infrastructure is expected (Thurnherr et al., 2025).

For the OTs proxy, hail-day occurrence is defined using a threshold number of detected overshooting tops within the 24-hour analysis window. In this study, a hail day is defined as a day on which 1 or more OTs are detected in a 10 km x 10 km grid cell. For larger grid cell sizes of 100 km x 100 km, this limit increases to 2 OTs per grid cell.

For ESWD reports, if at least one report is recorded within a grid cell (for both 10 km × 10 km, or 100 km × 100 km grid) during the 24-hour period, that day is considered a hail day for that specific cell. This binary conversion provides a consistent event-based metric, although ESWD reports remain affected by reporting biases related to population density and temporal variations in reporting frequency.

3.4.2. Categorical Verification

Categorical verification is a method used to test the performance of different predictors. In meteorology, it is commonly used to evaluate the quality and accuracy of non-probabilistic forecasts for discrete events, such as thunderstorms or hail occurrence (Wilks, 2006; López et al., 2007; Kunz, 2007).

This approach is primarily centered on constructing a 2 × 2 contingency table, that classifies events and serves as the basis for calculating various measures of accuracy and quality, commonly referred to as skill scores. This allows for a quantitative assessment of the degree of agreement between different predictors (proxies). This table separates event occurrence and non-occurrence into four outcomes: hits (a), where the event was both predicted and observed; false alarms (b), where the event was predicted but not observed; misses (c), where the event occurred but wasn't predicted; and correct negatives (d), where neither a prediction nor an occurrence took place (Wilks, 2006).

Table 3.1.: Contingency table for categorical verification.

		Observation	
		YES	NO
Forecast	YES	*a*	*b*
	NO	*c*	*d*

In this study, the 2 × 2 contingency table compares the presence or absence of hail days as indicated by OTs and HAILCAST for 100 km × 100 km grid cells across the entire study area, and 10 km × 10 km for separate countries. The study also includes comparisons of ESWD with both HAILCAST and OTs separately. The analysis was performed for each grid cell and each day during April–September over the period 2011–2021. A hit (a) is recorded when both proxies indicate a hail day in the same grid cell. A false alarm (b) occurs when HAILCAST indicates a hail day, but OTs do not. A missed event (c) is defined when the OT proxy indicates a hail day, but HAILCAST does not. A correct negative (d) is assigned when both proxies indicate no hail day for the same grid cell. Based on this table, verifications measures such as the Probability of Detection (POD), False Alarm Ratio (FAR), Heidke Skill Score (HSS), and Critical Success Index (CSI) are calculated to quantify the agreement between three datasets and to assess how consistently hail occurrence is represented across the study domain.

Probability of Detection, POD

One of the most common verification measures is the POD, which describes the fraction of observed events that were correctly forecast (Wilks, 2006). In this study, POD measures the fraction of OT-indicated hail occurrences that are also successfully captured by HAILCAST, as well as the fraction of ESWD reports captured by both hail indicators. POD is given as:

$$POD = \frac{a}{a + c} \tag{3.5}$$

POD ranges from 0 to 1. A POD of 0 means that none of the hail days identified in the reference dataset are detected by the compared dataset, while a POD of 1 means that all reference hail days are detected. Therefore, higher POD values indicate a better ability of the compared dataset to capture hail occurrences identified by the reference dataset.

False Alarm Ratio, FAR

FAR indicates the proportion of positive forecasts that were incorrect. So it describes the fraction of hail days indicated by one dataset that are not confirmed by the other one:

$$FAR = \frac{b}{a+b}, \tag{3.6}$$

with $0 \leq \text{FAR} \leq 1$. High FAR values indicate that many detected hail days in the compared dataset are not found in the reference dataset for the same day and grid cell.

Heidke Skill Score, HSS

HSS is a skill score used in meteorological verification that evaluates overall agreement between the compared sources while accounting for the agreement expected by chance. It is specifically used for events such as hail and tornadoes, where most cases fall into the correct-negative category.

$$HSS = \frac{2(ad - bc)}{(a+c)(c+d) + (a+b)(b+d)}, \tag{3.7}$$

with $-1 \leq \text{HSS} \leq 1$. Values close to 1 indicate a perfect agreement between data sources, whereas negative values indicate very poor agreement. Values around 0 correspond to no skill beyond random agreement. Negative values indicate worse agreement than expected by chance and therefore very poor performance.

Critical Success Index, CSI

In this study, CSI evaluates the agreement between HAILCAST and the OTs, and ESWD and HAILCAST/OTs by relating joint hail detections to all grid cells for which hail is indicated by at least one of the two proxies:

$$CSI = \frac{a}{a+b+c} \tag{3.8}$$

Unlike HSS, the CSI does not include correct negatives and therefore focuses on the cells relevant to hail occurrence. CSI ranges from 0 to 1, where 0 indicates no successful agreement in hail-day detection and 1 indicates perfect agreement.

4. Results

This chapter presents an analysis of the datasets used in this study, focusing on their respective characteristics and differences. The annual and seasonal variability, and diurnal cycle of hail occurrence are examined for HAILCAST model output, OTs, and ESWD reports. Furthermore, multiple verification approaches are applied to assess the degree of agreement and consistency among different hail indicators. In addition, this chapter includes case studies focusing on selected high-impact hail events at the local scale. This approach allows for a detailed evaluation of the spatial agreement between the hail indicators and ground-based observations.

4.1. Dataset analysis

Because the three primary datasets used in this study differ significantly in their nature — directly observed data from ESWD, modeled maximum hail diameters from HAILCAST, and satellite-based OTs as an indirect proxy for hail-favorable SCSs — the initial analysis focuses on spatial and temporal hail day distributions. This first step establishes a baseline for comparing hail frequencies across the datasets.

To examine hail occurrence frequency across the three datasets, the calculated hail-day fields on the 10 km × 10 km grid were aggregated to European administrative regions. For this purpose, the European Nomenclature of Territorial Units for Statistics (NUTS-3) was used, which represents the most detailed regional level. For each day and each NUTS-3 administrative unit, a hail day was assigned if at least one 10 km × 10 km grid cell within that unit indicated hail occurrence. The total number of regional hail days from 2011 to 2021 during April-September was calculated and then divided by the number of years to determine the average annual number of hail days for each administrative unit (Figure 4.1).

The resulting distribution (Figure 4.1) shows a clear difference between the three datasets. ESWD has the lowest mean annual hail-day occurrence per administrative unit, with most regions experiencing only 1 to 3 hail days per year. This is consistent with the point-based and report-dependent nature of the dataset, where hail occurrence may be missed in regions with lower population density. OTs exhibit higher frequencies than ESWD, yet the distribution remains more concentrated in the lower-to-moderate ranges. HAILCAST shows a wider distribution, extending to significantly higher values, with certain areas experiencing more than 40 mean annual hail days during the April to September season.

Subsequently, the same regional values were mapped to assess how the mean annual number of hail days per administrative unit varies spatially across Europe. The spatial distributions

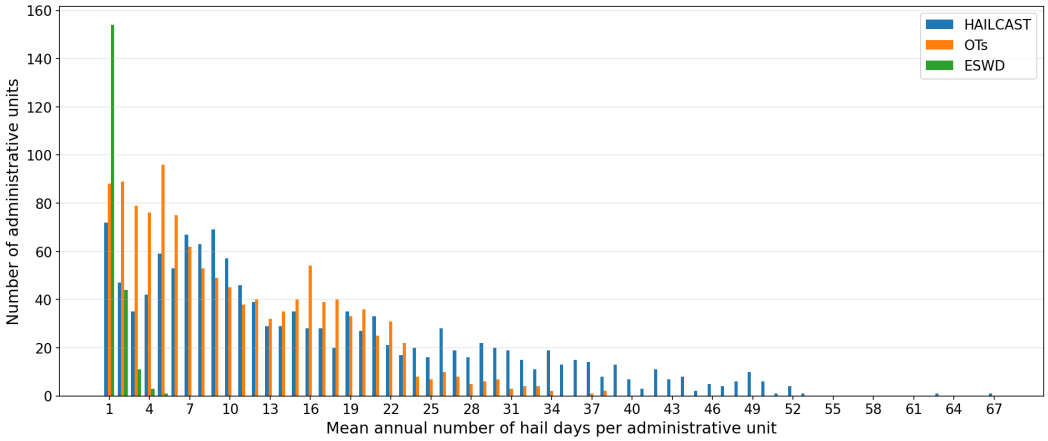

Figure 4.1.: Mean annual number of hail days per European administrative region for HAILCAST, OTs, and ESWD datasets, from April to September 2011-2021.

of mean annual hail-day occurrence across NUTS-3 administrative regions for HAILCAST and OTs show broadly similar large-scale patterns (Figure 4.2). Both datasets show a higher hail-day frequency in several well-known hail-prone regions, including the Alpine region, the Pyrenees, northeastern Spain, northern Italy (including the Po Valley), and parts of southeastern Europe and the Balkan Peninsula. Overall, this spatial distribution is consistent with previous studies (Punge and Kunz, 2016; Taszarek et al., 2020b).

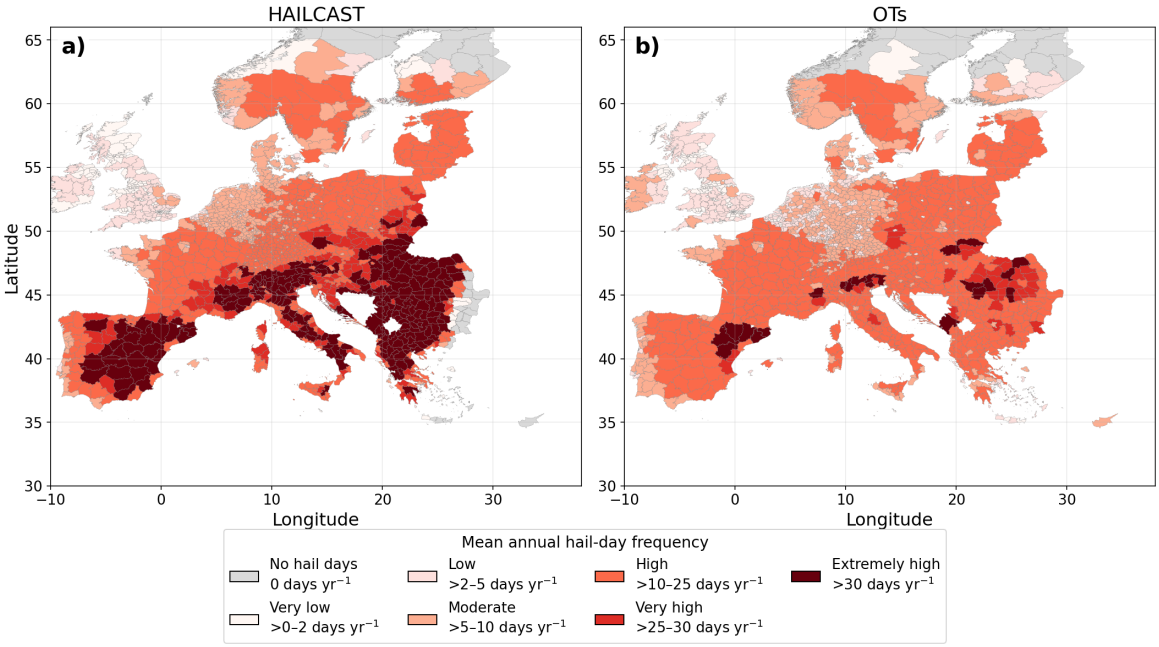

Figure 4.2.: Spatial distribution of the mean annual number of hail days per NUTS-3 administrative region for HAILCAST (a) and OTs (b) during April–September of the 2011–2021 period.

Despite these broad similarities, according to HAILCAST, there are more areas with mean annual hail-day frequencies of "high" to "extremely high" compared to the OTs (Figure 4.2).

This pattern is particularly pronounced across northern and central Italy, the Alpine foreland, the Iberian Peninsula, and southeastern Europe, where frequencies exceed 25–30 days yr^{-1} and, in some regions, 30 days yr^{-1}. In contrast, the OT-based distribution is more localized, with peak values concentrated within a few regions. These include parts of northern Italy, especially Piemonte, Lombardia, Veneto, Emilia-Romagna, and Friuli-Venezia Giulia; northeastern Spain, particularly Catalonia, Aragon, Navarra, and La Rioja; and parts of the Balkan Peninsula.

Both datasets also show lower mean annual hail-day occurrence over large parts of northern and north-western Europe. This north-south contrast is consistent with the general European severe convection pattern, where large hail and severe convection are generally less frequent farther north (Punge and Kunz, 2016).

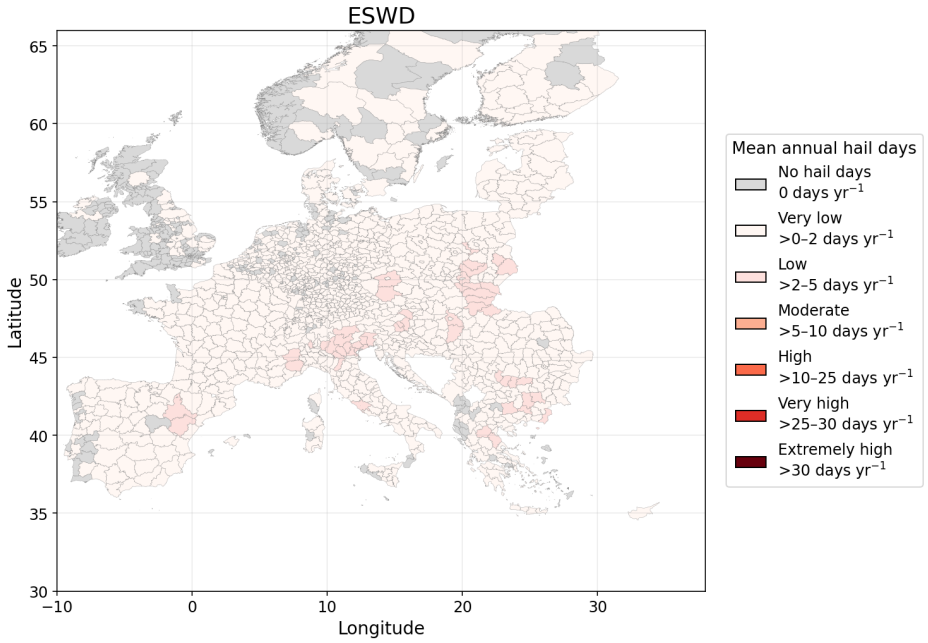

Figure 4.3.: Spatial distribution of the mean annual number of hail days per NUTS-3 administrative region for ESWD during April–September of the 2011–2021 period.

The ESWD map shows much lower values overall, as expected from the previous distribution analysis (Figure 4.3). Most NUTS-3 regions fall into the no-hail or very-low classes, reflecting the point-based and report-dependent character of ESWD. Nevertheless, the same spatial signals remain visible over northern Italy and parts of central and southern Europe. This supports the interpretation that ESWD identifies the main hail-prone regions, although it shows significantly lower occurrence numbers compared to HAILCAST and OTs.

To further examine the spatiotemporal variability of the hail-days, yearly maps were produced for the 2011-2021 period. For each year, the total number of hail days from April to September was calculated for every NUTS-3 administrative region. These maps make it possible to assess the interannual variability of hail-day occurrence and to examine whether the main hail hotspots recur across years and are consistently represented in all three datasets.

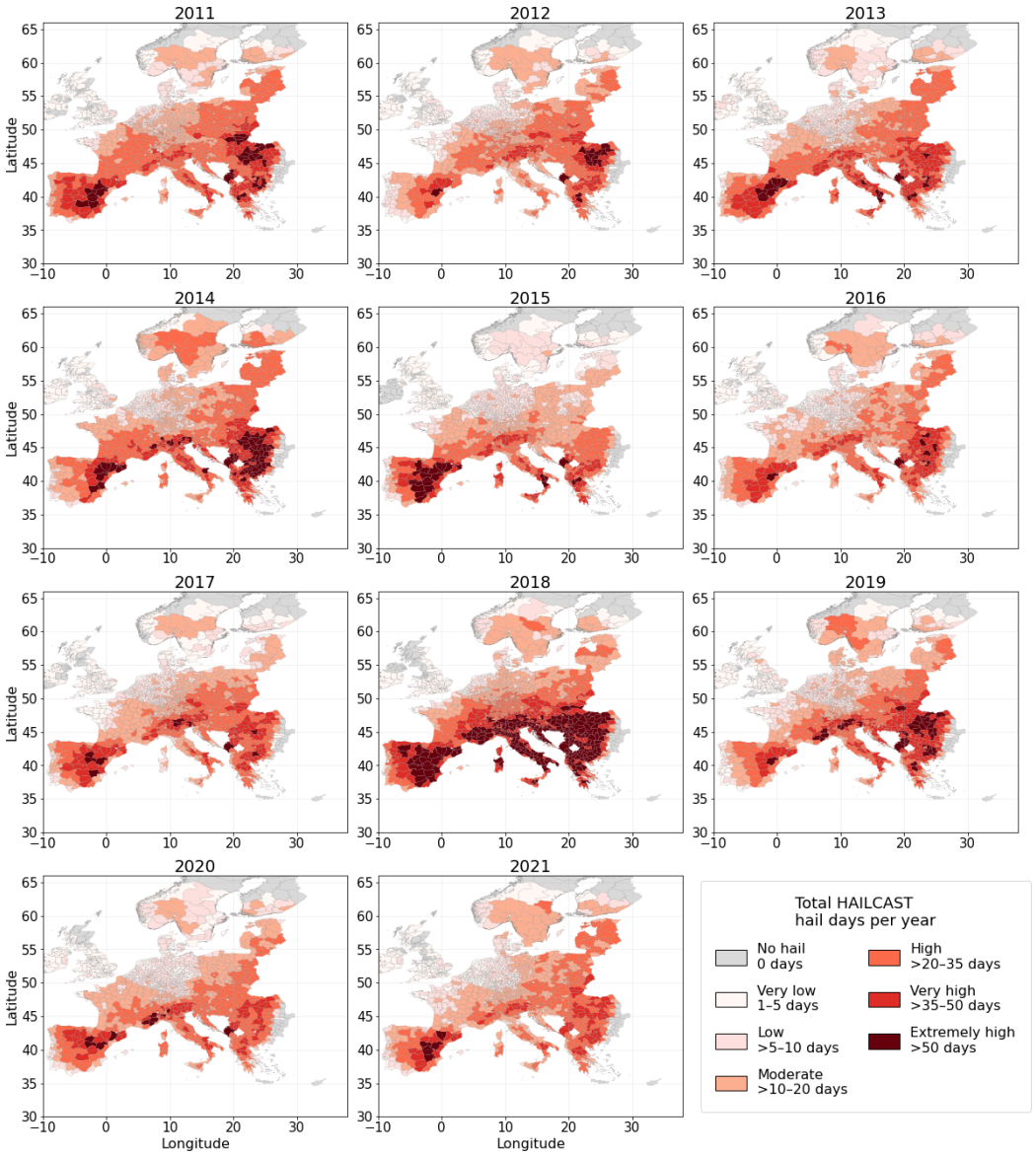

Figure 4.4.: Interannual variability of total HAILCAST hail days per NUTS-3 administrative region during April–September, 2011–2021.

The resulting maps show recurring spatial patterns across all three datasets throughout the 2011-2021 period, although the magnitude and spatial extent of hail-day occurrence vary by year and dataset. HAILCAST shows the highest annual hail-day totals (Figure 4.4). Over the years, much of southern and southeastern Europe has fallen into the "high" to "extremely high" categories, with many administrative regions experiencing more than 20-35 hail days yr^{-1}. Regions falling into the highest class, with more than 50 hail days yr^{-1}, include north-eastern Spain, particularly the Iberian System and the Ebro valley, Northern Italy, the Alpine region, and the Balkan Peninsula.

The OT-based maps exhibit a similar large-scale structure; however, areas with high annual hail-day totals are less widespread than in HAILCAST (Figure 4.5). The highest totals of OT-

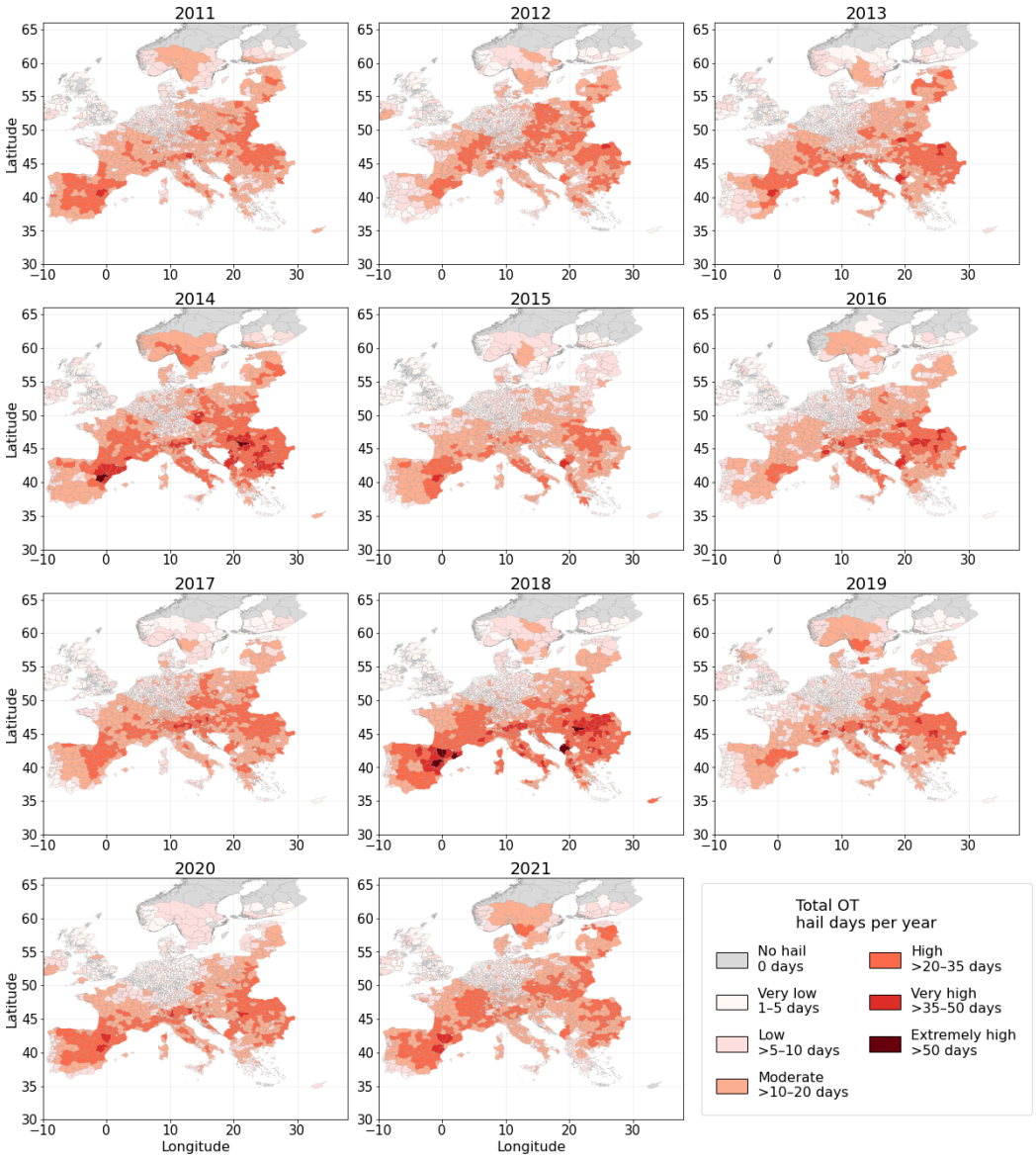

Figure 4.5.: Interannual variability of total OTs hail days per NUTS-3 administrative region during April–September, 2011–2021.

derived hail days (> 20-35 hail days yr^{-1}) are primarily found in regions known for frequent hail occurrences, including northeastern Spain, northern Italy, and parts of southeastern Europe. As in Figure 4.4, there is a distinct maximum of hail activity in 2018, captured by both HAILCAST and OTs hail proxy. This spatial pattern remains broadly consistent with previous European hail climatologies, which identify enhanced hail activity in the same regions (Punge and Kunz, 2016; Taszarek et al., 2020a).

In contrast, ESWD shows much lower annual hail-day totals than HAILCAST and OTs (Figure 4.6). Most administrative units remain in the "no hail", "low" or "moderate" classes, corresponding to 0–3 hail days yr^{-1}, while values above 3 hail days yr^{-1} are only found in isolated areas. Since the ESWD analysis is based on quality-controlled reports, it can serve

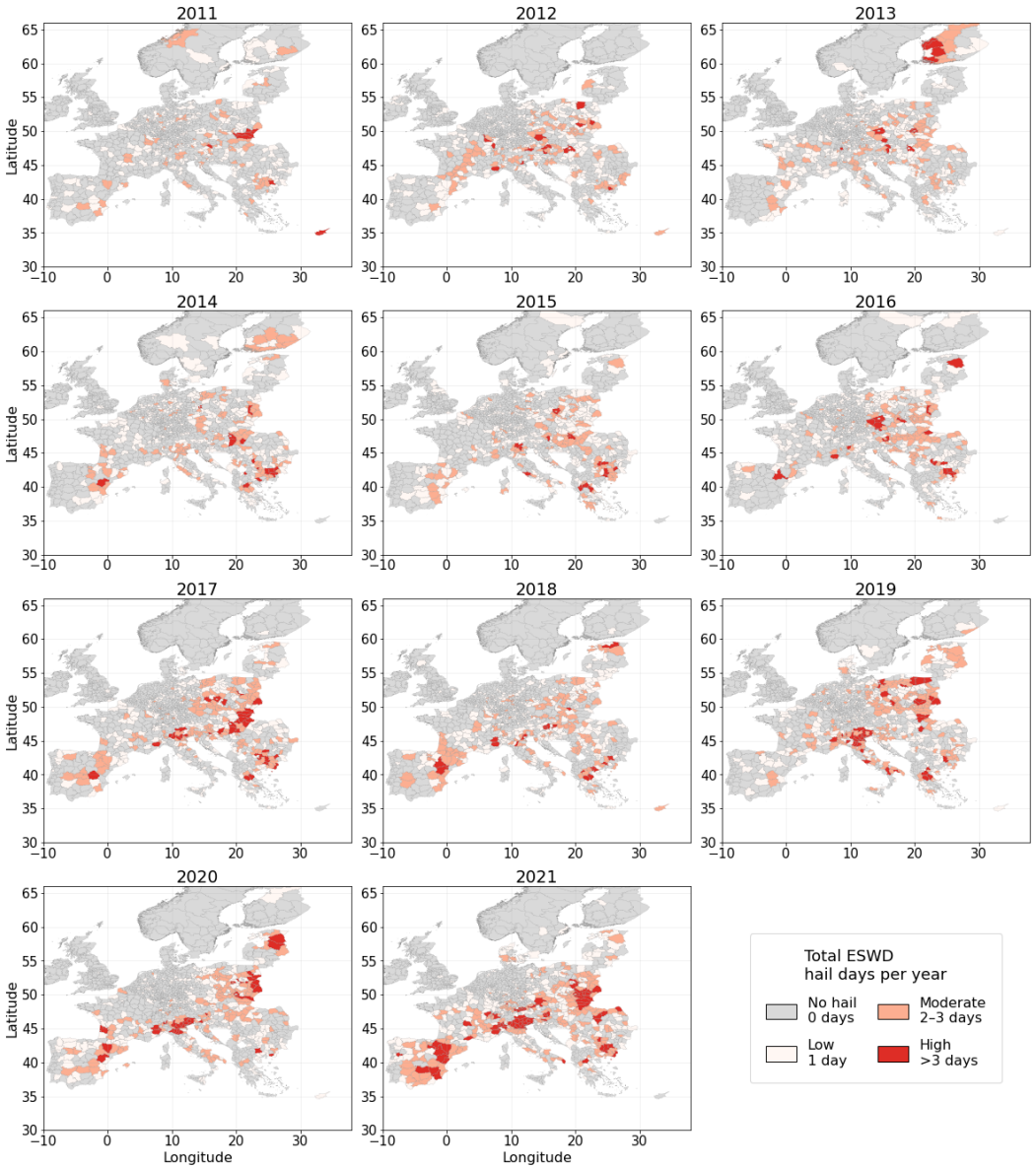

Figure 4.6.: Interannual variability of total ESWD hail days per NUTS-3 administrative region during April–September, 2011–2021.

as an observational reference for assessing the spatial plausibility of the HAILCAST- and OT-based patterns. However, because ESWD is report-dependent and spatially incomplete, it is not suitable as a direct quantitative benchmark for hail-day counts. Despite the lower values, several areas classified as "very high" and "extremely high" in the OTs (Figure 4.5) and HAILCAST (Figure 4.4) maps are supported by the reports. This suggests that regions with pronounced hail activity are captured correctly by both HAILCAST and OTs, even though both of the datasets indicate substantially higher hail-day totals than ESWD.

However, while all three datasets indicate generally lower hail activity over large parts of northern Europe, ESWD shows almost no reported hail days in several regions where

HAILCAST and OTs still indicate hail occurrence, for example, northern Germany, parts of central and northern Spain, the British Isles, and the Scandinavian Peninsula. In addition, the pronounced maximum visible in HAILCAST and OTs in 2018 is not clearly reflected in the ESWD maps. Hail days in ESWD are derived from individual ground reports and are therefore affected by reporting density, observer availability, population distribution, and possible daytime reporting biases. As a result, ESWD is not spatially or temporally homogeneous and cannot be interpreted as a complete record of hail occurrence.

The apparent increase in ESWD of the total number of hail days over the study period should therefore also be interpreted with caution (Figure 4.6). This increase may be partly due to improved reporting efficiency and broader spatial coverage, rather than to a purely meteorological increase in hail activity. For this reason, ESWD serves as an observational reference to evaluate whether the main spatial patterns identified by HAILCAST and OTs are physically plausible, rather than as a direct quantitative benchmark for hail-day frequency.

4.2. Seasonal variability

The seasonal cycle of hail occurrence was analyzed for ESWD reports, HAILCAST-derived hail estimates, and OTs detections. The goal is to evaluate the consistency of seasonal variability across these datasets for the European region. The monthly variation in hail activity is also relevant for viticulture, since grapevine susceptibility to hail damage varies with the phenological stage.

Following the spatial aggregation described in section 4.1, monthly hail-day totals were calculated for each NUTS-3 administrative region. A region was counted as having a hail day when at least one 10 km × 10 km grid cell within the region indicated hail occurrence on that day. The monthly totals were then averaged separately for each calendar month over the 2011–2021 period to obtain the mean number of hail days per month. This approach allows a comparison of the seasonal hail cycle across datasets, while also demonstrating how hail-day frequency varies regionally across Europe. The class intervals used for the monthly maps were defined based on the HAILCAST distribution, as HAILCAST shows the highest mean number of hail days per month per NUTS-3 administrative region (see Appendix A). Lower class intervals were used for the ESWD dataset to better represent its regional variability, as it contains substantially fewer hail days.

All three datasets (Figure 4.7–4.9) exhibit a pronounced and consistent seasonal cycle. Hail-day counts in each dataset increase from April to June, reaching an overall peak in June, followed by a gradual decline toward September. However, some individual regions show maximum hail activity in July, most notably the Alpine region, where this delayed peak is visible across all three datasets. This pattern is consistent with established climatologies of SCSs in Europe, where the peak occurs during late spring and summer (Punge and Kunz, 2016; Taszarek et al., 2020a). This delayed Alpine maximum may therefore be linked to the regional influence of orography, as previous studies report later hail peaks at higher

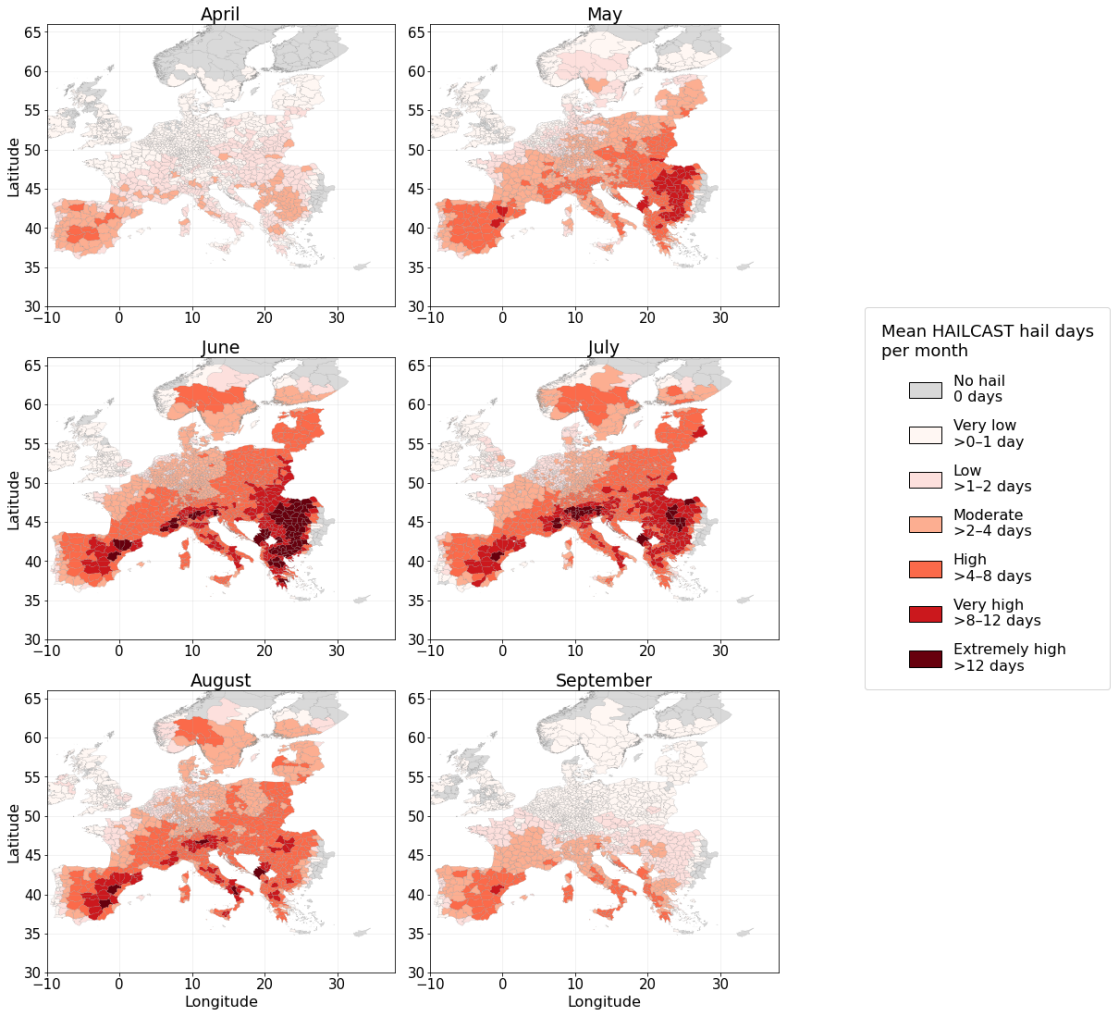

Figure 4.7.: Monthly mean hail-day frequency according to HAILCAST per NUTS-3 administrative region during the months of April to September from 2011 to 2021.

elevations and show that terrain-induced lifting and convergence can support convective initiation near mountainous regions (Punge and Kunz, 2016; Kirshbaum et al., 2018).

While there is an overall agreement in seasonal behavior, differences in magnitude and temporal evolution are evident between the datasets. The HAILCAST data shows the highest total number of hail days (Figure 4.7), with a pronounced peak in June and continued elevated activity through July and August. This is particularly evident over the Balkan region, across most of Italy, and in northeastern Spain. This indicates that the hail-favorable conditions are represented over a relatively extended period in the model output. The OT-based dataset shows a clear overall peak in activity during June (see Figure Figure 4.8). However, several regions continue to exhibit sustained or locally increased activity in July. This includes the Alpine region, which mirrors trends observed in HAILCAST, as well as southern Scandinavia and parts of northeastern Europe, such as Poland and the Baltic countries. After July, the mean hail-day frequency decreases more rapidly, with a noticeable reduction in August and a further decline in September. This sharper seasonal decline aligns with the idea that OTs

serve as indicators of intense convective updrafts, which are most common during the main convective season (Punge et al., 2017).

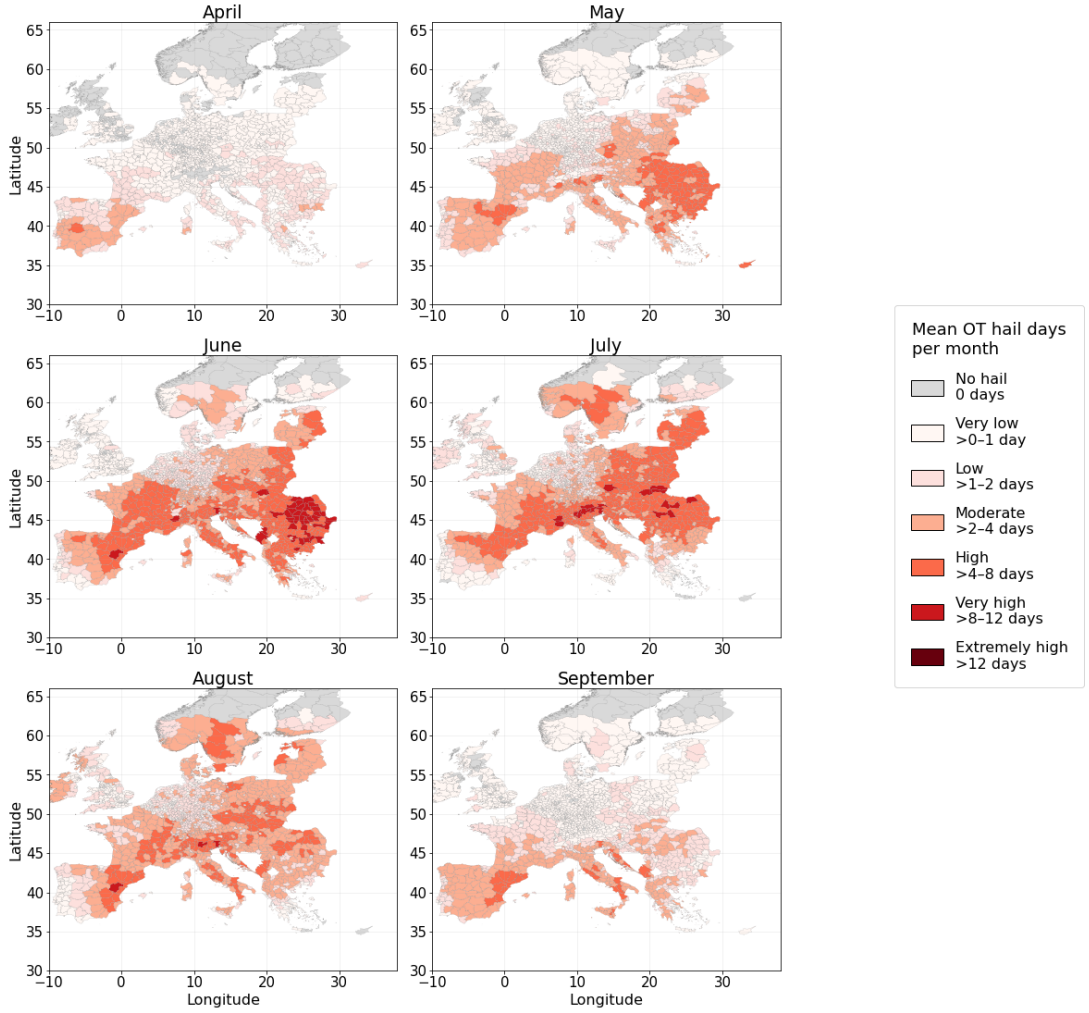

Figure 4.8.: Monthly mean hail-day frequency according to OTs per NUTS-3 administrative region during the months of April to September from 2011 to 2021.

The ESWD dataset follows a similar seasonal evolution (Figure 4.9), although the mean number of hail days per month is substantially lower overall. In comparison to HAILCAST and OTs, the ESWD signal exhibits greater spatial localization. However, increased activity remains evident in parts of the Alpine region, certain areas in the Balkans, and northeastern Spain. These areas broadly correspond to regions of elevated hail activity in the two proxy datasets. This is consistent with the known limitations of observational datasets (Taszarek et al., 2020a). In addition, the decrease from July to September is more pronounced compared to HAILCAST and OTs, indicating a shorter observed hail season.

Overall, the temporal evolution of hail occurrence is consistent across all three datasets, highlighting a common seasonal trend that begins with an increase in spring, peaks in early summer, and subsequent declines. This agreement indicates that, despite the differences in

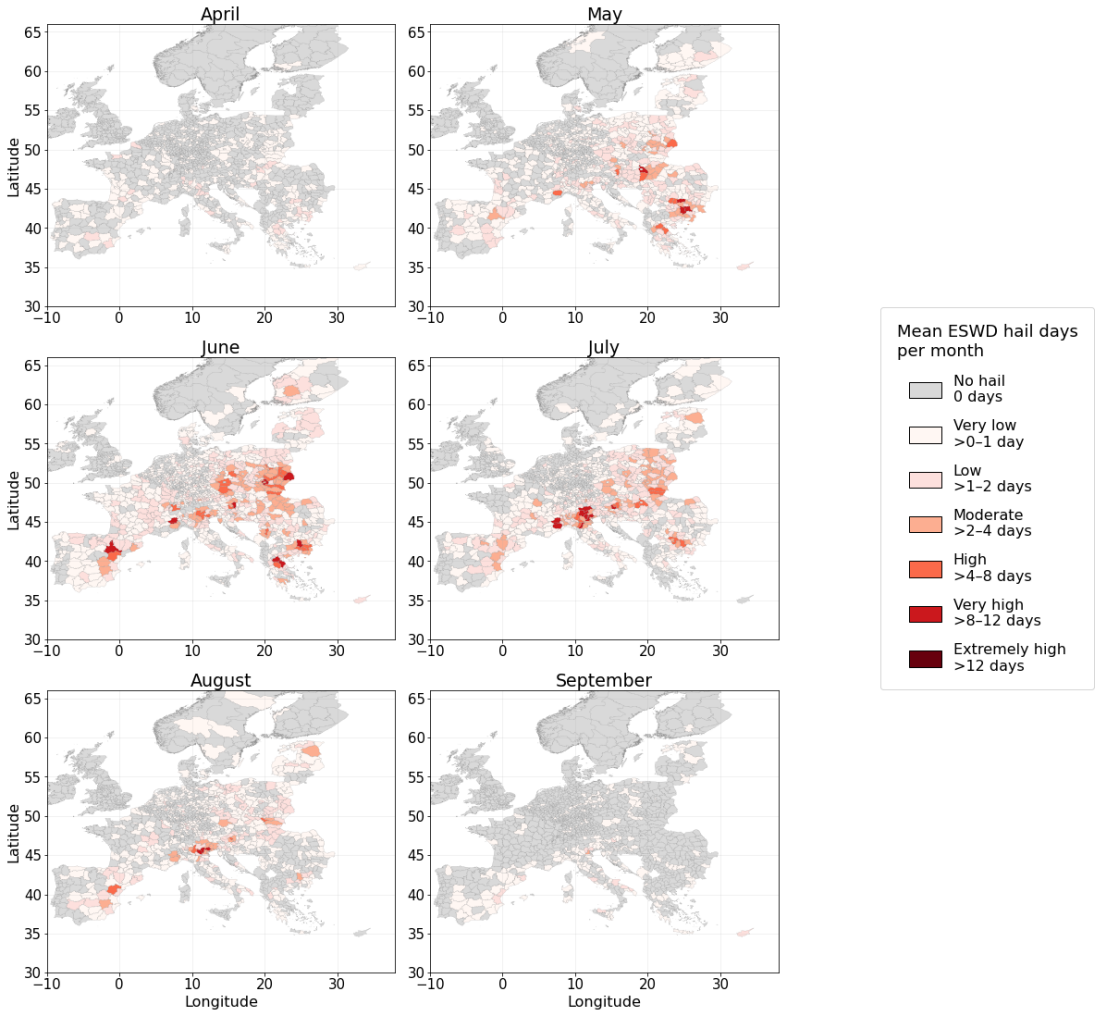

Figure 4.9.: Monthly mean hail-day frequency according to ESWD reports per NUTS-3 administrative region during the months of April to September from 2011 to 2021.

data sources and methodologies, all datasets capture the same large-scale seasonal variability in hail occurrence across Europe.

Year-by-year maps for individual months were also inspected to assess possible temporal changes in hail activity. For this purpose, the total number of hail days was calculated separately for each month, year, and NUTS-3 administrative region. No clear trend is visible over the 2011–2021 period. Instead, the maps support the previously identified year-to-year variability, with enhanced hail activity in some years and weaker activity in others. The main regions of increased hail occurrence remain broadly consistent between months and years. Due to the relatively short 11-year period, these maps are interpreted as supporting evidence for interannual variability rather than a robust trend analysis (see Appendix A).

4.3. Diurnal cycle

To further assess the temporal variability of hail occurrence, the diurnal cycle was analyzed. To account for the longitudinal variation in solar forcing across the study domain, the time coordinates of all datasets were converted from UTC to an approximate local solar time based on longitude. The analysis was restricted to the European land domain defined by the NUTS-3 regional boundaries, excluding points located outside these polygons. For better comparability, all datasets were aggregated to an hourly resolution and expressed as mean values over the study period (2011-2021) for April-September, resulting in a climatological diurnal cycle.

Due to a difference in the data structure, the absolute values are not directly comparable. Unlike the point-based ESWD and OT datasets, the HAILCAST diurnal cycle is derived from gridded model output. It is created by counting the number of instances in which the simulated hail diameter exceeds a defined threshold (10 mm) at each grid point and time step. For each hour, these occurrences are aggregated and averaged across all days, yielding a metric that represents the mean number of HAILCAST points per hour. This measure, therefore, reflects how often the hail threshold is exceeded, rather than the number of independent hail events. This leads to smoother, systematically higher values than the point-based datasets, as hail signals at individual grid cells contribute multiple counts within a given hour. However, this difference influences only the magnitude of the values and does not affect the temporal evolution of the diurnal cycle.

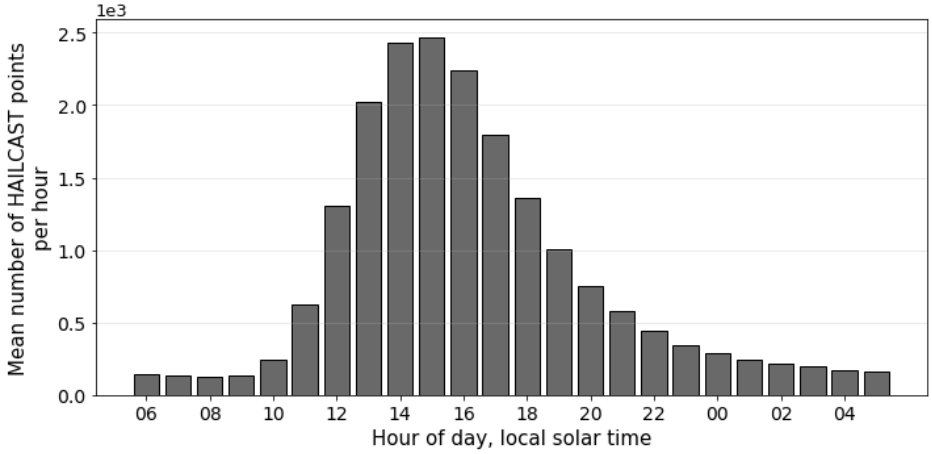

Figure 4.10.: Mean diurnal cycle of HAILCAST hail days, April–September 2011–2021. Hours are defined relative to a 06–06 UTC day.

Despite these differences, all three datasets exhibit a consistent diurnal pattern (Figure 4.10–4.12). The hail-related signals increase from late morning, reach a maximum in the afternoon, approximately between 14:00 and 16:00 local time, and decrease towards the evening, with low but non-zero values persisting into the nighttime hours. Differences between the datasets are mainly reflected in the shape and magnitude of the distributions. HAILCAST shows a relatively broad peak from around 13:00 to 17:00 hours (Figure 4.10). The OT dataset

exhibits a similar, slightly smoother diurnal evolution with a maximum around 15:00 local solar time while maintaining noticeable activity later in the day (Figure 4.11). In contrast, the ESWD data show a more pronounced peak around 16:00 local solar time, followed by a sharper decline after the afternoon maximum (Figure 4.12).

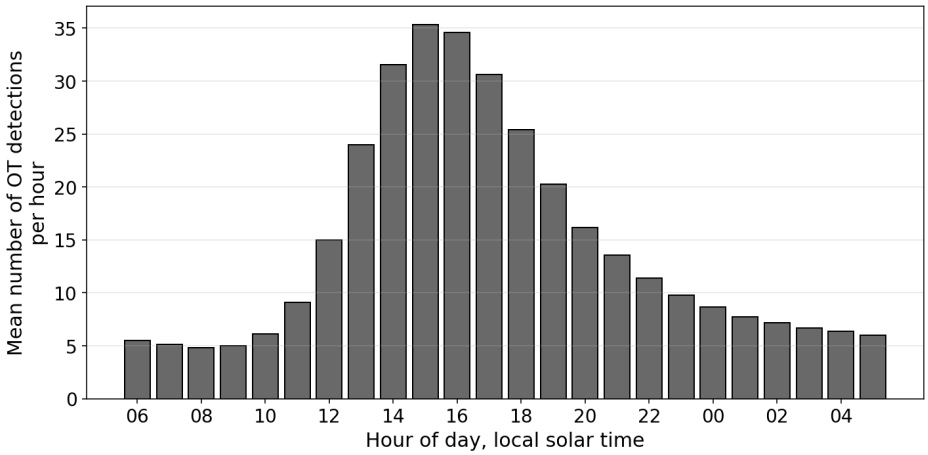

Figure 4.11.: Mean diurnal cycle of OTs detections, April–September 2011–2021. Hours are defined relative to a 06–06 UTC day.

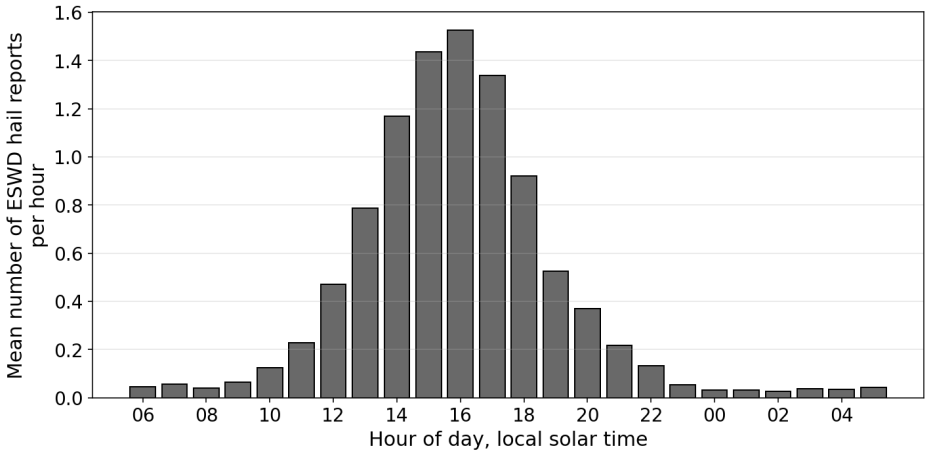

Figure 4.12.: Mean diurnal cycle of ESWD hail reports, April–September 2011–2021. Hours are defined relative to a 06–06 UTC day.

These discrepancies can be explained by the different nature of the datasets. ESWD reports face observational limitations because hail reports rely heavily on human observations, which tend to decrease at night. The overall lower number of reports can also be attributed to reporting bias related to population density, accessibility, and public awareness. Although OTs serve as a satellite-based indicator for intense convection and strong updrafts, they do not guarantee that hail will reach the ground. This can result in a smoother and more continuous diurnal distribution than in ESWD, as OT detections represent broader patterns of deep convective activity rather than confirmed hail reports. The substantially higher HAILCAST values are primarily due to the high spatial resolution of the original gridded

model output, which produces a much denser set of points than the point-based OT and ESWD datasets.

Overall, the diurnal cycle analysis reveals a consistent daily evolution of hail activity across Europe, with increasing values in the late morning, a peak in the early to mid-afternoon, and a decline towards nighttime. This behavior reflects the typical development of convection over land (Taszarek et al., 2020b). The peak between 14:00 and 16:00 local solar time is consistent with previous European studies, which found that hail and severe convective hazards often reach their maximum during the afternoon, when diurnal heating enhances instability in the boundary layer and supports the development of deep convection (Punge and Kunz, 2016; Taszarek et al., 2020b). All three datasets exhibit a similar diurnal cycle, indicating strong agreement in their temporal behavior.

4.4. Categorical verification of spatial hail occurrence

While the annual and seasonal variability analysis indicates a high degree of similarity in the large-scale spatial patterns of hail occurrence between the two proxies, a more detailed assessment at the daily grid-cell level reveals significant discrepancies. To quantify this, categorical verification was applied by classifying each daily grid-cell comparison between HAILCAST and OTs, and ESWD and HAILCAST/OTs as a hit, false alarm, miss, or correct negative.

For the analysis across the entire European domain, elements of the contingency table were summed over all grid cells and all days in the 2011–2021 period (Table 4.1). The resulting verification metrics indicate a generally low level of agreement between the HAILCAST and OTs. The POD (POD = 0.374) suggests that a large fraction of hail occurrences identified by the OT proxies are not captured by HAILCAST. At the same time, FAR (FAR = 0.725) indicates that a considerable number of HAILCAST detections are not supported by OT signals.

Table 4.1.: Categorical verification metrics for the European domain (2011–2021), derived from contingency table classifications of daily hail occurrence at the grid-cell level, based on comparisons between HAILCAST and OT detections (2011–2021).

Metric	POD	FAR	HSS	CSI
Europe (total)	0.374	0.725	0.287	0.188

This combination of low POD and high FAR results in low HSS (0.287) and CSI (0.188), both of which indicate limited overall skill in accurately representing daily hail occurrence at the grid-cell level. In particular, the low CSI indicates that only a relatively small fraction of all hail events are correctly matched between the two datasets.

Additionally, the same analysis was performed for the entire European domain using different simulated HAILCAST hail-size classes to determine whether the agreement with

OT detections improves when only larger simulated hailstones are considered. Here, "small hail" refers to simulated maximum hail diameters ranging between 10 and 12.5 mm, "intense hail days" to diameters between 12.5 and 20 mm, and "severe hail days" to diameters exceeding 20 mm. As shown in Table 4.2, POD, HSS, and CSI decrease with increasing HAILCAST hail-size class. This shows that considering only larger simulated hail diameters results in fewer HAILCAST hail days being retained and reduces the spatial-temporal overlap with OT detections. Although FAR also decreases, suggesting that the remaining HAILCAST detections are less frequently classified as false alarms, this improvement is not sufficient to compensate for the stronger reduction in detected hits. Overall, the results indicate a decrease in categorical skill for the more severe HAILCAST hail size classes.

Table 4.2.: Categorical verification metrics for the European domain (2011–2021), derived from contingency table classifications of daily hail occurrence at the grid-cell level, based on comparisons between OT detections and different HAILCAST hail-size classes.

HAILCAST class	POD	FAR	HSS	CSI
Small (10 mm $\leq D_{hail} <$ 12.5 mm)	0.374	0.724	0.287	0.188
Intense (12.5 mm $\leq D_{hail} <$ 20 mm)	0.320	0.701	0.282	0.183
Severe ($D_{hail} \geq$ 20 mm)	0.211	0.648	0.243	0.152

In addition to the European-wide analysis, verification was also performed for the four countries previously identified as most frequently affected by hail: Italy, Spain, France, and Germany. This was done to assess regional variations in the agreement between HAILCAST, OTs, and ESWD. To examine seasonal variability, verification metrics were calculated for each month and country by aggregating the contingency table elements across all years and over the 100 km × 100 km, 20 km × 20 km, and 10 km × 10 km grid cells within each country (Figure 4.13–Figure 4.15). This approach ensures statistically robust estimates while preserving the seasonal pattern.

On the 100 km × 100 km spatial scale, the resulting monthly metrics exhibit a clear seasonal dependence, with broadly similar values across all countries (Figure 4.13). In general, prediction skill is lowest during April and September, which is consistent with relatively low POD values (e.g. in April from 0.295 in Italy to 0.436 in Spain) and high FAR (typically between approximately 0.7 and 0.85). During the peak convective months (June - August), POD increases across all regions, reaching values above 0.7 in Italy and Spain, while France and Germany remain at comparatively lower levels. At the same time, FAR decreases, particularly in Germany and France, reaching 0.600 and 0.586, respectively, in July. Despite this, HSS and CSI remain relatively low, with only a small increase. This indicates that while the detection improves during the hail peak months, the overall agreement between HAILCAST and OTs remains limited when evaluated at the individual grid cell level on a daily basis.

When the verification metrics are calculated at the 10 km × 10 km grid-cell level, a weak seasonal signal is still visible, with slightly higher POD, HSS, and CSI values during the summer months (Figure 4.14). However, compared with the coarser 100 km × 100 km aggregation, the categorical skill is substantially reduced. POD remains low for all countries

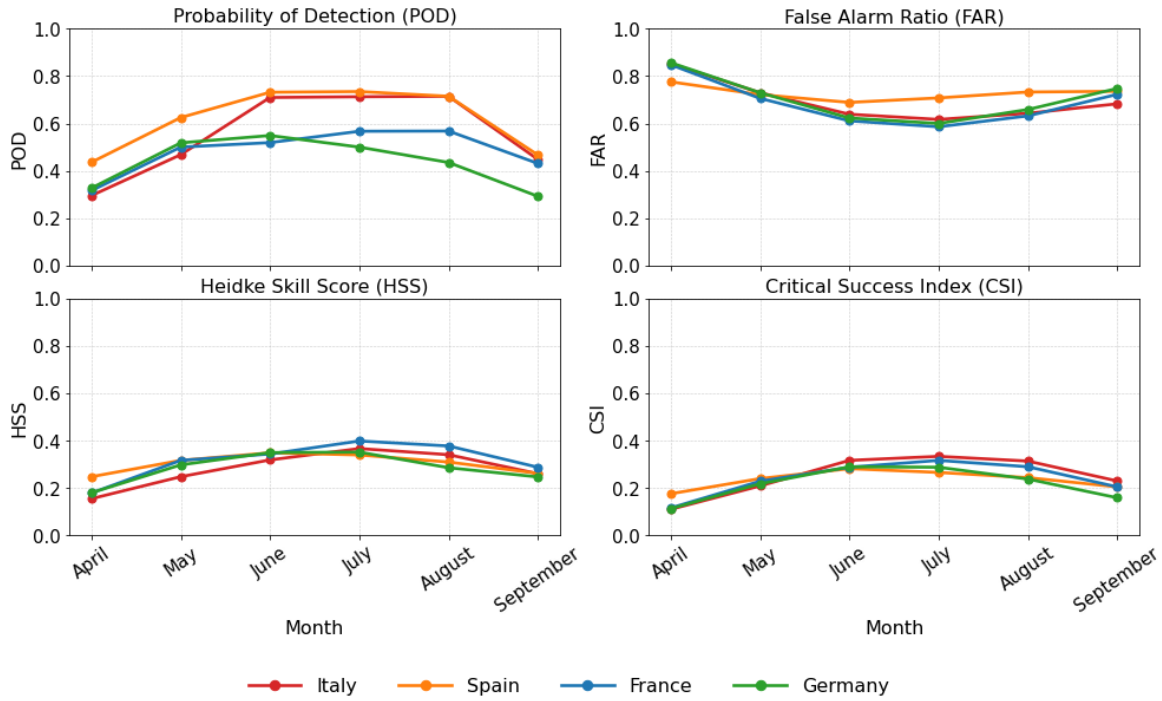

Figure 4.13.: Monthly climatological verification metrics for Germany, France, Italy, and Spain (2011–2021). Metrics are based on contingency table classifications of daily hail occurrence at the 100 km × 100 km grid-cell level, aggregated by calendar month across all years.

and months, while FAR is very high, indicating that most HAILCAST hail-day grid cells are not matched by OT detections at the same location and day. HSS and CSI also remain close to zero, suggesting only very limited spatial-temporal agreement between HAILCAST and OTs at this finer resolution. This indicates that, although the seasonal cycle is still broadly represented, the direct grid-cell-level correspondence between the two hail proxies becomes very weak at 10 km resolution. To further test whether this reduction in agreement is related to spatial scale, the analysis was additionally repeated on a 20 km × 20 km grid. The results confirmed that the categorical agreement between HAILCAST and OTs decreases with increasing spatial resolution (Appendix A).

Overall, the results demonstrate that, although both hail signals capture similar large-scale spatial patterns, their agreement is substantially reduced at a finer spatial and temporal scales. This inconsistency likely reflects fundamental differences between the model-based representation of hail occurrence in HAILCAST and the satellite-based detection of hail-prone convective activity using OTs.

Additional sensitivity tests using different OT thresholds indicate that increasing the threshold leads to higher POD, as weaker and potentially less reliable OT detections are removed. However, this is accompanied by a substantial increase in the FAR, while both HSS and CSI decrease. This indicates that the apparent improvement in detection is achieved at the expense of reliability and overall agreement. This behavior is consistent not only for Europe as a whole, but also at the regional scale, although the magnitude of the changes varies

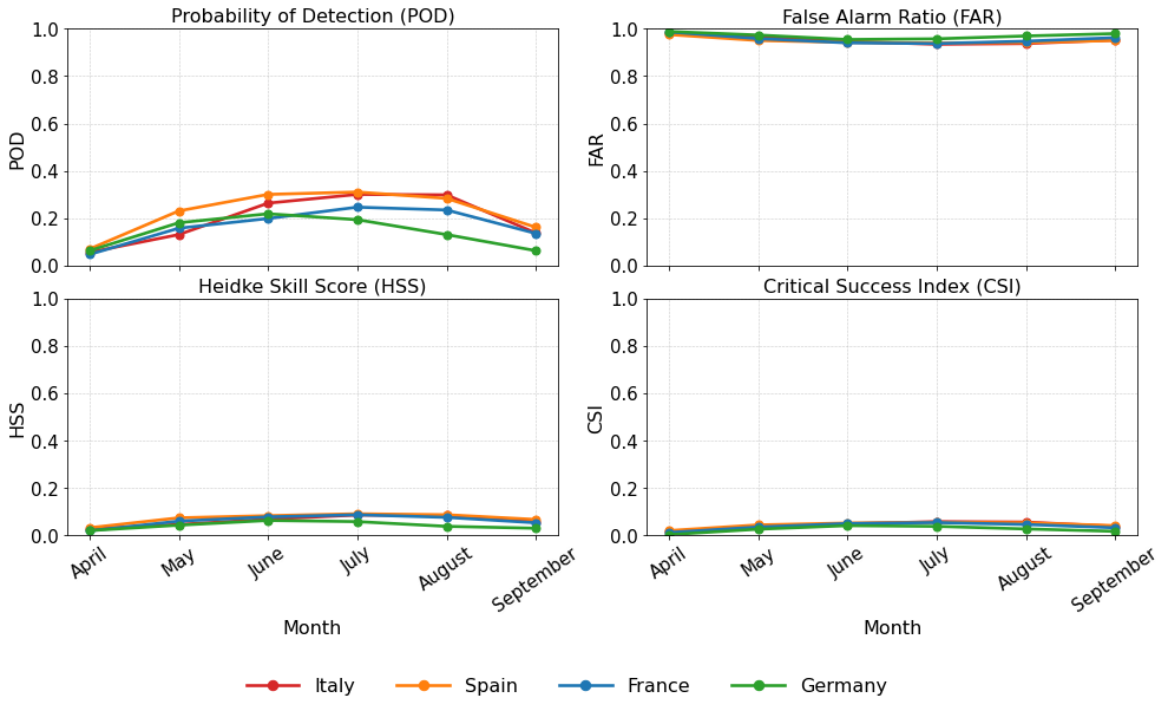

Figure 4.14.: Monthly climatological verification metrics for Germany, France, Italy, and Spain (2011–2021). Metrics are based on contingency table classifications of daily hail occurrence at the 10 km × 10 km grid-cell level, aggregated by calendar month across all years.

across regions. For the European domain, the original configuration therefore provides the most balanced performance, whereas higher OT thresholds mainly emphasize a trade-off between detection capability and false alarms.

The next step was to evaluate the agreement between the quality-checked ESWD hail reports and OTs and HAILCAST, separately. For this purpose, contingency tables were calculated for four selected countries using 20 km × 20 km grid cells. As an example, Figure 4.15 shows the monthly HSS for ESWD vs. OTs and ESWD vs. HAILCAST.

Overall, the HSS values indicate that the agreement between ESWD and the satellite-based OT detections is consistently higher than the agreement between ESWD and HAILCAST. The highest values occur in summer, particularly in June and July, which is consistent with the main hail season. However, all HSS values remain below 0.1, indicating very weak skill and suggesting that the agreement between the datasets is not substantially better than random agreement. The lower HSS values for ESWD vs. HAILCAST suggest that exact spatial and temporal matching is challenging at this grid-cell scale, as ESWD reports are localized point observations, whereas HAILCAST represents hail occurrence over gridded areas and may miss the reported location even when hail is simulated nearby.

A corresponding verification was also performed on a 10 km × 10 km grid. The results indicate even lower agreement, suggesting that skill decreases as spatial resolution increases. This is expected, as a finer grid requires a more precise spatial overlap between the datasets, while ESWD reports, OTs, and HAILCAST represent hail occurrence in fundamentally

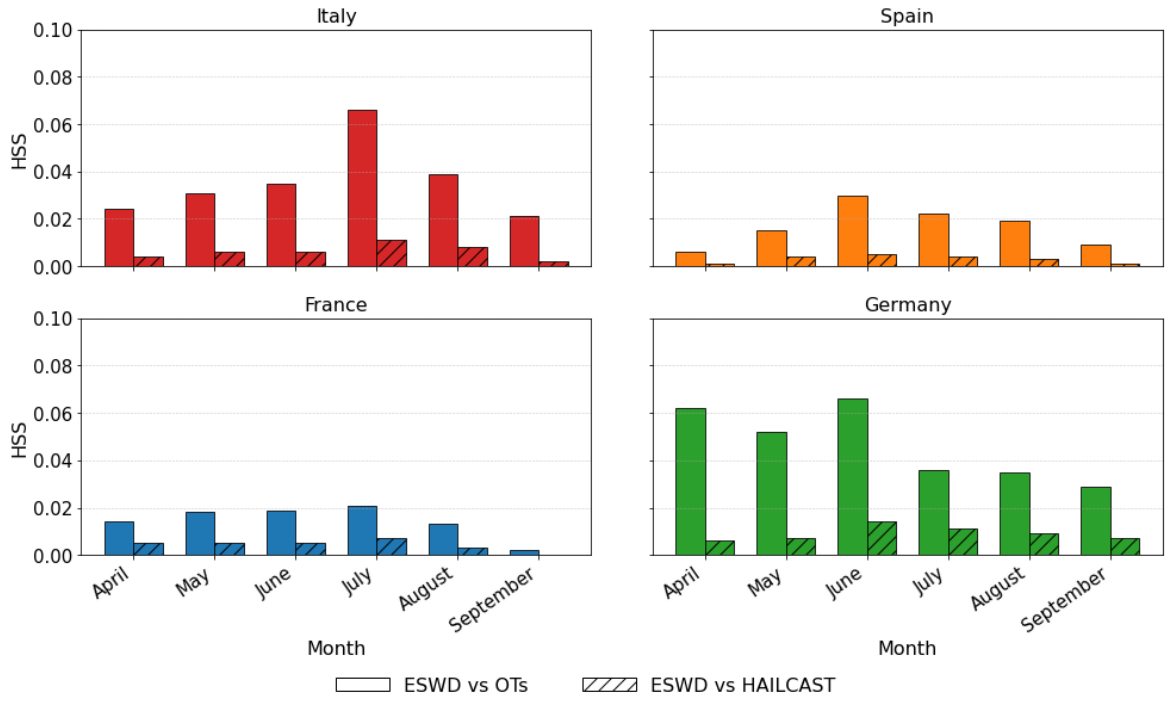

Figure 4.15.: Monthly climatological HSS comparing ESWD reports with OTs and HAILCAST for Italy, Spain, France, and Germany during 2011–2021. HSS values are calculated from contingency tables of daily hail occurrence on a 20 km × 20 km grid and aggregated by calendar month across all years.

different ways. Thus, the weak HSS values reflect the difficulty of matching point-based reports, satellite-based convective signals, and modeled hail occurrence at small spatial and temporal scales.

An additional assessment was performed to examine whether ESWD hail reports are consistent with the OT probability signal. For this comparison, ESWD reports were matched with nearby OT detections using a temporal window of ±30 minutes and a spatial radius of 25 km. These thresholds account for possible time delays between the OT signal and hail reaching the surface, as well as storm motion and downshear displacement.

The results show that larger reported hail diameters are generally associated with higher OT probabilities (Figure 4.16). This suggests that severe hail formation is more closely linked to intense, deep convection, whereas smaller hail can also occur in storms with lower OT probabilities. This relationship is physically plausible, as larger hailstones typically require stronger and more persistent updrafts. The observed increase in OT probability with hail diameter, therefore, supports the validity of OTs as an indicator of intense deep convection and potential severe hail occurrence.

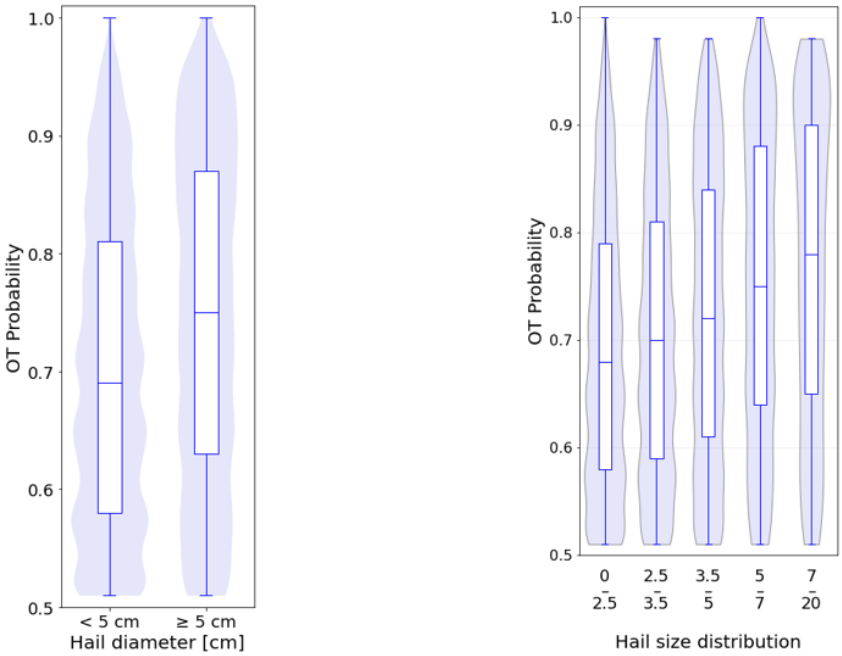

Figure 4.16.: Distribution of OT probability for ESWD hail reports grouped by hail diameter. The left panel compares reports below and above the 5 cm threshold, while the right panel shows the distribution across individual hail-size classes.

4.5. Spatial aggregation of hail days over major wine-producing countries

As discussed previously, vineyards are among the most vulnerable areas of the agricultural sector. Therefore, the following analysis focuses on the main European wine-producing regions and investigates hail-day occurrence in selected countries where viticulture is both spatially extensive and economically important. The European Union is the world's leading wine-producing region. In 2023, it accounted for 44% of the global vineyard area and more than 60% of worldwide wine production, while its average annual production between 2020 and 2025 reached 157 million hectolitres (mhl) (European Commission, 2025).

Using the European vineyards dataset provided by Daniell (2025), the spatial distribution of vineyards across Europe was mapped (Figure 4.17). The resulting distribution reveals a pronounced concentration of vineyards in Italy, southern and south-western France, Spain, Portugal, south-western Germany, and parts of the Balkan Peninsula. Based on spatial patterns and the fact that these countries contain several regions strongly affected by hail activity (Punge and Kunz, 2016), four countries were selected for further analysis: Italy, Spain, France, and Germany. These countries account for a substantial share of European viticulture, making them particularly suited for evaluating the occurrence of hail days over vineyard-rich regions. According to the preliminary estimates of OIV (2025), global wine production reached approximately 232 mhl in 2025, while EU production was estimated at

around 140 mhl. Among the main European producers, Italy produced 47.4 mhl, France 35.9 mhl, Spain 29.4 mhl, and Germany 7.3 mhl.

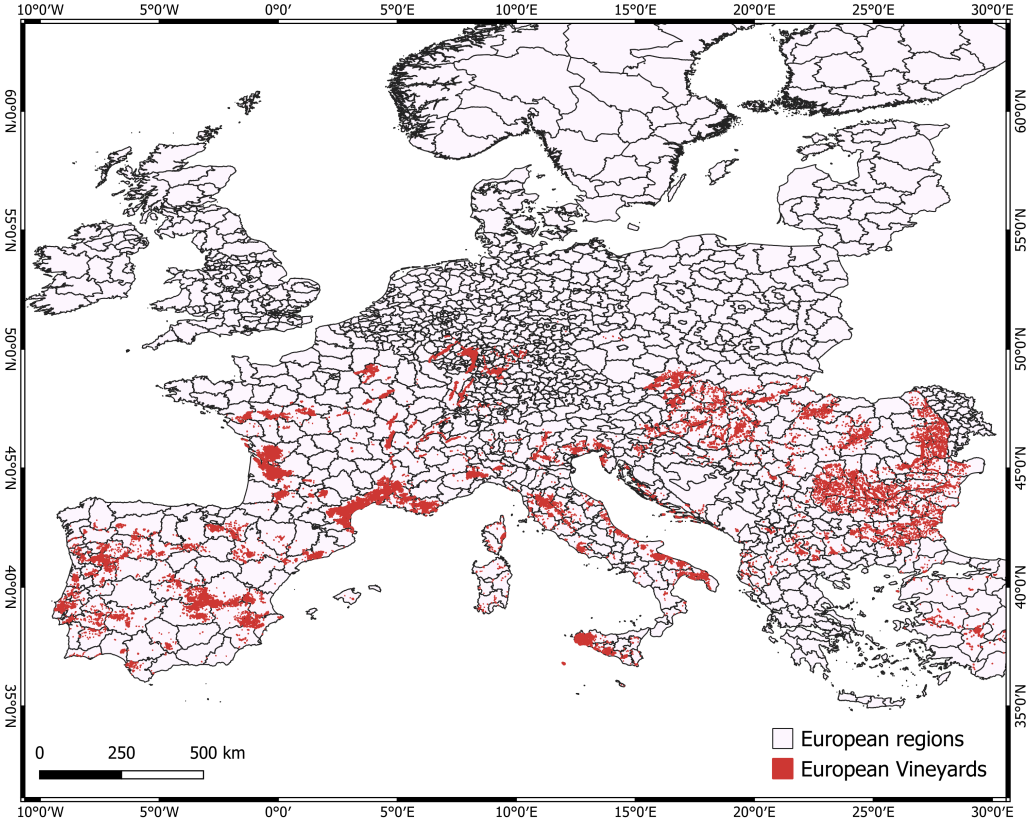

Figure 4.17.: European vineyards.

To illustrate the spatial distribution of hail days specifically for wine-producing countries, both OT detections and HAILCAST output were analyzed. The hail data was first converted into a common hail-day metric and mapped onto a 10 × 10 km grid. For each grid cell, a seasonal mean hail-day frequency was calculated for April–September from 2011 to 2021, representing the average number of hail days per year. These gridded values were then aggregated to the administrative province level in QGIS, using zonal statistics to calculate the spatial mean within each region. The resulting maps therefore depict the spatially averaged annual hail-day occurrence at the provincial scale, allowing for a direct comparison of spatial patterns between the HAILCAST and OTs data.

The spatial distribution derived from OTs and HAILCAST exhibits a high degree of spatial consistency across all four countries. In both datasets, enhanced hail activity is concentrated along major orographic features and known convective hotspots. In Italy (Figure 4.18a), the highest frequencies are observed along the southern Alpine region and extend into the Po Valley, indicating a pronounced maximum in northern Italy. In Spain (Figure 4.18b), hail-day values peak along the Pyrenees and in the northeastern part of the country, with a gradual decrease toward the southern and western regions. A similar orographic influence is

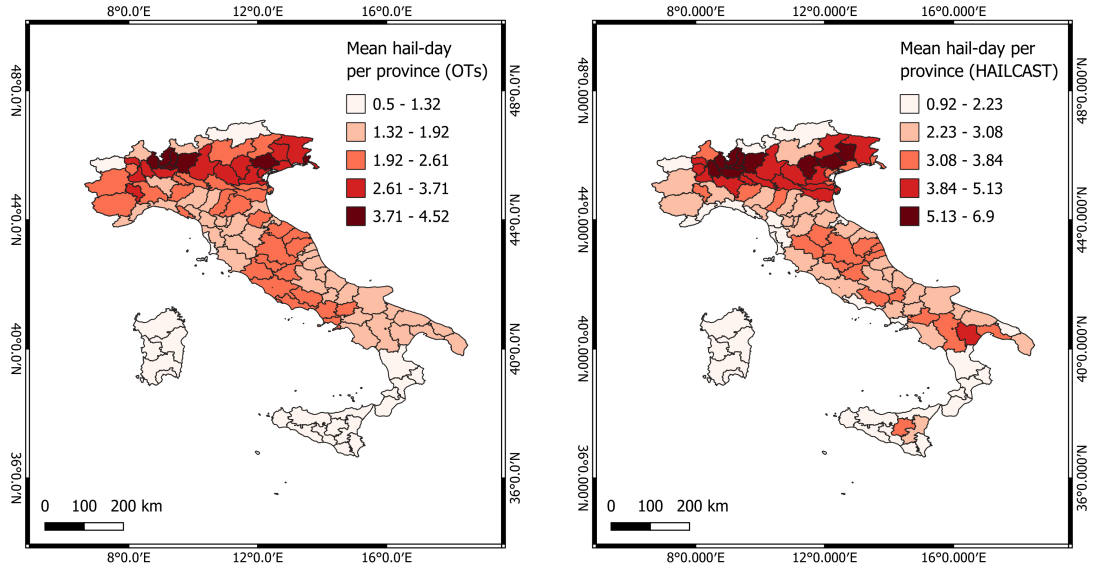

(a) Italy

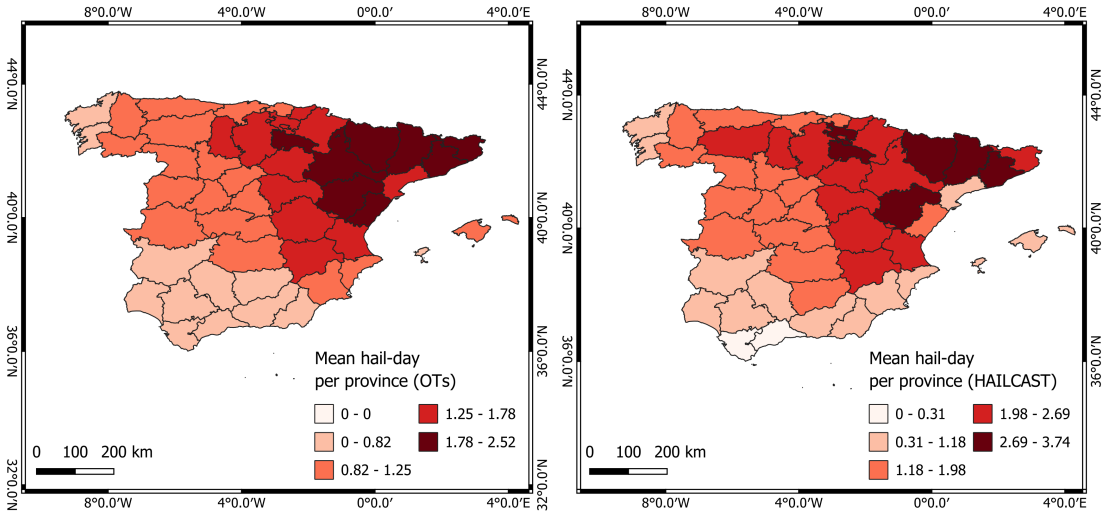

(b) Spain

Figure 4.18.: Regional average hail-day distribution per administrative region of Italy (a) and Spain (b) derived from OTs (left) and HAILCAST (right) during April–September of 2011–2021. The original hail-day fields were calculated on a 10 km × 10 km grid and then spatially aggregated to administrative regions.

evident in France (Figure 4.19a), where increased hail-day occurrence is concentrated along the Pyrenees, the Massif Central, and parts of southern and eastern France. In Germany (Figure 4.19b), the highest values are found in the southern regions, particularly along the northern Alpine foreland and in parts of Baden-Württemberg and Bavaria, whereas lower values dominate northern Germany.

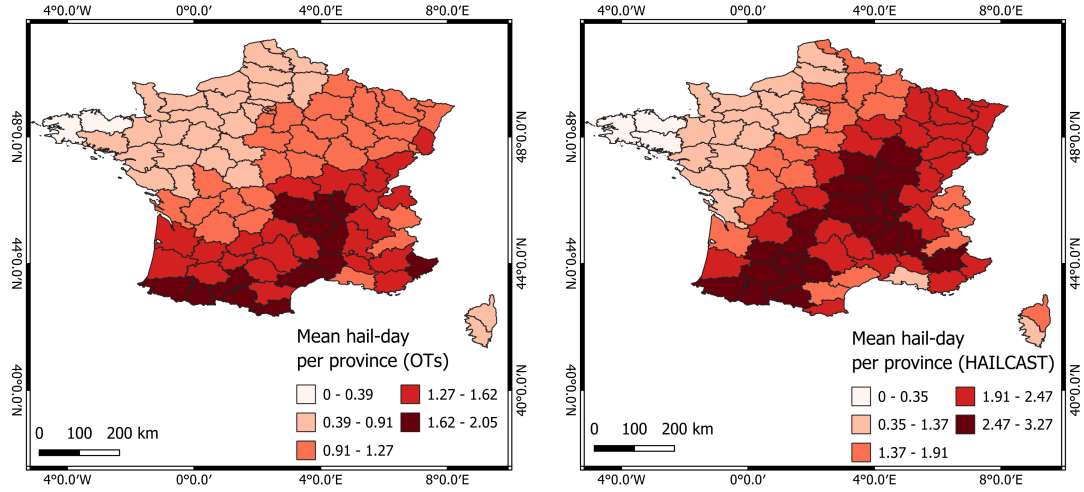

(a) France

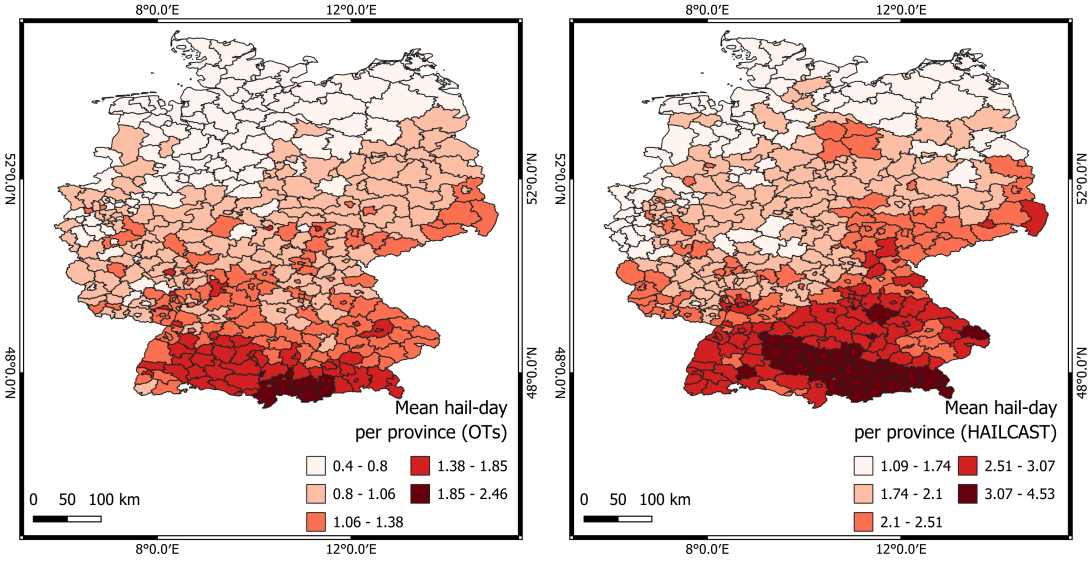

(b) Germany

Figure 4.19.: Regional average hail-day distribution per administrative region of France (a) and Germany (b) derived from OTs (left) and HAILCAST (right) during April–September of 2011–2021. The original hail-day fields were calculated on a 10 km × 10 km grid and then spatially aggregated to administrative regions.

These spatial patterns are consistent with previously identified national or European hail hotspots, which are typically associated with mountainous terrain and regions favorable for deep moist convection (Punge and Kunz, 2016; Cui et al., 2025). Lower hail-day frequencies in coastal and southern regions, such as southern Italy and southern Spain, further reflect less favorable convective environments in these areas. Nevertheless, some regional differences between HAILCAST and OTs are evident. In Germany, both datasets indicate enhanced hail activity toward the south, but the spatial distribution of the maxima differs. HAILCAST shows a stronger signal in southern Germany and therefore appears to represent the main

hail-prone area more clearly than OTs. However, the exact hotspot locations still differ from radar-based analyses, which identify pronounced maxima south of Stuttgart, downstream of the Black Forest, over the Swabian Jura, and in the Bavarian Prealps (Mohr et al., 2026).

Despite the overall agreement in the spatial distribution, notable differences remain in the magnitude of hail-day occurrence. Compared with OT-based results, HAILCAST systematically produces higher values, which can be attributed to differences in the underlying detection principles between simulated hail and satellite-derived hail proxy.

Overall, the strong correspondence in spatial patterns suggests that both HAILCAST and OTs reliably capture the large-scale distribution of hail-prone environments, despite the remaining systematic differences in the magnitudes of seasonal hail-day occurrence.

4.6. Case Studies

To assess the practical performance of the hail proxies at the local scale, a case-study analysis was conducted. For this purpose, this research focuses on the main wine-producing countries.

Several major hail events from the 2011–2021 period were selected to provide a representative set of case studies. Event selection was based on two criteria: the severity of viticultural damage, quantified by the affected area (ha), and the associated reduction in production levels, reflected in substantial losses in total crop yield.

The analysis is based on a comparative spatial evaluation of how well hail proxies reproduce documented ground-level damage patterns. For each case, the geographic overlap between reported vineyard damage and the spatial patterns from three data sources – HAILCAST, OTs, and ESWD reports – were examined. A comparative assessment of these spatial plots illustrates the degree to which each proxy aligns with documented damage. This comparison provides insight into the practical usefulness of HAILCAST and OT data while also highlighting discrepancies in their spatial representation of hail impacts.

Following the statistical evaluation, we can gain a clearer understanding by examining selected case studies for specific days. This approach enables analysis of the spatial structure of specific hail events and provides additional insights into how HAILCAST, OTs, and ESWD represent these occurrences in practice. In this subsection, three case studies from different European regions are presented to illustrate both strong and weak levels of agreement between the datasets.

The figures (Figure 4.20–Figure 4.22) illustrate contrasting examples of proxy agreement. The left-hand panels show cases with strong spatial consistency between HAILCAST, OTs, and ESWD observations. In contrast, the right-hand panels highlight events with reduced agreement, where reported hail occurrences from ESWD and affected wineries are not consistently detected by HAILCAST and OTs.

In Italy, two significant hail events that greatly impacted viticultural areas occurred on 20 July 2012, and 28 June 2021 (Figure 4.20). The hailstorm of 20 July 2012 hit the Vallagarina region in Trentino, including the communes of Nomi, Villalagarina, Calliano, Besenello, and Volano. According to Provincia autonoma di Trento (2012), vineyard damage reached up to 100% in the most severely affected areas. A second severe event occurred on 28 June 2021 in the Oltrepò Paveseregion of Lombardy. Reports described extensive vineyard damage, including smashed berries and destroyed grape bunches, with up to 80% of cultivation affected in some areas. The communes most strongly impacted included Montù Beccaria, Bosnasco, and Zenevredo (ANSA, 2021). ERA5-derived environmental parameters extracted at the OT locations indicate that both events occurred in conditions supportive of deep convection. In the selected affected area, the 20 July 2012 event showed MUCAPE up to 1472 J kg^{-1} and bulk shear up to 26.0 m $^{-1}$, while the single OT point detected on 28 June 2021 had MUCAPE of 1669 J kg^{-1} and bulk shear of 16.9 m s^{-1}. These values indicate instability and sufficient vertical wind shear for organized convection, but do not directly confirm hail at the ground.

Looking at Figure 4.20, the left plot shows a strong spatial agreement between the reported vineyard damage (yellow rhombus), OT detections (red circle), HAILCAST hail swath, and ESWD hail reports (green triangle). All datasets demonstrate consistent hail occurrence in northern Italy, indicating that the event was accurately captured by satellite and model-based methods, as well as ground-based observations. While the spatial overlap may not be exact, all datasets indicate hail activity near the reported vineyard damage.

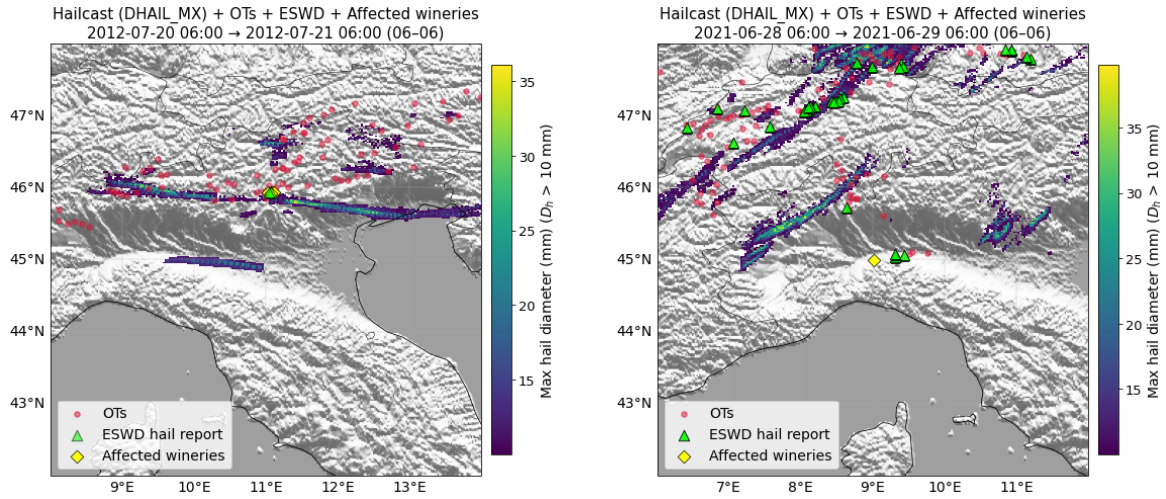

Figure 4.20.: Spatial distribution and co-occurrence of HAILCAST, OTs, ESWD hail reports, and affected wineries for Italy.

In contrast, the right plot illustrates a case with weaker spatial consistency between the datasets. OTs and ESWD reports indicate convective activity and hail in the vineyard area. However, HAILCAST does not directly capture hail occurrence at the damage location, instead placing the strongest hail signal further to the north and east. Nevertheless, the model output remains partially consistent with the OT detections and ESWD reports in the surrounding region.

On the 1 of June 2021, Spain was hit by a major hailstorm that, according to the reports (Heraldo de Aragón, 2021), struck the D.O. Cariñena wine region in Aragón. The event caused substantial damage to approximately 500 hectares of vineyard, concentrated around the towns of Paniza and Cariñena. Another severe hailstorm occurred on 20 August 2018, affecting the Sierra de Montilla wine region of Andalusia. Local estimates indicated that approximately 500,000 kg of grapes were affected (RAIF Andalucía, 2018).

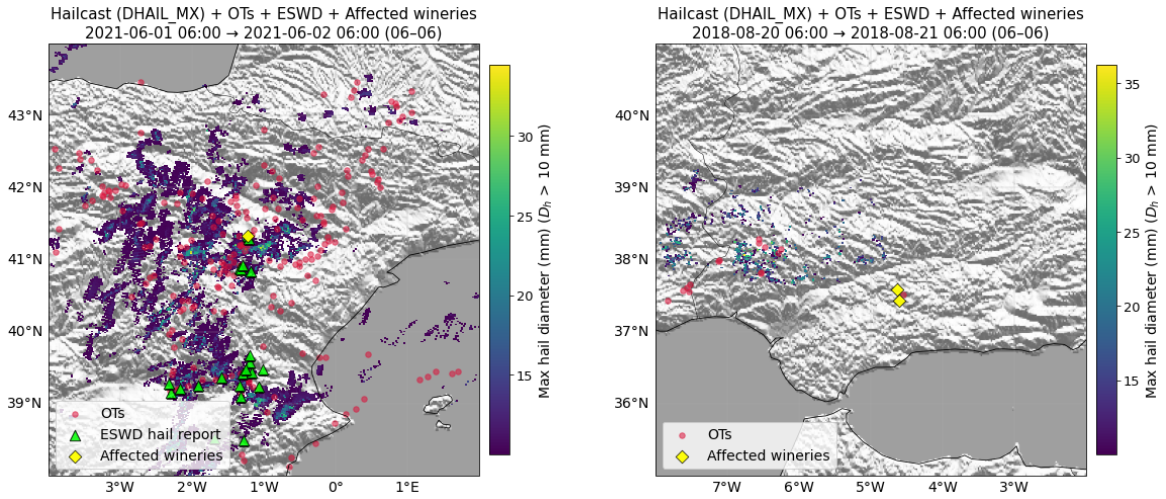

Figure 4.21.: Spatial distribution and co-occurrence of HAILCAST, OTs, ESWD hail reports, and affected wineries for Spain.

In the Figure 4.21, a similar contrast between strong and weak agreement between the datasets can be observed. The left panel presents a case in which the reported vineyard damage is represented by all datasets used in this work. While the right panel illustrates a case with much weaker agreement. Although OT detections are present in the vicinity of the affected wineries, neither HAILCAST nor ESWD reports indicate significant hail occurrence directly over the reported area. One possible explanation is that the event produced hailstones smaller than 2 cm, which would not be included in the ESWD reports. Another possibility is that the precipitation was graupel, which was not detected by either ESWD or HAILCAST. This interpretation is further supported by the ERA5-derived environmental parameters extracted at the OT locations. In the selected area on 20 August 2018, both MUCAPE and bulk shear were relatively low, with MUCAPE reaching only 972 J kg^{-1} and bulk shear only 1.2 m s^{-1}. This suggests that the environment was not very favorable for organized hail-producing convection on this day, and may indicate uncertainty in the reported timing from the vineyard rather than a failure of HAILCAST to detect a severe hail signal.

To further investigate cases with weaker agreement between the datasets, the German case studies were additionally checked against radar observations. As vineyard damage reports may contain spatial and temporal uncertainties, particularly when damage is reported some time after the event, radar observations provide an additional reference to verify the presence of hail activity on the reported day. The radar dataset consists of tracked potential

hail-bearing cells derived from 3D radar reflectivity data using the TRACE3D tracking algorithm, which identifies and follows convective cells with hail potential based on radar reflectivity cores (Mohr et al., 2026). The dataset provides information on hail-track location, propagation, duration, direction, and track geometry at 15-minute intervals.

The first hailstorm occurred on 26 August 2011 in the Mittelmosel region, where severe hail damage was reported for the wine-growing areas around Veldenz and Brauneberg. The second event occurred on 29 June 2021 in the Pfalz region near Bad Dürkheim/Gönnheim, where hail damage was documented for vineyards of Bioweingut Eymann, including damage to grapes and vine wood (Köhler, 2021). On 26 August 2011, warm and humid conditions prevailed in the affected region, with Bernkastel-Kues reaching 30 °C, 76% mean humidity, and 24.8 mm of precipitation. The 500 hPa field shows an upper-level trough over western to central Europe (Wetterzentrale, 2026). Together with MUCAPE of up to 3075 J kg^{-1} and bulk shear reaching 28.8 m s^{-1}, this indicates a favorable environment for organized severe convection and hail. On 29 June 2021, the extracted parameters also indicate that the atmosphere was unstable and sufficiently sheared, with MUCAPE of up to 2261 J kg^{-1} and bulk shear of up to 22.7 m s^{-1}.

As shown on the right panel in Figure 4.22, radar-derived hail tracks are present in the vicinity of the affected wineries and ESWD reports, confirming that there was hail on this specific day. However, no clear HAILCAST hail signal is visible over the affected region on this day, while only a weak signal is detected further south of the reported damage location. This suggests that the modeled convective conditions were insufficient to trigger sustained strong updrafts required for HAILCAST activation.

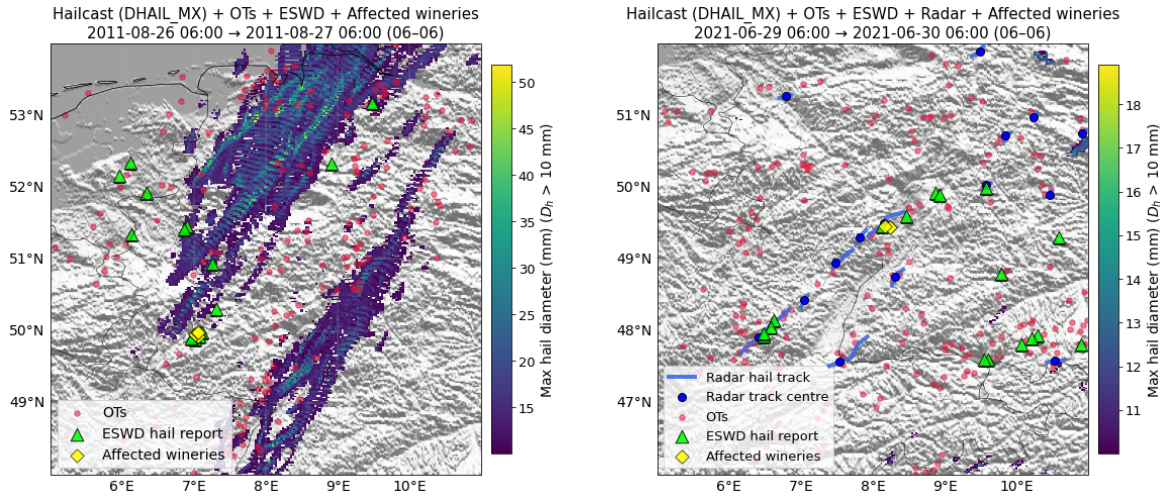

Figure 4.22.: Spatial distribution and co-occurrence of HAILCAST, OTs, ESWD hail reports, and affected wineries for Germany. With the addition of radar based hail tracks on the right plot.

Overall, the analyzed case studies demonstrate that although substantial agreement is often observed among HAILCAST, OT detections, and ESWD hail reports, important differences remain at local scales. In some cases, hail occurrence is consistently represented across all datasets, while in others, one or more datasets fail to capture the reported event. For

example, OT detections may indicate strong convective activity without corresponding HAILCAST or ESWD signals, whereas in other situations, hail reports or modeled hail swaths are present without clear OT detections. These results highlight that each dataset captures different aspects of hail-producing convection and that no single dataset is sufficient to fully represent hail occurrence over affected regions. Therefore, the combined use of HAILCAST, OTs, and ESWD provides a more comprehensive representation of hail events and their spatial variability.

4.7. Persistent hail occurrence and its relevance for viticulture

The case studies presented in section 4.6 provided examples of hail-related damage to wine-growing regions, highlighting that individual events may not always be fully captured by the available datasets. Even a single severe hail event can cause substantial damage to vineyards, particularly when it occurs during a sensitive stage of vine development. However, it is also important to recognize the broader relevance of repeated or persistent hail occurrence during the growing season, as multiple hail days may further increase the potential for damage to grapevines. As the impact of hail strongly depends on the vine's developmental stage, events that occur during sensitive periods may lead to particularly severe consequences for vine growth, final yield, and grape quality. Therefore, the following section shifts the focus from individual hail events to periods of persistent hail occurrence and discusses their relevance for viticulture. These periods are defined here as at least ten consecutive hail days.

Periods of persistent hail occurrence were identified based on the central 100 km $\times$ 100 km grid cell and the four directly adjacent grid cells. As shown in Table 4.3, the number of sequences with at least 10 consecutive hail days is considerably larger in HAILCAST than in OTs. In HAILCAST, these periods occur most frequently in June (846), followed by July (813), May (723), and August (696), while April and September show considerably fewer cases. The OT dataset exhibits a similar seasonal pattern, with a maximum in June as well. However, the second-highest number of cases occurs in May, followed by July, whereas August, September, and April have only a few entries. Overall, both datasets indicate that persistent hail activity is concentrated mainly between May and July.

Based on the coordinates of the analyzed European area, many of the persistent hail periods identified in HAILCAST are located over northern Italy, southern Germany, southeastern France, and northern to northeastern Spain. These regions are particularly relevant because they already experience substantial hail-related damage, and climate change may lead to a further increase in hailstorm frequency. These regions are also significant in viticulture as Italy, France, and Spain are the three largest wine-producing countries, with Germany also recognized as a major wine producer (International Organisation of Vine and Wine, 2025). Several of the affected areas lie within or close to European wine-growing regions, such as La Rioja in Spain and Rhine-Main-Nahe in Germany (Irimia et al., 2024; Zhou and Vilar-Zanón, 2024). In the OT datasets, the number of persistent hail periods is lower, and the spatial distribution is less continuous, but several cases are still found in these areas.

Table 4.3.: Number of periods with at least ten consecutive hail days in HAILCAST and OT datasets during 2011–2021, grouped by month. Consecutive hail periods were identified using the central 100 × 100 km grid cell and its four directly adjacent cells. The month refers to the start month of each period.

Month	HAILCAST	OTs
April	43	5
May	723	155
June	846	185
July	813	64
August	696	16
September	110	17

Clear examples of overlaps between HAILCAST and OTs are observed in central Italy from 9 to 20 June, 2014 (Figure 4.23), and in northern to northeastern Spain from 8 to 23 July 2013. Additionally, overlaps are found in southeastern France in June 2015, in southern Germany and the Western Balkans from late May to early June 2018, and in the Bulgaria/Romania region in July 2017.

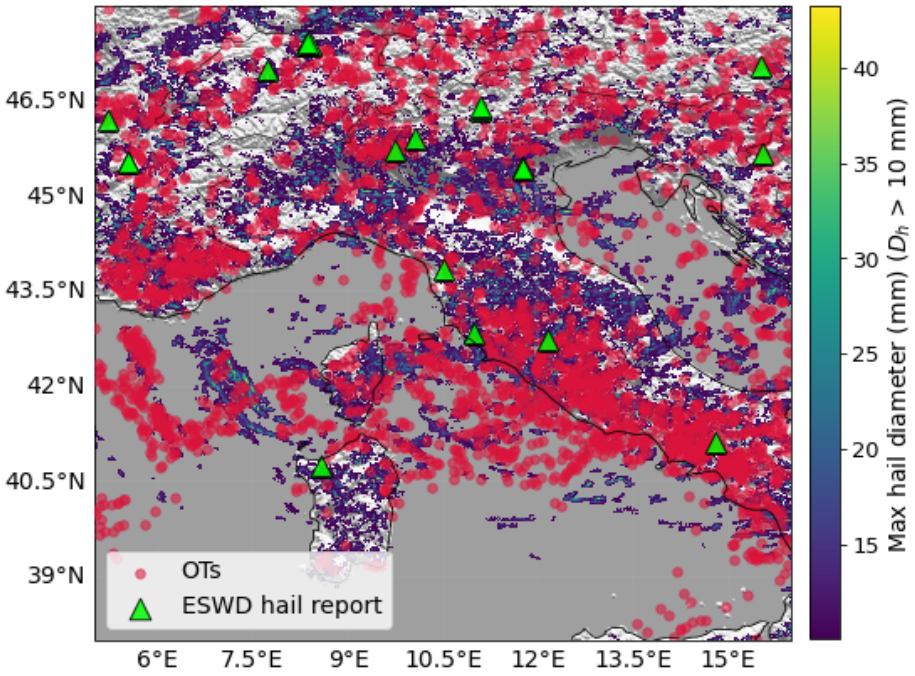

Figure 4.23.: Example of overlapping HAILCAST and OT signals over central Italy during a period of persistent hail activity from 9 to 20 June 2014.

The concentration of persistent hail periods in May, June, July, and August is important for wine grapes as these months coincide with key stages of the grapevine growth cycle, including flowering, setting, berry development, and veraison (Coombe, 1995). Hail during these stages can affect bunches, leaf area, fruit set, berry development, and fruit quality,

with potential consequences for both the current and following season (The Australian Wine Research Institute, 2021).

In European vineyards, these months generally align with the main reproductive and fruit-development phases of the vine. Although the exact timing varies across regions, varieties, and years, flowering and fruit set typically occur in May and June. In contrast, July and August are linked to berry development and the onset of veraison, corresponding to the development stages from flowering and setting to berry growth, softening, color change, and eventual ripening (Coombe, 1995; Korta Katarina Winery, 2026).

During May and June, hail can affect both the canopy and the developing crop. At this stage, hailstones can injure shoots and leaves, and they may also directly affect inflorescences and young bunches, which later determine the overall yield (The Australian Wine Research Institute, 2021). The consequences, therefore, depend not only on the physical removal of leaves and bunches, but also on the amount of functional leaf area that remains at fruit set. The reduction of leaf area can limit successful fruit set, while damage during fruit set can lead to berry abortion and reduce the number of berries per bunch (The Australian Wine Research Institute, 2021). If the main shoot tip is damaged, the vine may respond by producing lateral shoots from the bud in the leaf axils. This can partially compensate for the loss of canopy, but strong lateral development in the fruit zone may increase shading of the remaining crop and developing compound buds. As a result, hail can negatively impact fruit quality in the current season and lower bud fruitfulness for the following year (The Australian Wine Research Institute, 2021). In some cases, lateral shoots may produce a secondary crop that ripens later than the main crop, leading to uneven fruit maturity and difficulty managing the harvest.

As the season progresses, especially during berry development and the early stages of ripening, the significance of hail damage becomes more related to fruit quality, disease risk, and harvest management. Hail wounds the surface of berries and leaves, making these tissues more vulnerable to fungal diseases, especially Botrytis under wet or humid conditions (The Australian Wine Research Institute, 2021). At this stage, direct berry injury becomes particularly important: hail has been observed to cause cracking and visible fruit damage, which can reduce the proportion of marketable or usable berries within a bunch and affect fruit composition at harvest (Petoumenou et al., 2019). If damaged or delayed secondary fruit remains on the vine, selective harvesting or sorting may be required to avoid mixing ripe and unripe fruit, which can negatively affect the quality of the harvested crop (The Australian Wine Research Institute, 2021).

As hail causes substantial damage to the final yield, it is also an important factor for agricultural risk management and insurance. For winegrowers, understanding the timing and location of hail occurrence is crucial for making decisions about insurance coverage and implementing protective measures, such as hail nets. Similarly, for insurance companies, knowing the spatial distribution of hail-prone areas is crucial for assessing regional risk. However, such risk assessment relies heavily on the availability of transparent and comparable agricultural loss data, since insurance applications require not only information on where hail occurs, but also how this translates into crop-specific yield and economic losses.

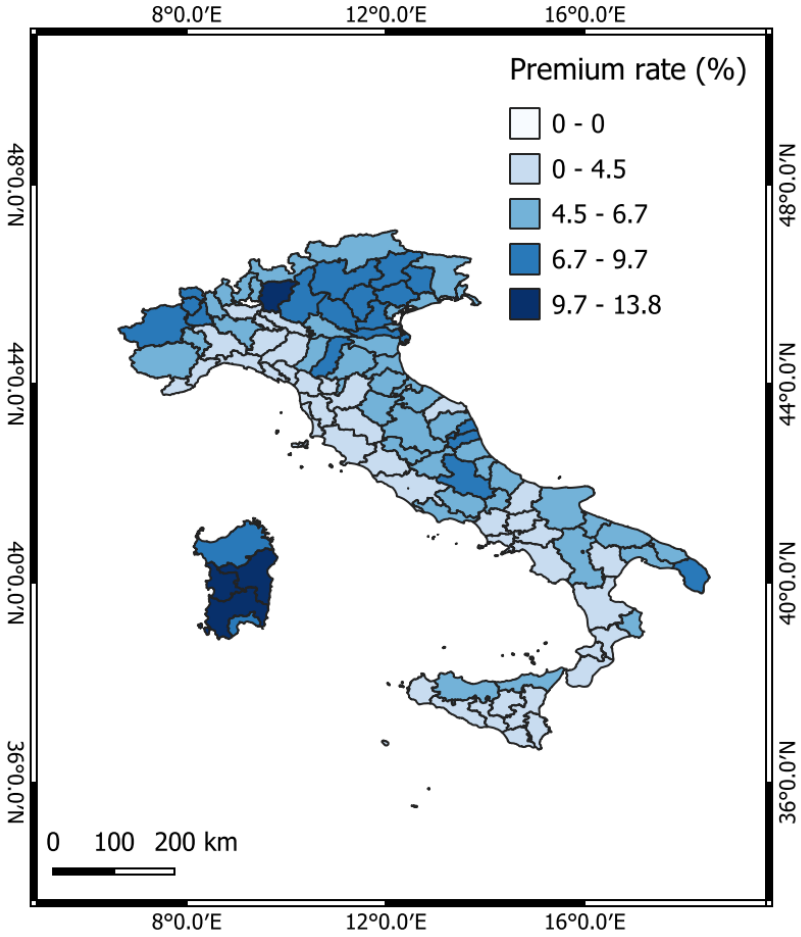

Figure 4.24.: Mean annual insurance premium rate (%) for grapevine-related insurance in Italy.

As an example, Figure 4.24 shows the mean annual insurance premium rate for grapevine-related insurance in Italy. The rate was determined by dividing the total premium by the total insured value over the 11-year period and expressing the result as a percentage. Because the insurance data do not distinguish hail-related losses from other weather-related hazards, this map cannot be interpreted as a direct representation of hail damage. Nevertheless, relatively high premium rates persist in parts of northern Italy, a region known for high hail exposure. This spatial relationship indicates that hail may contribute to the overall insurance risk in these areas, although the specific extent of this contribution cannot be quantified with the available data. Together, these findings highlight the importance of analyzing hail occurrence in both space and time when evaluating its potential impact on European viticulture. At the same time, the limitations of the available insurance information show the need for further studies. More detailed and consistently defined agricultural loss data, ideally separated by crop type, hazard, and economic impact, would allow the contribution of hail to viticultural insurance risk to be assessed more directly. This is consistent with González Peláez et al. (2025), who emphasize that agricultural risk modeling requires improved crop, climate, yield, insurance, and loss data, and that future yield-loss data by crop and peril would help refine model assumptions.

5. Conclusions and outlook

Hail is difficult to observe, model, and evaluate because it is a highly localized and short-lived hazard (Punge and Kunz, 2016; Cui et al., 2025). There is no universal method or dataset that fully represents hail occurrence across Europe. Ground-based reports are affected by population density and reporting practices, while radar-based hail information remains limited due to non-uniform coverage across national networks and topographical gaps (Punge et al., 2017; Taszarek et al., 2020a). This thesis evaluated the consistency of three hail indicators—satellite-based OTs, simulated maximum hail diameter from HAILCAST coupled to a convection-permitting regional climate model, and quality-controlled ESWD hail reports—in representing hail occurrences across Europe. The emphasis is on whether there is agreement between the datasets at broad spatial and temporal scales, or if it consistently persists at the local grid-cell and event scale that are significant for viticulture.

The first part of the analysis showed that all three datasets indicate the main European regions of enhanced hail activity, with hail-day maxima over northern Italy, including the Po Valley and adjacent wine-growing regions, as well as elevated frequencies near the Alpine and pre-Alpine regions, the Pyrenees and the Ebro Valley, and parts of the Balkan Peninsula. This overall distribution aligns with prior studies highlighting southern and central Europe, particularly regions affected by complex terrain and strong convective activity, as important hail-prone areas (Punge and Kunz, 2016). However, the absolute number of hail days differs substantially between the datasets. ESWD exhibits the lowest frequencies, which is consistent with its point-based and report-dependent nature. OTs show higher hail-day frequencies, though they remain more spatially concentrated. In contrast, HAILCAST produces a broader spatial distribution and generally higher hail-day numbers in hail-prone regions. This suggests that while the datasets may share similar large-scale spatial patterns, they are not directly interchangeable.

The interannual analysis did not indicate a clear increase in hail-day frequency in either HAILCAST or OTs from 2011 to 2021, though this period is too short for a robust trend assessment. In contrast, reports from the ESWD show an increase over time, likely influenced by changes in reporting density and practices rather than by a solely meteorological trend (Dotzek et al., 2009). The year 2018 exhibits enhanced hail activity in both HAILCAST and OTs, consistent with several major European hailstorms reported by ESSL during that season (Pucik, 2018). The seasonal and diurnal analyses further revealed that all three datasets capture the expected increase in hail activity during the warm season, when convective activity is strongest, followed by a decrease afterward. This trend is consistent with previous climatological studies of severe convection in Europe (Taszarek et al., 2020a). Similarly, the diurnal cycle peaks in the afternoon, aligning with daytime heating, boundary-layer destabilization, and the development of deep convection (Punge and Kunz, 2016).

While the datasets exhibit comparable large-scale spatial and temporal patterns, categorical verification reveals that their direct agreement at the grid-cell and daily levels is weak. Even at the coarser 100 km × 100 km resolution, the agreement between HAILCAST and OTs remains limited, with low HSS and CSI values indicating little skill beyond chance agreement. At a resolution of 10 km × 10 km, the agreement further decreases, while false alarm ratios increase and skill scores approach zero. This indicates that the similarity between HAILCAST and OTs primarily reflects broad regional and seasonal patterns of hail occurrence, rather than consistently identifying the same hail days within the same grid cells. A similar conclusion follows from the comparison with ESWD reports. The agreement between ESWD and OTs is generally stronger than that between ESWD and HAILCAST, but it still remains limited at the local scale. Overall, the verification results show that the consistency between the datasets is primarily observed at broader spatial and temporal scales, while the agreement at the grid-cell and daily levels remains weak. One reason for this limited agreement is that the datasets represent different aspects of hail occurrence.

The case studies on hail events impacting wineries confirmed the limitations noted by the categorical verification. In some instances, HAILCAST, OTs, ESWD reports, and documented vineyard damage were spatially consistent, demonstrating that the combined datasets can successfully identify areas affected by severe hail. However, in other cases, the agreement was significantly weaker. For example, OT detections and ESWD reports were sometimes located close to damaged vineyards, while HAILCAST either missed the local hail signal or placed the strongest hail occurrence in a different location. The German case studies, which additionally considered radar-based hail tracks, further illustrate that local hail events can be missed or displaced by HAILCAST, even when independent observations indicate hail activity. These results highlight the need for caution when assessing hail at a local scale, particularly when relying on a single data source. For viticulture, this limitation is particularly important. Vineyards are spatially fixed and can be severely affected even by a single hail event, while repeated hail days during sensitive phenological stages may further increase the risk of damage.

By integrating satellite-based OTs, model-based HAILCAST output, and ESWD reports, this thesis provides a cross-scale assessment of European hail occurrence, ranging from broad climatological patterns to localized events that are significant to viticulture. The results indicate that both OTs and HAILCAST are effective in identifying large hail-prone areas and seasonal hail activity; however, their direct correlation at the daily grid-cell level is weak. OTs detections appear more closely co-located with reported severe hail events than HAILCAST in several instances, but they still serve as an indirect proxy for intense convection. HAILCAST provides hail-size information and offers complete spatial coverage, but in this analysis, it often produces broader hail signals and can miss or displace individual local events. Consequently, the datasets are most useful when interpreted together rather than separately.

Several limitations remain. First, the three datasets differ fundamentally in what they represent: ESWD reports observed hail at specific locations, OTs indicate intense convective updrafts, and HAILCAST uses atmospheric profiles from the driving regional climate model to estimate hailstone growth and maximum hail diameter at the ground. Direct categorical

verification, therefore, compares related, but not identical, quantities. Second, the results are sensitive to spatial and temporal aggregation. Higher resolution offers more local detail, but also reduces the probability that two datasets identify hail occurrence in exactly the same grid cell and on the same day. Third, ESWD reports are affected by reporting biases, especially in sparsely populated regions or areas with lower observer activity. Finally, the winery case studies are useful for evaluating local event representation, but they remain selected examples and cannot provide a complete statistical assessment of hail impacts on viticulture. Future studies would benefit from linking hail indicators more directly to vineyard-level damage records, yield losses, and economic loss data. This would allow evaluation not only of hail detection but also of the extent of its impact on viticultural production and insurance-related losses.

Future work should therefore focus on combining several complementary hail datasets. A systematic integration of radar-based hail tracks would be valuable, as radar provides greater spatial and temporal detail than ESWD reports and can more directly verify local hail occurrence. However, radar-based hail climatologies remain difficult to construct consistently across Europe because national radar networks differ in coverage, data availability, and processing methods. Incorporating additional observational sources such as hailpads, agricultural damage reports, and insurance loss data could enhance the evaluation, especially for viticulture.

Future methodological improvements could include a more systematic testing of spatial buffers and temporal matching windows around ESWD reports and winery damage locations. This would help account for small spatial displacements between datasets and possible uncertainty in the timing and location of reported hail or winery damage. For HAILCAST, future sensitivity tests should examine how strongly the results depend on the model activation criterion, particularly the representation of updrafts in the driving model. In the COSMO implementation used here, HAILCAST is activated when the modeled updraft speed exceeds 10 m s^{-1} for at least 15 minutes. If this threshold is too permissive, the model may generate hail signals in convective situations where hail does not necessarily reach the ground. Testing higher updraft-speed thresholds or less sensitive activation criteria could help determine whether the broad spatial hail occurrence observed in HAILCAST is partly due to overly frequent model activation. For OTs, future work could further examine the relationship between OT probability, environmental conditions, and reported hail size, especially for severe hail thresholds. Finally, applying the same framework to a longer study period and to additional wine-growing regions would help assess whether the conclusions reached here are valid across other European areas.

Overall, this thesis demonstrates that OTs, HAILCAST, and ESWD provide complementary information on hail occurrence in Europe. They agree reasonably well in identifying the main hail-prone regions and their general seasonal and diurnal behavior of hail activity. However, their agreement is limited to the local event scale that is most relevant to vineyards and other exposed agricultural systems. Therefore, hail assessment for European viticulture should not rely on a single hail indicator. Instead, the most robust interpretation is obtained by combining satellite-based indicators of intense convection,model-based

HAILCAST estimates of maximum hail diameter at the ground, and available ground-based observations.

Bibliography

Adler, R. F. and Mack, R. A. (1986). Thunderstorm cloud top dynamics as inferred from satellite observations and a cloud top parcel model. *Journal of Atmospheric Sciences*, 43(18):1945 – 1960.

Allianz Commercial (2026). Severe convective storms: Trends, impacts, and pathways to resilience. Global Risk Dialogue Commercial Insights, Allianz Global Corporate & Specialty SE, Munich, Germany. Published March 2026.

ANSA (2021). Maltempo: grandine in oltrepò pavese, danni ai vigneti. Accessed: 2026-05-09.

Baldauf, M., Seifert, A., Förstner, J., Majewski, D., Raschendorfer, M., and Reinhardt, T. (2011). Operational convective-scale numerical weather prediction with the cosmo model: Description and sensitivities. *Monthly Weather Review*, 139(12):3887 – 3905.

Barry, R. G. and Chorley, R. J. (2003). *Atmosphere, Weather and Climate*. Routledge, London, 8 edition.

Battaglioli, F., Taszarek, M., Groenemeijer, P., Púčik, T., and Rädler, A. (2026). Contrasting trends in very large hail events and related economic losses across the globe. *Nature Geoscience*, 19(1):52–58.

Bedka, K. M. (2011). Overshooting cloud top detections using msg seviri infrared brightness temperatures and their relationship to severe weather over europe. *Atmospheric Research*, 99(2):175–189.

Bedka, K. M. and Khlopenkov, K. (2016). A probabilistic multispectral pattern recognition method for detection of overshooting cloud tops using passive satellite imager observations. *Journal of Applied Meteorology and Climatology*, 55(9):1983 – 2005.

Berthet, C., Dessens, J., and Sanchez, J. (2011). Regional and yearly variations of hail frequency and intensity in france. *Atmospheric Research*, 100(4):391–400. 5th European Conference on Severe Storms.

Bolton, D. (1980). The computation of equivalent potential temperature. *Monthly Weather Review*, 108(7):1046 – 1053.

Byers, H. R. and Braham, R. R. (1949). *The Thunderstorm: Report of the Thunderstorm Project*. U.S. Weather Bureau, Department of Commerce, Washington, DC.

Carmona, M. J., Chaïb, J., Martínez-Zapater, J. M., and Thomas, M. R. (2008). A molecular genetic perspective of reproductive development in grapevine. *Journal of Experimental Botany*, 59:2579–2596.

Chen, S. S. and Frank, W. M. (1993). A numerical study of the genesis of extratropical convective mesovortices. part i: Evolution and dynamics. *Journal of the Atmospheric Sciences; (United States)*, 50:15.

Coombe, B. (1995). Growth stages of the grapevine: Adoption of a system for identifying grapevine growth stages. *Australian Journal of Grape and Wine Research*, 1(2):104–110.

Coombe, B. G. and McCarthy, M. G. (2000). Dynamics of grape berry growth and physiology of ripening. *Australian Journal of Grape and Wine Research*, 6:131–135.

Cui, R., Thurnherr, I., Velasquez, P., Brennan, K. P., Leclair, M., Mazzoleni, A., Schmid, T., Wernli, H., and Schär, C. (2025). A european hail and lightning climatology from an 11-year kilometer-scale regional climate simulation. *Journal of Geophysical Research: Atmospheres*, 130(14):e2024JD042828. e2024JD042828 2024JD042828.

Daniell, J. (2025). Provision of hailcast data, european vineyards dataset, and catdat dataset for the analysis of hail impacts on european viticulture. Personal communication and data provision, 20 August 2025.

Deepen, J. (2006). Schadenmodellierung extremer hagelereignisse in deutschland. Diplomarbeit, Westfälische Wilhelms-Universität Münster.

Doswell, C. A. (1987). The distinction between large-scale and mesoscale contribution to severe convection: A case study example. *Weather and Forecasting*, 2(1):3 – 16.

Dotzek, N., Groenemeijer, P., Feuerstein, B., and Holzer, A. M. (2009). Overview of essl's severe convective storms research using the european severe weather database eswd. *Atmospheric Research*, 93(1):575–586. 4th European Conference on Severe Storms.

Emanuel, K. A. (1995). Atmospheric convection, k. a. emanuel, oxford university press (new york), 1994. no. of pages: x+580. price: $47.50. isbn: 0-19-506630-8. *International Journal of Climatology*, 15(7):821–822.

European Commission (2025). Wine. `https://agriculture.ec.europa.eu/farming/crop-productions-and-plant-based-products/wine_en`. Accessed: 31 May 2026.

European Severe Storms Laboratory (2026). European Severe Weather Database. `https://eswd.eu/en`. Accessed: 2026-05-30.

Feldmann, M., Domeisen, D. I. V., and Martius, O. (2025). A pan-european analysis of large-scale drivers of severe convective outbreaks. *Weather and Climate Dynamics*, 6(4):1089–1106.

Fischer, J., Groenemeijer, P., Holzer, A., Feldmann, M., Schröer, K., Battaglioli, F., Schielicke, L., Púčik, T., Gatzen, C., Antonescu, B., and the TIM Partners (2025). Invited perspectives: Thunderstorm intensification from mountains to plains.

Fischer von zur Gathen, J. (2026). Personal communication on environmental filtering thresholds for overshooting-top detections. Personal communication, 13 October 2025.

Giordani, A., Kunz, M., Bedka, K. M., Punge, H. J., Paccagnella, T., Pavan, V., Cerenzia, I. M. L., and Di Sabatino, S. (2024). Characterizing hail-prone environments using convection-permitting reanalysis and overshooting top detections over south-central europe. *Natural Hazards and Earth System Sciences*, 24(7):2331–2357.

González Peláez, A., Daniell, J., and Douglas, R. (2025). Insurance and risk management tools for agriculture in the eu. Market analysis, fi-compass. Prepared with the support of Howden with Risklayer and Karlsruhe Institute of Technology for the European Commission and European Investment Bank.

Groenemeijer, P., Púčik, T., Holzer, A. M., Antonescu, B., Riemann-Campe, K., Schultz, D. M., Kühne, T., Feuerstein, B., Brooks, H. E., Doswell, C. A., Koppert, H.-J., and Sausen, R. (2017). Severe convective storms in europe: Ten years of research and education at the european severe storms laboratory. 98(12):2641–2651.

Heim, C., Panosetti, D., Schlemmer, L., Leuenberger, D., and Schär, C. (2020). The influence of the resolution of orography on the simulation of orographic moist convection. 148(6):2391–2410.

Heraldo de Aragón (2021). La d.o. cariñena estima daños en un 3,5% de su superficie de viñedo.

Holton, J. R. and Hakim, G. J. (2013). *An Introduction to Dynamic Meteorology*. Elsevier.

Houze, R. A., Biggerstaff, M. I., Rutledge, S. A., and Smull, B. F. (1989). Interpretation of doppler weather radar displays of midlatitude mesoscale convective systems. *Bulletin of the American Meteorological Society*, 70:608–619.

Hulton, F. and Schultz, D. M. (2024). Climatology of large hail in europe: characteristics of the european severe weather database. *Natural Hazards and Earth System Sciences*, 24(4):1079–1098.

International Organisation of Vine and Wine (2025). State of the global vine and wine sector. OIV Press Conference, presented by John Barker, OIV Director General.

Irimia, L. M., Patriche, C. V., Petitjean, T., Tissot, C., Santesteban, L. G., Neethling, E., Foss, C., Le Roux, R., and Quénol, H. (2024). Structural and spatial shifts in the viticulture potential of main european wine regions as an effect of climate change. *Horticulturae*, 10(4).

Juckes, M. and Smith, R. K. (2000). Convective destabilization by upper-level troughs. *Quarterly Journal of the Royal Meteorological Society*, 126:111–123.

Khlopenkov, K. V., Bedka, K. M., Cooney, J. W., and Itterly, K. (2021). Recent advances in detection of overshooting cloud tops from longwave infrared satellite imagery. *Journal of Geophysical Research: Atmospheres*, 126(14):e2020JD034359. e2020JD034359 2020JD034359.

Kirshbaum, D. J., Adler, B., Kalthoff, N., Barthlott, C., and Serafin, S. (2018). Moist orographic convection: Physical mechanisms and links to surface-exchange processes. *Atmosphere*, 9(3).

Köhler, H. (1921). Zur kondensation des wasserdampfes in der atmosphäre. *Geofysisk Publicationer*, 2:3–15.

Korta Katarina Winery (2026). Everything you ever wanted to know about the life cycle of a grape.

Kunz, M. (2007). The skill of convective parameters and indices to predict isolated and severe thunderstorms. *Natural Hazards and Earth System Sciences*, 7(2):327–342.

Köhler, M. (2021). Schwieriges jahr für weinbau.

Lamb, D. and Verlinde, J. (2011). *Physics and Chemistry of Clouds*. Cambridge University Press, Cambridge.

Lemon, L. R. and Doswell, C. A. (1979). Severe thunderstorm evolution and mesocyclone structure as related to tornadogenesis. *Monthly Weather Review*, 107(9):1184 – 1197.

Lin, Y.-L. (2007). *Mesoscale Dynamics*. Cambridge University Press.

Lombardo, K. and Bitting, M. (2024). A climatology of convective precipitation over europe. 152(7):1555–1585.

López, L., García-Ortega, E., and Sánchez, J. L. (2007). A short-term forecast model for hail. *Atmospheric Research*, 83(2):176–184. European Conference on Severe Storms 2004.

Markowski, P. and Richardson, Y. (2010). *Mesoscale Meteorology in Midlatitudes*. Wiley, 1 edition.

MeteoSwiss (n.d.). Hail climatology.

Möhler, O. (2024). Introduction to atmospheric aerosol processes. Lecture slides, Atmospheric Aerosols, Winter term 2023–24, Karlsruhe Institute of Technology.

Mohr, S., Tonn, M., Augenstein, M., Sperka, C., Kavil Kambrath, G., and Kunz, M. (2026). A 20-year spatio-temporal analysis of 3d radar-based hail tracks in germany: trends and regional differences. *Frontiers in Environmental Science*, Volume 14 - 2026.

Munich Re (2026). Hail, tornadoes and flash floods: Risks from severe thunderstorms on the rise. `https://www.munichre.com/en/risks/natural-disasters/thunderstorms-hail-tornados.html`. Updated April 2026; accessed 29 May 2026.

Naidu, R. A., Maree, H. J., and Burger, J. T. (2015). Grapevine leafroll disease and associated viruses: A unique pathosystem. *Annual Review of Phytopathology*, 53:613–634.

NOAA National Weather Service (n.d.). Skew-t parameters and indices. Accessed: 2026-04-22.

OIV (2025). World wine production outlook 2025. Technical report, International Organisation of Vine and Wine, Dijon, France. OIV First Estimates 2025.

Petoumenou, D. G., Biniari, K., Xyrafis, E., Mavronasios, D., Daskalakis, I., and Palliotti, A. (2019). Effects of natural hail on the growth, physiological characteristics, yield, and quality of vitis vinifera l. cv. thompson seedless under mediterranean growing conditions. *Agronomy*, 9(4).

Provincia autonoma di Trento (2012). Grandine in vallagarina: gli aiuti ai viticoltori. Comunicato stampa, accessed 2026-05-09.

Pruppacher, H. R., Klett, J. D., and Wang, P. K. (1998). Microphysics of clouds and precipitation. *Aerosol Science and Technology*, 28(4):381–382.

Pucik, T. (2018). Major hailstorms of 2018 across europe. European Severe Storms Laboratory. Accessed: 2026-05-30.

Punge, H., Bedka, K., Kunz, M., and Reinbold, A. (2017). Hail frequency estimation across europe based on a combination of overshooting top detections and the era-interim reanalysis. *Atmospheric Research*, 198:34–43.

Punge, H. and Kunz, M. (2016). Hail observations and hailstorm characteristics in europe: A review. 176-177:159–184.

Punge, H. J., Bedka, K. M., Kunz, M., Bang, S. D., and Itterly, K. F. (2023). Characteristics of hail hazard in south africa based on satellite detection of convective storms. *Natural Hazards and Earth System Sciences*, 23(4):1549–1576.

Puskeiler, M. (2013). Radarbasierte analyse der hagelgefährdung in deutschland.

Púčik, T., Castellano, C., Groenemeijer, P., Kühne, T., Rädler, A. T., Antonescu, B., and Faust, E. (2019). Large hail incidence and its economic and societal impacts across europe. *Monthly Weather Review*, 147(11):3901 – 3916.

Púčik, T., Groenemeijer, P., Rýva, D., and Kolář, M. (2015). Proximity soundings of severe and nonsevere thunderstorms in central europe. *Monthly Weather Review*, 143(12):4805 – 4821.

RAIF Andalucía (2018). Vid: fuerte tormenta de granizo en la sierra de montilla.

Risklayer GmbH (2024). Winerisk: Hailstorms. WineRisk project page on hailstorm risk for wine regions.

Robert A. Houze, J. (2014). *Cloud Dynamics*, volume 104 of *International Geophysics*. Elsevier Academic Press, 2 edition.

Scarino, B. R., Bedka, K., Bhatt, R., Khlopenkov, K., Doelling, D. R., and Smith Jr., W. L. (2020). A kernel-driven brdf model to inform satellite-derived visible anvil cloud detection. *Atmospheric Measurement Techniques*, 13(10):5491–5511.

Swiss Re (2023). Natural catastrophes in focus: Tornados, hail and thunderstorms. Accessed: 2026-04-18.

Taszarek, M., Allen, J. T., Groenemeijer, P., Edwards, R., Brooks, H. E., Chmielewski, V., and Enno, S.-E. (2020a). Severe convective storms across europe and the united states. part i: Climatology of lightning, large hail, severe wind, and tornadoes. 33(23):10239–10261.

Taszarek, M., Allen, J. T., Púčik, T., Hoogewind, K. A., and Brooks, H. E. (2020b). Severe convective storms across europe and the united states. part ii: Era5 environments associated with lightning, large hail, severe wind, and tornadoes. *Journal of Climate*, 33(23):10263 – 10286.

Taszarek, M., Nixon, C., Pucik, T., Szuster, P., Groenemeijer, P., Battaglioli, F., and Czernecki, B. (2025). Severe storm research with thunder package: Improvements in calculation procedures of convective parameters. In *12th European Conference on Severe Storms*, Utrecht, Netherlands. Conference poster, 17–21 November 2025.

The Australian Wine Research Institute (2021). Managing grapevines after hail damage. Viticulture Fact Sheet, updated November 2021.

Thurnherr, I., Cui, R., Velasquez, P., Wernli, H., and Schär, C. (2025). The effect of 3 °C global warming on hail over europe. *Geophysical Research Letters*, 52(18):e2025GL114811. e2025GL114811 2025GL114811.

Ursu, A., Istrate, V., Jitariu, V., and Lazăr, I.-L. (2025). Hail damage detection: Integrating sentinel-2 images with weather radar hail kinetic energy. *Remote Sensing*, 17(23).

Vallis, G. K. (2017). *Atmospheric and Oceanic Fluid Dynamics: Fundamentals and Large-Scale Circulation*. Cambridge University Press, 2 edition.

Van Baelen, J., Reverdy, M., Tridon, F., Labbouz, L., Dick, G., Bender, M., and Hagen, M. (2011). On the relationship between water vapour field evolution and the life cycle of precipitation systems. *Quarterly Journal of the Royal Meteorological Society*.

van Ederen, D., d.S. Fonseca-Cerda, M., Botzen, W. J., Aerts, J. C., Lupi, V., Scussolini, P., and Gubbels, K. B. (2026). A high-resolution compound vulnerability function for severe convective storm losses. *Climate Services*, 42:100656.

Wallace, J. M. and Hobbs, P. V. (2006). *Atmospheric Science: An Introductory Survey*. Academic Press, Amsterdam, 2 edition.

Wetterzentrale (2026). Reanalysis archives: Cfsr. Accessed: 2026-05-31.

Wilks, D. S. (2006). *Statistical Methods in the Atmospheric Sciences*, volume 91 of *International Geophysics Series*. Academic Press, Amsterdam, 2 edition.

Wissmeier, U. and Goler, R. (2009). A comparison of tropical and midlatitude thunderstorm evolution in response to wind shear. *Journal of the Atmospheric Sciences*, 66(8):2385–2398.

Young, K. C. (1993). *Microphysical Processes in Clouds*. Oxford University Press, New York.

Zhou, N. and Vilar-Zanón, J. L. (2024). Impact assessment of climate change on hailstorm risk in spanish wine grape crop insurance: Insights from linear and quantile regressions. *Risks*, 12(2).

A. Appendix

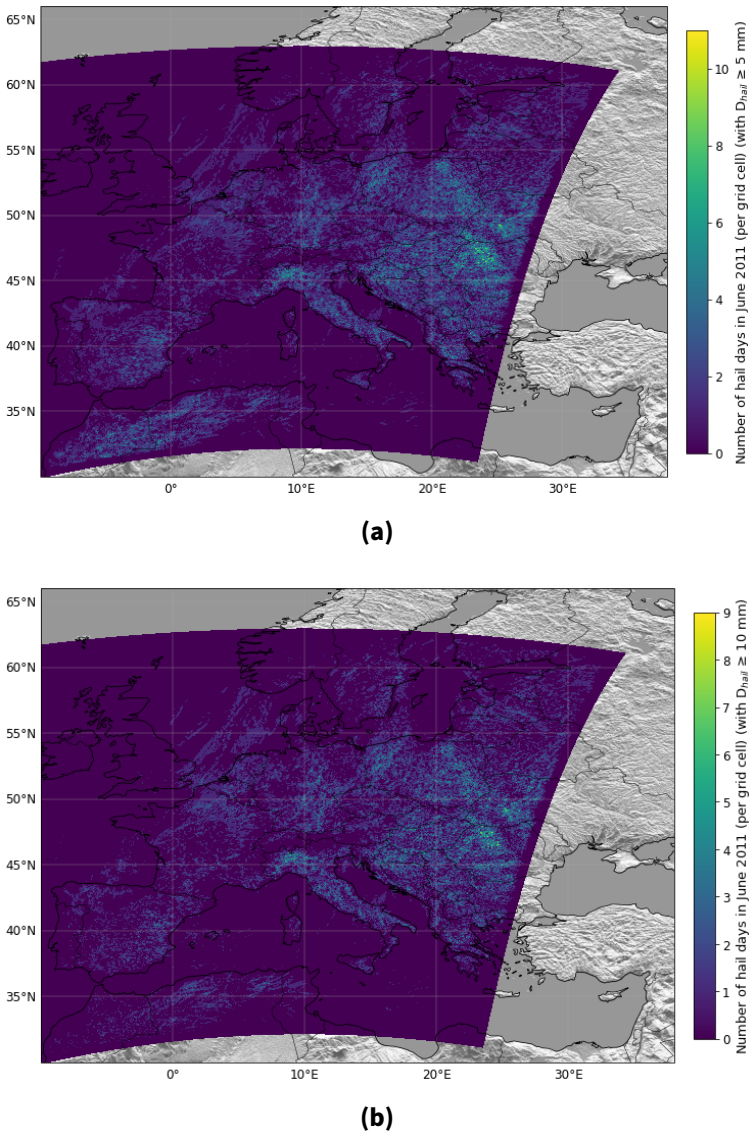

Figure A.1.: Example of HAILCAST hail days with maximum hail diameter greater than or equal to 5 mm in panel (a) and greater than or equal to 10 mm in panel (b).

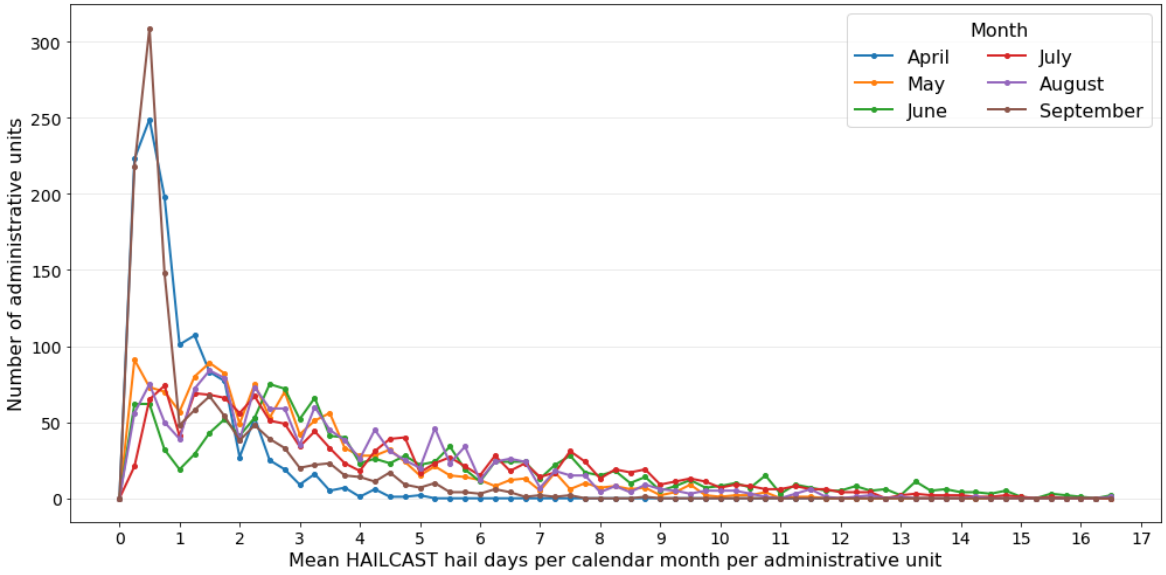

Figure A.2.: Distribution of monthly mean HAILCAST hail-day frequency per NUTS-3 administrative region for April–September during 2011–2021.

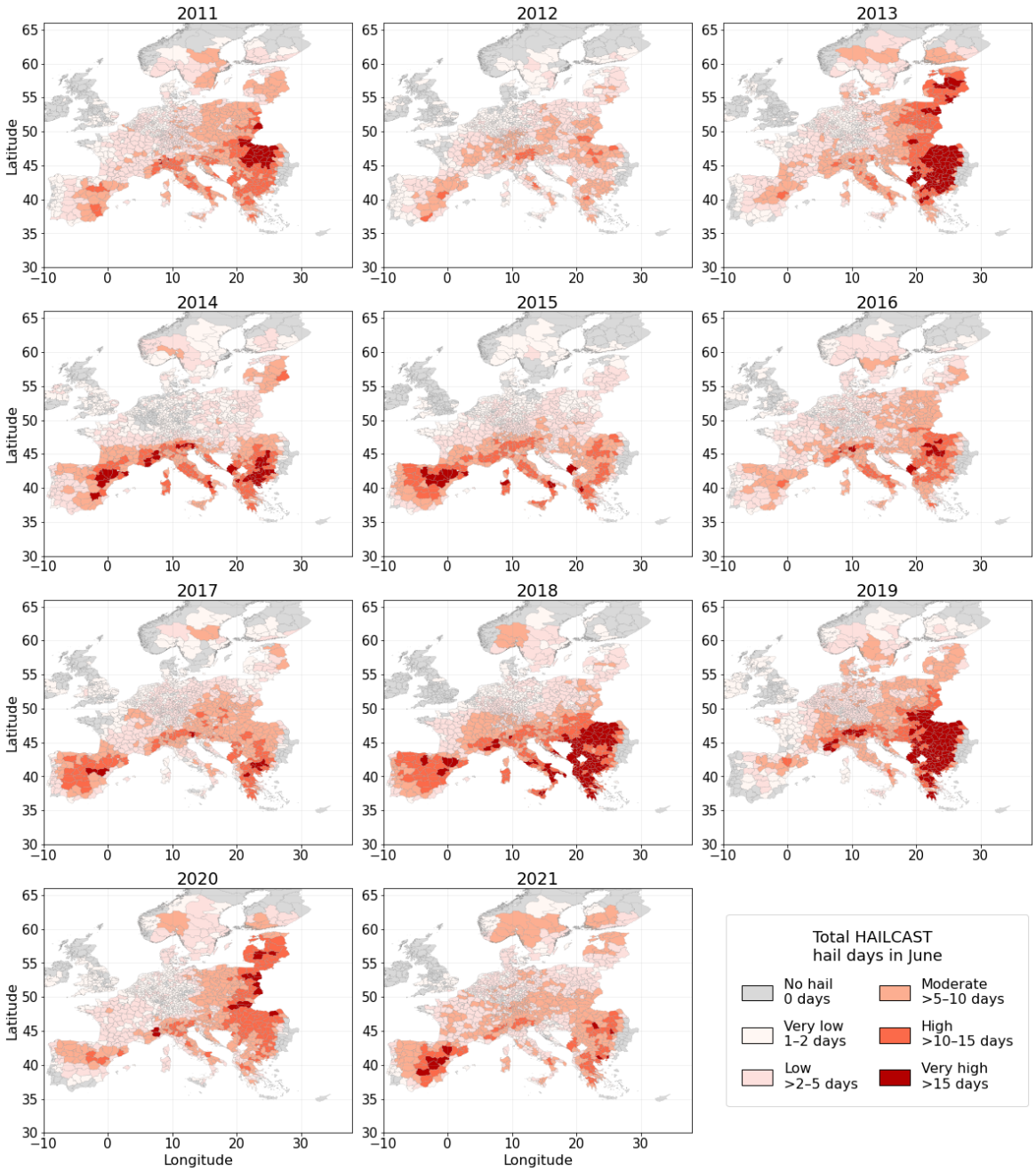

Figure A.3.: Year-by-year HAILCAST hail-day totals per NUTS-3 administrative region for June, shown as an example for 2011–2021.

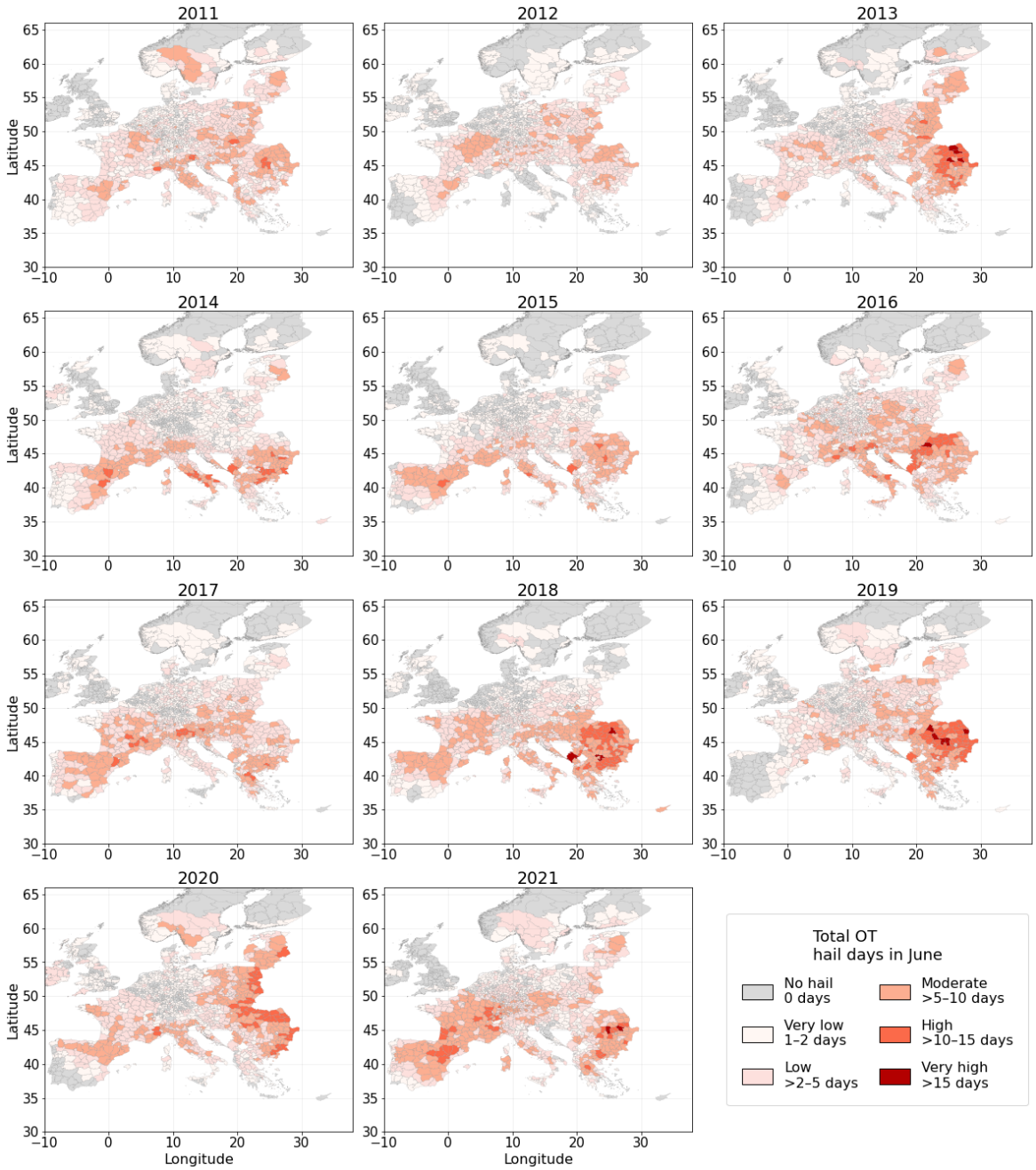

Figure A.4.: Year-by-year OT hail-day totals per NUTS-3 administrative region for June, shown as an example for 2011–2021.

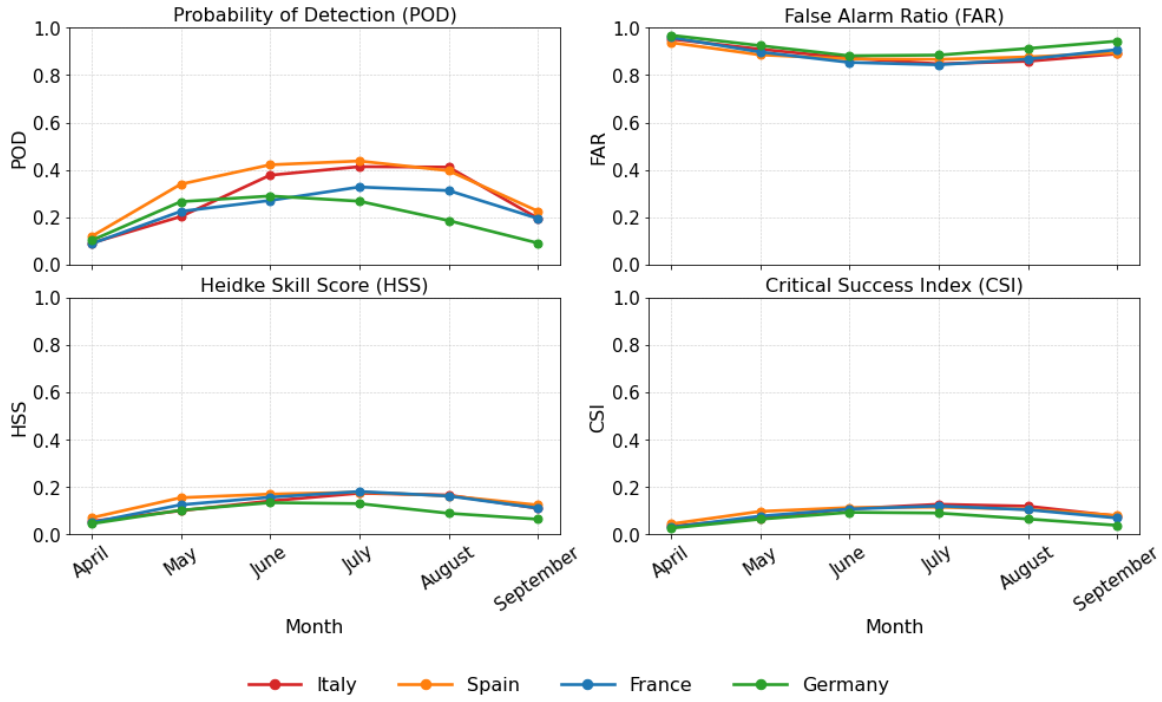

Figure A.5.: Monthly climatological verification metrics for Germany, France, Italy, and Spain (2011–2021). Metrics are based on contingency table classifications of daily hail occurrence at the 20 km × 20 km grid-cell level, aggregated by calendar month across all years.

Acknowledgments

First of all, I would like to thank my supervisors, Michael Kunz and James Daniell, for their guidance and support throughout this project. I would also like to give special thanks to the Risklayer team, especially Annika Maier, who helped me and kept my spirits up, Andreas M. Schäfer for his ideas and for introducing me to James, and Kopper for the moral support along the way. I am also grateful to Jannick Fischer von zur Gathen for helping me understand the OT dataset and for providing a very well-prepared version of the data.

Special thanks to my family and friends for continuous moral support!